

9

Subsectional Basis Functions for Multidimensional and Vector Problems

The numerical techniques discussed in the preceding chapters are deliberately limited to the use of the simplest, lowest order basis and testing functions that are believed to provide converging results. The accuracy of a particular solution usually improves with the polynomial degree of the expansion functions, and it is therefore worthwhile to consider functions smoother than a piecewise-constant or piecewise-linear polynomial. Several types of higher order basis functions were introduced for one-dimensional expansions in Chapter 5. This chapter develops higher order subsectional functions for multidimensional applications, illustrates their implementation in several two-dimensional formulations, and considers some of the computational trade-offs associated with their use.

Despite the fact that electromagnetic fields are vector quantities, previous chapters have only employed a scalar representation. While it is possible to use a scalar basis in the general three-dimensional case, by employing the obvious remedy of separately expanding the x , y , and z components, it is not always desirable. At medium interfaces, for instance, tangential-field components are subject to different continuity conditions than normal components, and a boundary condition can be difficult to impose on an expansion that does not naturally separate into normal and tangential components along the boundary. In addition, scalar representations tend to be continuous, and with certain vector quantities the imposition of complete continuity can produce erroneous results (Section 9.7). Consequently, several types of subsectional *vector* basis functions are introduced for two- and three-dimensional electromagnetic applications. For illustration, one class of functions is used to discretize the curl–curl form of the two-dimensional vector Helmholtz equation for cavity, waveguide, and scattering applications. These functions are extended to the three-dimensional case in this chapter and used for three-dimensional applications in Chapter 11. Other vector expansion functions introduced in this chapter appear appropriate for surface patch discretizations of three-dimensional integral equations and will be employed in Chapter 10.

As the polynomial order of expansion functions is increased, providing greater accuracy with fewer cells, the modeling error associated with simple cell shapes may exceed the discretization error associated with the expansion functions. A remedy is obtained by the use of parametric basis functions defined on cells having curved edges or surfaces. Parametric mappings are discussed for scalar and vector functions.

9.1 HIGHER ORDER LAGRANGIAN BASIS FUNCTIONS ON TRIANGLES [1, 2]

We initially restrict our attention to expansion functions defined on triangular cells. As illustrated in Chapter 3, triangle-based analysis is facilitated through the use of *simplex coordinates* $\{L_1, L_2, L_3\}$ related to the Cartesian coordinates by

$$x = L_1 x_1 + L_2 x_2 + L_3 x_3 \quad (9.1)$$

$$y = L_1 y_1 + L_2 y_2 + L_3 y_3 \quad (9.2)$$

where (x_i, y_i) are the coordinates of the i th vertex of the triangle. These coordinates specify the position of a point within a triangle by giving the relative perpendicular distance measured from each side to the point, with the distance expressed as a fraction of the triangle altitude (Figure 3.9). Since the resulting interior triangles divide the original cell into three parts, each having a fraction of the total area in proportional to their respective coordinate, the additional condition

$$L_1 + L_2 + L_3 = 1 \quad (9.3)$$

must always hold. Equations (9.1)–(9.3) can be inverted to produce

$$L_i = \frac{1}{2A} (a_i + b_i x + c_i y) \quad (9.4)$$

where

$$a_i = x_{i+1} y_{i+2} - x_{i+2} y_{i+1} \quad (9.5)$$

$$b_i = y_{i+1} - y_{i-1} \quad (9.6)$$

$$c_i = x_{i-1} - x_{i+1} \quad (9.7)$$

and A denotes the area of the triangle. The index i in Equations (9.4)–(9.7) assumes values 1, 2, and 3 cyclically, so that if $i = 3$, then $i + 1 = 1$.

Chapters 2 and 3 included examples in which a two-dimensional scalar function was represented by the superposition of linear pyramid basis functions defined on triangular cells (Figure 3.4). The pyramid functions straddle several cells and provide a linear interpolation between values at the cell corners. The representation is automatically continuous across cell boundaries and is therefore especially convenient for representing continuous quantities such as the z -components of the two-dimensional electromagnetic fields.

Since it straddles several cells, the pyramid function depicted in Figure 3.4 is conceptually a global entity. If we restrict our attention to a single cell, it is more convenient to employ a local description in simplex coordinates. Within a particular triangle, a pyramid function centered at node i of the triangle is a linear function having unity value at corner i and vanishing at the other corners. It has the obvious representation

$$B_i(L_1, L_2, L_3) = L_i \quad (9.8)$$

A local picture of the three overlapping functions is provided in Figure 9.1.

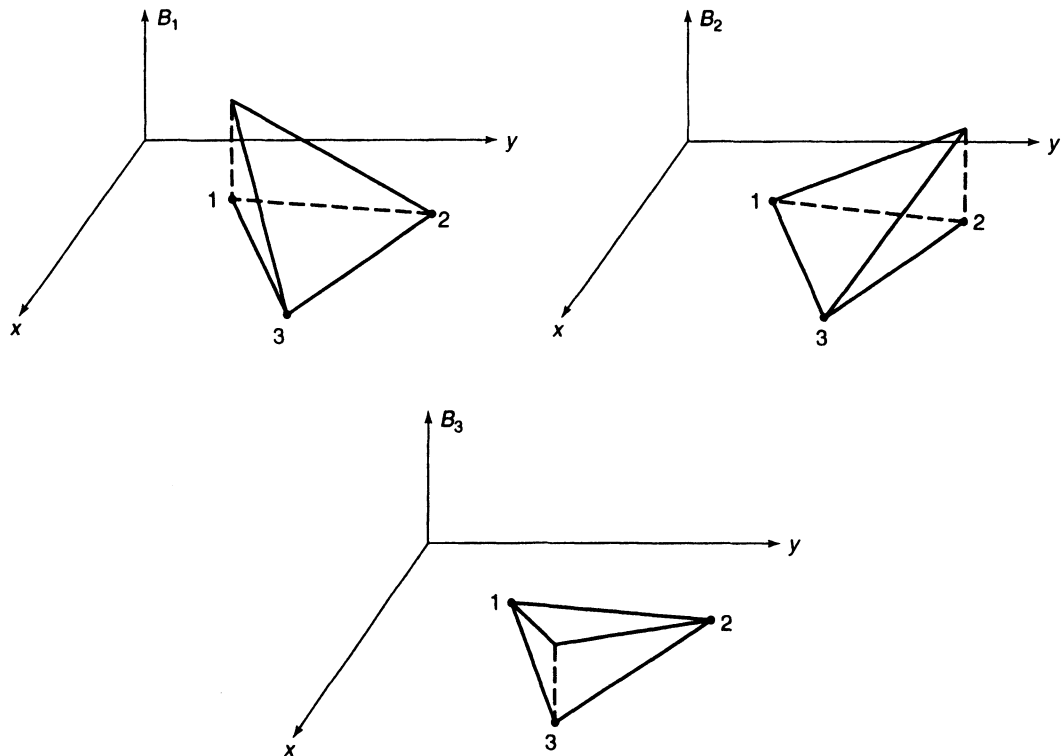


Figure 9.1 Linear Lagrangian functions within a triangular cell.

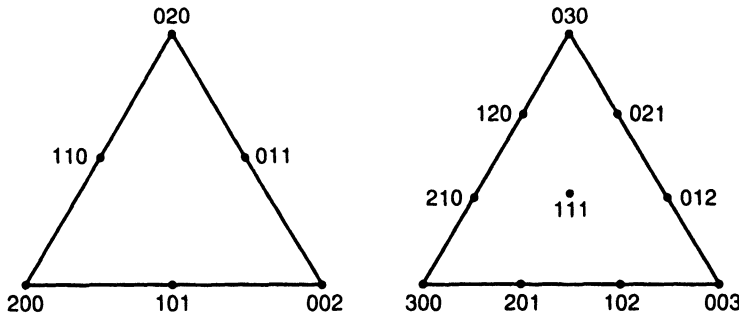
The linear pyramid functions are actually the simplest members of the family of Lagrangian functions defined on triangular cells. From the introductory discussion in Section 5.3, we recall that Lagrangian functions interpolate field values between some number of nodes throughout an interval of interest. As in the one-dimensional case, higher order basis functions on triangles are defined to be interpolatory at a number of points or nodes within each triangular cell. The linear pyramid functions interpolate between the three corner nodes. Quadratic, cubic, and other higher order expansion functions require the introduction of additional nodes within each cell. In general, an M th-order polynomial can be defined over a triangular cell containing m nodes, where m and M are related through

$$m = \frac{1}{2}(M+1)(M+2) \quad (9.9)$$

For example, a quadratic basis ($M = 2$) involves 6 nodes. A cubic basis requires 10 nodes. These nodes can be located at a regularly spaced set of points defined by the simplex coordinate values

$$\left\{ \frac{i}{M}, \frac{j}{M}, \frac{k}{M} \right\} \quad i, j, k = 0, 1, \dots, M \quad (9.10)$$

where the indices are restricted to integers satisfying $i + j + k = M$. For ease of notation when using higher order interpolation functions on triangles, the triple index (i, j, k) is often employed to denote a particular node. Figure 9.2 illustrates the arrangement of nodes and the triple-index scheme for $M = 2$ and $M = 3$.

Figure 9.2 Triple indices for $M = 2$ and $M = 3$.

In order to define an M th-order polynomial basis function B_{ijk} directly in terms of the coordinates $\{L_1, L_2, L_3\}$, Silvester and Ferrari introduce the auxiliary polynomials [2]

$$R_s(M, L) = \frac{1}{s!} \prod_{k=0}^{s-1} (ML - k) \quad (s > 0) \quad (9.11)$$

$$R_0(M, L) = 1 \quad (9.12)$$

The polynomial R_s has exactly s equally spaced zeros at $L = 0, 1/M, \dots, (s-1)/M$ and equals one at $L = s/M$. For illustration, Figure 9.3 depicts these polynomials for $M = 2$ and $M = 3$. The basis functions can be defined in terms of R_s as

$$B_{ijk}(L_1, L_2, L_3) = R_i(M, L_1)R_j(M, L_2)R_k(M, L_3) \quad (9.13)$$

Basis function B_{ijk} has unity value at node ijk and vanishes at every other node in the triangle. Since the basis functions are interpolatory, a function $E(x, y)$ of polynomial order M can be exactly represented throughout the triangle by the superposition

$$E(L_1, L_2, L_3) = \sum_{i=0}^M \sum_{j=0}^{M-i} e_{ijk} B_{ijk}(L_1, L_2, L_3) \quad (9.14)$$

where the coefficient e_{ijk} is the value of E at node (i, j, k) .

As an example, consider the set of quadratic basis functions ($M = 2$). The six functions provided by Equation (9.13) are

$$B_{200}(L_1, L_2, L_3) = (2L_1 - 1)L_1 \quad (9.15)$$

$$B_{020}(L_1, L_2, L_3) = (2L_2 - 1)L_2 \quad (9.16)$$

$$B_{002}(L_1, L_2, L_3) = (2L_3 - 1)L_3 \quad (9.17)$$

$$B_{110}(L_1, L_2, L_3) = 4L_1 L_2 \quad (9.18)$$

$$B_{101}(L_1, L_2, L_3) = 4L_1 L_3 \quad (9.19)$$

$$B_{011}(L_1, L_2, L_3) = 4L_2 L_3 \quad (9.20)$$

These functions are illustrated in Figure 9.4. Observe that the first three functions have unity value at nodes 200, 020, and 002, respectively, while the latter three functions have unity value in the center of one of the three sides. Each of the basis functions vanishes at five of the six nodes. The superposition of all six functions, appropriately weighted, provides a quadratic representation with coefficients associated with the field values at each

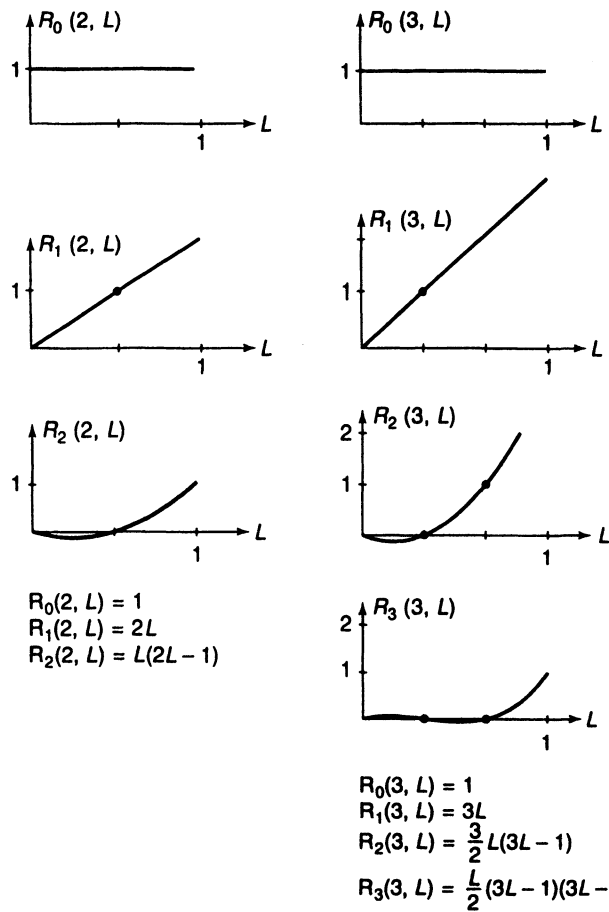


Figure 9.3 Polynomials used to build Lagrangian functions.

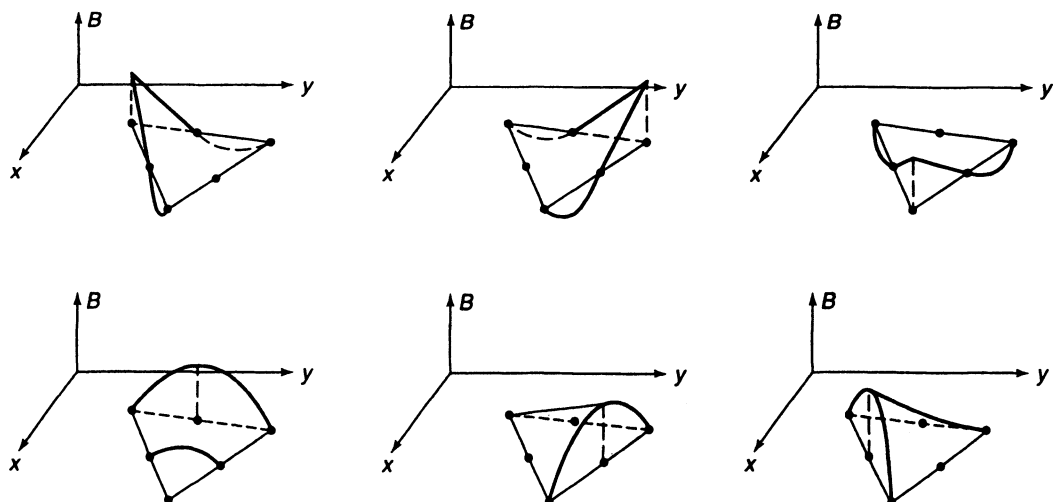


Figure 9.4 Quadratic Lagrangian functions within a triangular cell.

of the six nodes. A description of these functions in Cartesian coordinates is not particularly illuminating but can be obtained using Equation (9.4) if desired.

The higher order Lagrangian polynomials permit a smoother representation of the field within a cell than possible using the linear pyramid functions employed in previous chapters. As discussed in Chapter 5, the interpolation error associated with these functions behaves as $O(\Delta^{p+1})$ as $\Delta \rightarrow 0$, where Δ is the longest edge in the triangle and p is the polynomial degree [3]. Although the actual solution error in a particular situation may be dominated by other sources (such as the use of approximate radiation boundary conditions), observations support the notion that the overall error is primarily interpolation error [4]. In any case, for fixed computational resources, a far greater reduction in interpolation error for small Δ can be obtained by increasing the polynomial order p than by decreasing the cell size.

Although the higher order Lagrangian polynomials permit a smoother representation of the field within a cell, the smoother representation is not imposed across cell boundaries. Continuity of the global expansion is ensured by the common nodes along each boundary, but the normal derivative of the field expansion at a cell boundary is generally not continuous. The discontinuity of the derivatives is usually a second order effect producing an error that disappears in the limit as the cell sizes shrink to zero. In fact, whether or not the derivative discontinuity is undesirable depends on the specific problem under consideration. As an example, the z -components of the true electric and magnetic fields in a two-dimensional problem exhibit discontinuous normal derivatives at material interfaces, and consequently it might be desirable that the expansion functions permit this behavior.

If derivative continuity is desired, the Hermitian representation introduced in Section 5.3 can be extended to the multidimensional case [3]. In the two-dimensional situation, it is necessary to adopt an expansion of polynomial order 5 in order to ensure the continuity of a scalar function and its tangential and normal derivatives across the cell boundaries. If used with triangular cell shapes, at least two different representations are possible, one employing 18 functions [5] and the other employing 21 functions. The 18-function expansion is only complete to polynomial order 4 and will produce an interpolation error of $O(\Delta^5)$ as $\Delta \rightarrow 0$, while the 21-function expansion is complete to order 5 and produces an interpolation error of $O(\Delta^6)$ [3]. Since all the Hermitian coefficients are shared by multiple cells, the Hermitian type of expansion offers the possibility of a high-order expansion with far fewer unknowns than a Lagrangian representation of the same order. However, the reduction in unknowns is offset by an increase in the number of nonzero entries per row of the matrix.

To illustrate the implementation of higher order Lagrangian functions, we turn our attention to an example employing the scalar Helmholtz equation for two-dimensional scattering.

9.2 EXAMPLE: USE OF HIGHER ORDER BASIS FUNCTIONS WITH THE TWO-DIMENSIONAL SCALAR HELMHOLTZ EQUATION

Consider the two-dimensional scattering problem posed at the beginning of Chapter 3, involving a TM wave incident on a cylinder containing dielectric and magnetic inhomogeneities. A weak equation incorporating the Bayliss–Turkel RBC was provided in Equation

(3.87), which we repeat for convenience:

$$\begin{aligned} & \iint_{\Gamma} \left(\frac{1}{\mu_r} \nabla T \cdot \nabla E_z^{\text{tot}} - k^2 \epsilon_r T E_z^{\text{tot}} \right) dx dy - \int_{\partial\Gamma} \left(\alpha T E_z^{\text{tot}} - \beta \frac{\partial T}{\partial \phi} \frac{\partial E_z^{\text{tot}}}{\partial \phi} \right) \rho d\phi \\ &= \int_{\partial\Gamma} T \left(\frac{\partial E_z^{\text{inc}}}{\partial \rho} - \alpha E_z^{\text{inc}} - \beta \frac{\partial^2 E_z^{\text{inc}}}{\partial \phi^2} \right) \rho d\phi \end{aligned} \quad (9.21)$$

The variables α and β are defined in Equations (3.81) and (3.82). The finite-element discretization of this equation produces a matrix equation

$$\mathbf{A}\mathbf{e} = \mathbf{b} \quad (9.22)$$

with matrix entries given by

$$\begin{aligned} A_{mn} = & \iint_{\Gamma} \left(\frac{1}{\mu_r} \nabla B_m \cdot \nabla B_n - k^2 \epsilon_r B_m B_n \right) dx dy \\ & - \int_{\partial\Gamma} \left(\alpha B_m B_n - \beta \frac{\partial B_m}{\partial \phi} \frac{\partial B_n}{\partial \phi} \right) \rho d\phi \end{aligned} \quad (9.23)$$

and

$$b_m = \int_{\partial\Gamma} B_m \left(\frac{\partial E_z^{\text{inc}}}{\partial \rho} - \alpha E_z^{\text{inc}} - \beta \frac{\partial^2 E_z^{\text{inc}}}{\partial \phi^2} \right) \rho d\phi \quad (9.24)$$

where $\{B_n\}$ denote the basis functions. Chapter 3 presented a detailed description of the computational implementation of this procedure for linear basis functions.

We wish to evaluate these expressions using the higher order Lagrangian functions developed in the preceding section. Following the procedure employed in Chapter 3, we initially construct *element matrices* on a cell-by-cell basis containing the interaction terms. The element matrices will be of order m , where m is a specific function of the polynomial order M as described by Equation (9.9). Linear, quadratic, and cubic expansion functions give rise to element matrices of order 3, 6, and 10, respectively. For any polynomial order, the two-dimensional integrals to be evaluated are

$$A_{pq}^{(1)} = \iint_{\Gamma} \nabla B_p \cdot \nabla B_q dx dy \quad (9.25)$$

$$A_{pq}^{(2)} = \iint_{\Gamma} B_p B_q dx dy \quad (9.26)$$

The required boundary integrals are

$$A_{pq}^{(3)} = \int_{\partial\Gamma} B_p B_q dt \quad (9.27)$$

and

$$\int_{\partial\Gamma} \frac{\partial B_p}{\partial \phi} \frac{\partial B_q}{\partial \phi} \rho d\phi \quad (9.28)$$

Using the change of variable

$$\frac{\partial}{\partial \phi} = \rho \frac{\partial}{\partial t} \quad (9.29)$$

Equation (9.28) can be written in terms of the integral

$$A_{pq}^{(4)} = \int_{\partial\Gamma} \frac{\partial B_p}{\partial t} \frac{\partial B_q}{\partial t} dt \quad (9.30)$$

For a triangular-cell model, these integrals can be evaluated in closed form for any polynomial order. Since the evaluation becomes tedious for higher order functions [neglecting symmetry across the main diagonal, the $M = 4$ element matrices for (9.25) and (9.26) each require 225 entries!], it is often accomplished by numerical quadrature. Purists who prefer closed-form evaluation will probably find the approach of P. P. Silvester [2, 6] to be the most convenient. We summarize this procedure below.

Consider the evaluation of Equation (9.25) over one triangular cell denoted Γ_t . The integrand can be written explicitly as

$$\frac{\partial B_p}{\partial x} \frac{\partial B_q}{\partial x} + \frac{\partial B_p}{\partial y} \frac{\partial B_q}{\partial y} \quad (9.31)$$

Using the chain rule of differentiation and Equation (9.4), we find

$$\frac{\partial B_q}{\partial x} = \sum_{i=1}^3 \frac{\partial B_q}{\partial L_i} \frac{\partial L_i}{\partial x} = \sum_{i=1}^3 \frac{\partial B_q}{\partial L_i} \frac{b_i}{2A} \quad (9.32a)$$

$$\frac{\partial B_q}{\partial y} = \sum_{i=1}^3 \frac{\partial B_q}{\partial L_i} \frac{\partial L_i}{\partial y} = \sum_{i=1}^3 \frac{\partial B_q}{\partial L_i} \frac{c_i}{2A} \quad (9.32b)$$

The integral can now be written as

$$A_{pq}^{(1)} = \frac{1}{4A^2} \iint_{\Gamma_t} \sum_{i=1}^3 \sum_{j=1}^3 (b_i b_j + c_i c_j) \frac{\partial B_p}{\partial L_i} \frac{\partial B_q}{\partial L_j} dx dy \quad (9.33)$$

Geometric properties of a triangle dictate that [2]

$$b_i b_j + c_i c_j = -2A \cot \theta_k \quad (i \neq j) \quad (9.34)$$

$$b_i^2 + c_i^2 = 2A(\cot \theta_j + \cot \theta_k) \quad (9.35)$$

where θ_i is the interior angle at node i and the indices i , j , and k assume the values 1, 2, and 3 cyclically. It follows that the integral of Equation (9.25) reduces to

$$A_{pq}^{(1)} = \frac{1}{2A} \iint_{\Gamma_t} \sum_{i=1}^3 \left(\frac{\partial B_p}{\partial L_{i+1}} - \frac{\partial B_p}{\partial L_{i-1}} \right) \left(\frac{\partial B_q}{\partial L_{i+1}} - \frac{\partial B_q}{\partial L_{i-1}} \right) \cot \theta_i dx dy \quad (9.36)$$

It remains to transform the integral from Cartesian coordinates to the local-area coordinates $\{L_1, L_2, L_3 = 1 - L_1 - L_2\}$ using the transformation

$$dx dy = dL_1 dL_2 \frac{\partial(x, y)}{\partial(L_1, L_2)} = 2A dL_1 dL_2 \quad (9.37)$$

Equation (9.25) can be written in the local coordinates as

$$A_{pq}^{(1)} = \sum_{i=1}^3 Q_{pq}^{(i)} \cot \theta_i \quad (9.38)$$

where

$$Q_{pq}^{(i)} = \iint_{\Gamma_t} \left(\frac{\partial B_p}{\partial L_{i+1}} - \frac{\partial B_p}{\partial L_{i-1}} \right) \left(\frac{\partial B_q}{\partial L_{i+1}} - \frac{\partial B_q}{\partial L_{i-1}} \right) dL_1 dL_2 \quad (9.39)$$

Note that $Q_{pq}^{(i)}$ is independent of the specific shape of the triangle Γ_i . In fact, Equation (9.39) consists entirely of integrals having the form [2]

$$I = \iint_{\Gamma_i} L_1^a L_2^b L_3^c dL_1 dL_2 = \frac{a!b!c!}{(a+b+c+2)!} \quad (9.40)$$

where a , b , and c represent integer powers.

A similar transformation can be applied to Equation (9.26) to produce

$$A_{pq}^{(2)} = 2A \iint_{\Gamma_i} B_p B_q dL_1 dL_2 \quad (9.41)$$

which can also be evaluated using Equation (9.40).

In the simplex coordinate system, the integrals arising in the matrix elements depend only on the order of the interpolation functions and not on the specific shape or size of the triangular cells. The evaluation of these integrals may be done once and for all prior to the matrix fill and tabulated in a systematic way for easy access. The remaining calculations required for matrix element computation are limited to the area A of each cell and the three cotangents necessary for Equation (9.38). The three Q -matrices required for Equation (9.38) are simple permutations of each other, and Sylvester's approach employs rotation matrices to construct the entries of each Q -matrix from a minimal-sized table [2, 6]. FORTRAN subroutines producing the complete element matrices for (9.25) and (9.26) are available for polynomial orders $M = 1$ through $M = 4$ [2].

The entries of the boundary integral terms in Equations (9.27) and (9.30) can be found in a similar manner. Their evaluation will be left as an exercise for the reader.

The complete finite-element system may be constructed by scanning through the mesh, obtaining element matrices on a cell-by-cell basis, and subsequently adding these entries to the global system in Equation (9.22). To facilitate the required bookkeeping, we employ a *connectivity matrix* mapping the local node numbers to the global node numbers. The primary connectivity array has dimension N_c by m , where N_c is the number of cells in the model and m is the number of nodes per cell. A second connectivity array is required to link nodes on the outer boundary with the adjacent cells, in order to facilitate the evaluation of the boundary integral terms. These connectivity arrays are part of the scatterer model generated prior to finite-element analysis. (As we have seen in previous chapters, the scatterer model also includes a list of node coordinates and the constitutive parameters of each cell.)

The use of higher order expansion functions increases the required storage relative to linear expansion functions as a consequence of larger element matrices and a larger connectivity matrix. In addition, the sparsity of the resulting global system will decrease as the order of the expansion functions increases, since more basis functions interact over each cell. For a scatterer model having a fixed number of cells, the number of nodes and the number of nonzero entries can grow quickly with increasing polynomial order. For the idealized situation of N equilateral triangles arranged in an asymptotically large hexagonal mesh, the number of nodes grows as $N/2$, $4N/2$, and $9N/2$ for linear, quadratic, and cubic Lagrangian functions. Data shown in Figure 9.5 from a variety of triangular-cell models closely tracks this 1:4:9 ratio. From a similar analysis, the number of nonzero entries in the A -matrix can be estimated as $3.5N$, $23N$, and $76.5N$ for linear, quadratic, and cubic Lagrangian functions on an idealized mesh containing N cells. Figure 9.6 illustrates actual data for linear and quadratic expansions that are in reasonable agreement with these estimates. The overall computational requirements, however, may not always grow as

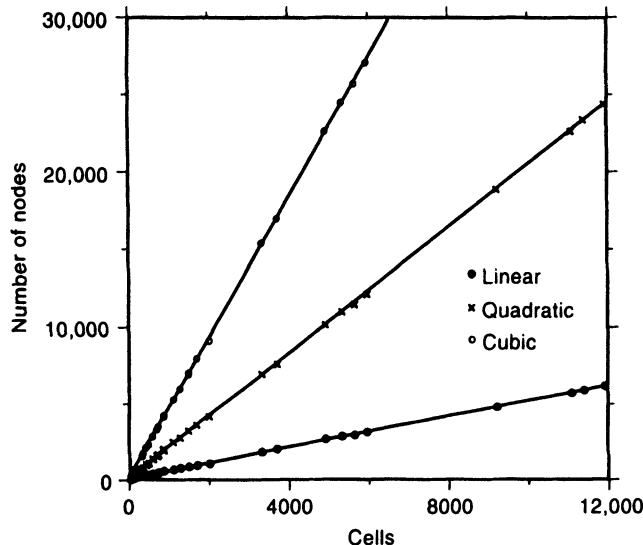


Figure 9.5 Growth of nodes with element order versus number of cells in a triangular-cell mesh.

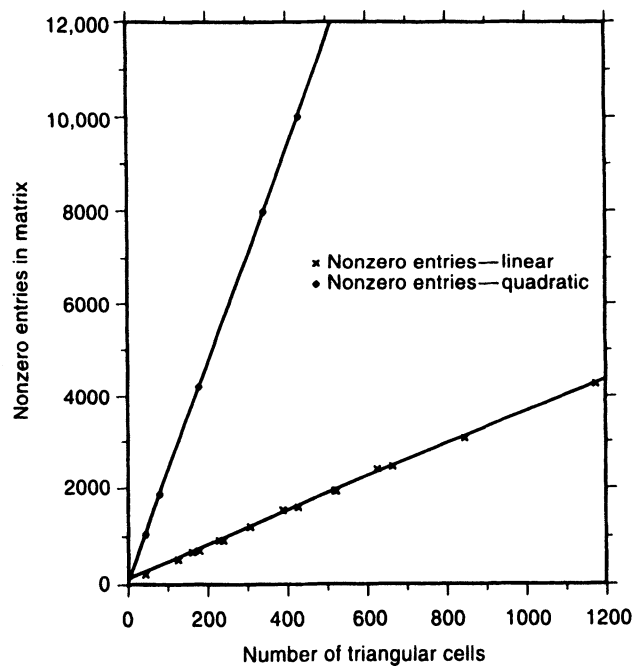


Figure 9.6 Growth of matrix entries with element order versus number of cells in a triangular-cell mesh.

quickly as these figures seem to suggest. Figure 9.7 compares the number of nonzero entries in the A -matrix after LU factorization via the sparse matrix program Y12M [7] for linear and quadratic expansions. These data suggest that there is often little additional storage in the use of quadratic expansion functions compared to linear for an equal number

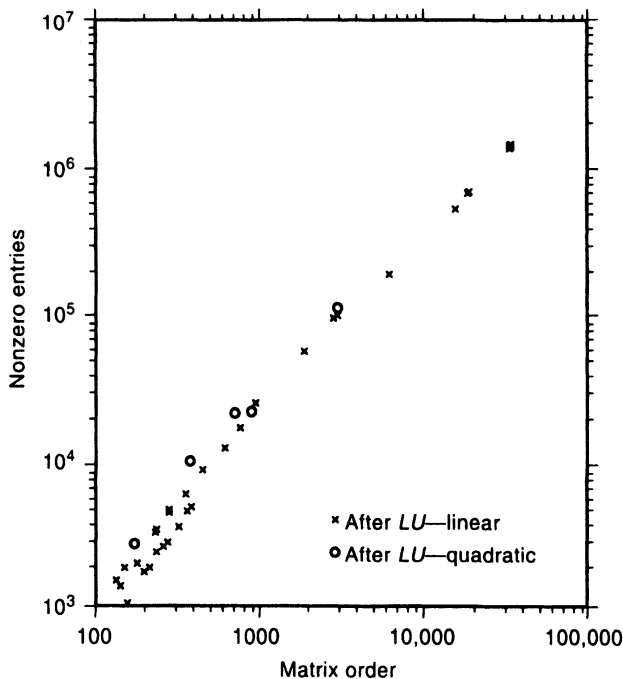


Figure 9.7 Nonzero entries after LU factorization versus matrix order: Y12M performance for scalar bases.

of nodes. Furthermore, we expect a substantial improvement in accuracy when using higher order expansion functions.

As an illustration, consider a lossy dielectric cylinder of size $ka = 2$ and relative permittivity $\epsilon_r = 2.56 - j2.56$. Table 9.1 shows the interior E_z -field produced by an incident TM plane wave along a cut through the center of the cylinder. Results obtained using linear basis and testing functions are compared with results from a quadratic Lagrangian representation for a mesh containing 1480 triangular cells. The linear expansion involves one unknown for each of the 781 corner nodes in the mesh, yielding a density within the cylinder of $105 \text{ nodes}/\lambda_d^2$. For the quadratic expansion functions, the additional midside nodes bring the total to 3041 unknowns. The second-order Bayliss–Turkel RBC is imposed on a circular boundary having radius $\rho = 0.98\lambda_0$, approximately three times the cylinder radius. The accuracy obtained with the quadratic basis and testing functions is quite good, especially in light of the fact that the RBC is approximate.

As a second example, Figure 9.8 shows the electric field magnitude within a cylinder having $ka = 3.5449$ and $\epsilon_r = 6$. Linear and quadratic expansions were employed using different models adjusted to produce a similar number of unknowns (2905 for the linear functions, 3041 for the quadratic). The second-order Bayliss–Turkel RBC was imposed at $\rho = 1.36\lambda_0$, a location approximately 2.4 times the radius of the cylinder. The linear result employed a mesh with 5656 triangular cells, 2905 nodes, and a maximum cell dimension of $0.068\lambda_0$. The quadratic result employed a mesh with 1480 triangular cells, 3041 nodes (781 corner nodes), and a maximum cell dimension of $0.135\lambda_0$. Although the linear result contains gross errors, the quadratic result appears to exhibit excellent agreement with the exact solution. (The quadratic basis coefficients used to plot Figure 9.8 actually have a total error that varies between 0.4 and 12% along this cut through the cylinder.)

TABLE 9.1 E_z -Field Produced by Incident TM Plane Wave Along $y = 0$ Cut Through Center of Circular, Homogeneous Dielectric Cylinder Having $ka = 2$ and Relative Permittivity $\epsilon_r = 2.56 - j2.56$

x	Magnitude of E_z			Phase of E_z (deg)		
	Linear	Quadratic	Exact	Linear	Quadratic	Exact
-0.319	0.7163	0.7046	0.7039	123.75	123.28	123.32
-0.255	0.5683	0.5568	0.5566	83.39	82.32	82.35
-0.191	0.4508	0.4388	0.4386	43.13	41.62	41.64
-0.128	0.3568	0.3445	0.3443	1.80	0.05	0.07
-0.064	0.2902	0.2768	0.2767	-40.65	-42.66	-42.63
0.0	0.2414	0.2276	0.2274	-82.36	-84.81	-84.78
0.064	0.1962	0.1833	0.1831	-126.16	-129.01	-128.98
0.128	0.1837	0.1698	0.1696	178.41	178.09	178.12
0.191	0.2412	0.2237	0.2235	139.68	135.48	135.50
0.255	0.3169	0.2964	0.2961	120.23	116.14	116.15
0.319	0.3511	0.3303	0.3299	115.98	112.54	112.57

Note: Results obtained using linear and quadratic expansion functions with the same 1480-cell model are compared with the exact solution. The numerical solutions were obtained with the second-order Bayliss-Turkel RBC imposed at $\rho = 0.98 \lambda_0$.

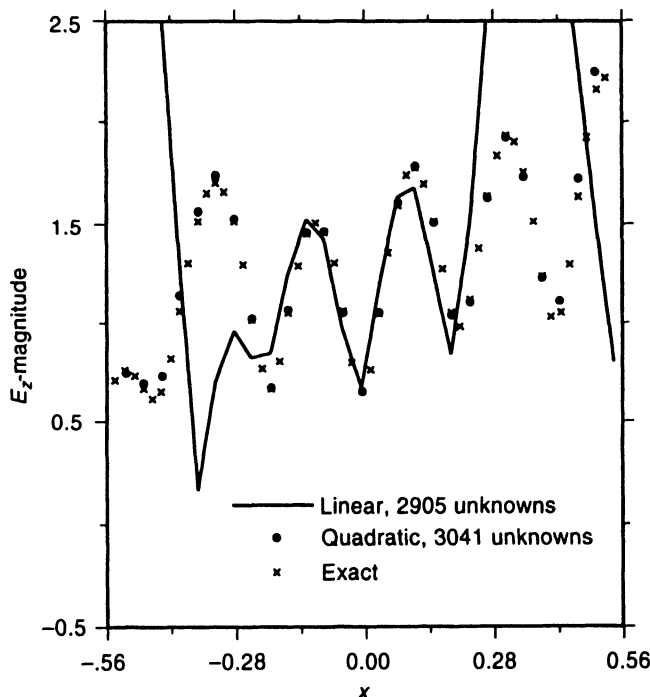


Figure 9.8 Electric field within a circular dielectric cylinder obtained using linear (solid line) and quadratic (dots) expansion functions. The exact solution is also shown (crosses). Both results required about the same number of unknowns. The cylinder has $ka = 3.5449$, $\epsilon_r = 6$, $\mu_r = 1$, and the radiation boundary is located at $\rho = 1.36\lambda_0$.

Numerical results for the electric field in the center of a circular dielectric cylinder with $\epsilon_r = 3$ and $ka = 1$ were presented in Table 3.2 based on linear Lagrangian basis functions. For purposes of comparison, Table 9.2 shows the error in the electric field for quadratic basis functions defined on triangular-cell models similar to those used to create Table 3.2. In this formulation, the approximate Bayliss–Turkel RBC is used to truncate the mesh at a radius of 0.3λ (less than twice the cylinder radius). Although the approximate RBC places a limit on the accuracy possible with a large density of cells, the error due to the RBC appears to be less than 0.5% in this case.

TABLE 9.2 Numerical Values of E_z -Field Produced at Center of Circular Dielectric Cylinder with $\epsilon_r = 3$ and $ka = 1$

Model	Longest Edge in Mesh	Magnitude of E_z	Phase of E_z (deg)	Error (%)
97-Node	$0.166\lambda_0$	0.909	-57.36	1.88
273-Node	$0.098\lambda_0$	0.897	-57.39	0.59
565-Node	$0.071\lambda_0$	0.895	-57.37	0.37
901-Node	$0.053\lambda_0$	0.895	-57.36	0.30
Exact	—	0.892	-57.36	—

Note: Results from four triangular-cell models are compared with the exact solution. The Bayliss–Turkel RBC is imposed at a 0.3λ radius and places a limit on the accuracy in this case. Results are obtained with quadratic basis functions.

9.3 LAGRANGIAN BASIS FUNCTIONS FOR RECTANGULAR AND QUADRILATERAL CELLS

While triangular cells offer modeling flexibility, a rectangular-cell mesh is sometimes preferred because of ease of generation and visualization. Often, an irregular region can be represented by a combination of rectangular and triangular cells, provided that the continuity of the expansion is maintained across cell boundaries. This section considers the development of Lagrangian basis functions for rectangular domains. In addition, basis functions defined on quadrilateral cells can be obtained by a straightforward transformation of the rectangular-cell functions. This transformation is described.

The simplest representation on rectangles is bilinear interpolation between the four cell corners. A suitable expansion consists of four overlapping functions, each having the general form

$$B_i(x, y) = \alpha_i + \beta_i x + \gamma_i y + \delta_i xy \quad (9.42)$$

The four degrees of freedom in each function allow interpolation to one of the four corners of the cell, that is, $B_i(x, y) = 1$ at node i and $B_i(x, y) = 0$ at the other three nodes. Because the representation along every edge of the rectangular cell is linear, this expansion automatically provides continuity to a linear expansion on an adjacent cell, whether it be rectangular or triangular in shape. These bilinear functions are the lowest order member of a Lagrangian family for rectangular cells.

In order to develop a general formula for these expansion functions, we repeat the expression originally introduced in Equation (5.33) for the j th Lagrangian function of order

$N - 1$ on an interval $[x_1, x_N]$:

$$\phi_j(x) = \frac{(x - x_1)(x - x_2) \cdots (x - x_{j-1})(x - x_{j+1}) \cdots (x - x_N)}{(x_j - x_1)(x_j - x_2) \cdots (x_j - x_{j-1})(x_j - x_{j+1}) \cdots (x_j - x_N)} \quad (9.43)$$

This expression defines N independent polynomials $\{\phi_1, \phi_2, \dots, \phi_N\}$ spanning the interval. It is convenient to introduce a local coordinate system (η, ξ) , where

$$\eta = \frac{2x - x_1 - x_2}{x_2 - x_1} \quad (9.44)$$

$$\xi = \frac{2y - y_1 - y_2}{y_2 - y_1} \quad (9.45)$$

These coordinates are illustrated in Figure 9.9. We can construct a general formula for the Lagrangian expansion functions using

$$B_{ij}(\eta, \xi) = \phi_i(\eta)\phi_j(\xi) \quad (9.46)$$

where $\phi_i(\eta)$ denotes a polynomial of order M spanning the interval $[-1, 1]$, and i and j may assume values $1, 2, \dots, M + 1$.

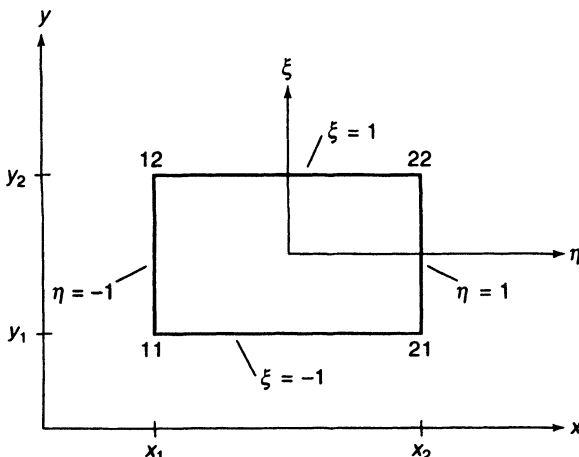


Figure 9.9 Local (η, ξ) coordinate system.

If expressed as explicit functions of η and ξ over the domain $(-1 < \eta < 1, -1 < \xi < 1)$, the bilinear expansion functions have the form

$$B_{11}(\eta, \xi) = \frac{1 - \eta}{2} \frac{1 - \xi}{2} \quad (9.47)$$

$$B_{12}(\eta, \xi) = \frac{1 - \eta}{2} \frac{\xi + 1}{2} \quad (9.48)$$

$$B_{21}(\eta, \xi) = \frac{\eta + 1}{2} \frac{1 - \xi}{2} \quad (9.49)$$

$$B_{22}(\eta, \xi) = \frac{\eta + 1}{2} \frac{\xi + 1}{2} \quad (9.50)$$

Element matrices for integrals such as (9.25) and (9.26) can be evaluated directly in the

(η, ξ) -coordinate system. The mapping from (η, ξ) to (x, y) involves a transformation

$$\begin{bmatrix} \frac{\partial}{\partial \eta} \\ \frac{\partial}{\partial \xi} \end{bmatrix} = \mathbf{J} \begin{bmatrix} \frac{\partial}{\partial x} \\ \frac{\partial}{\partial y} \end{bmatrix} \quad (9.51)$$

where \mathbf{J} is the Jacobian matrix

$$\mathbf{J} = \begin{bmatrix} \frac{\partial x}{\partial \eta} & \frac{\partial y}{\partial \eta} \\ \frac{\partial x}{\partial \xi} & \frac{\partial y}{\partial \xi} \end{bmatrix} = \begin{bmatrix} \frac{x_2 - x_1}{2} & 0 \\ 0 & \frac{y_2 - y_1}{2} \end{bmatrix} \quad (9.52)$$

Therefore, since

$$dx dy = (\det \mathbf{J}) d\eta d\xi = \frac{1}{4} A d\eta d\xi \quad (9.53)$$

where A is the area of the rectangular cell, (9.26) can be written as

$$A_{pq}^{(2)} = \int_x \int_y B_p B_q dx dy = \frac{A}{4} \int_{\eta=-1}^1 \int_{\xi=-1}^1 B_p B_q d\eta d\xi \quad (9.54)$$

In a similar manner, (9.51) can be used to transform (9.25) into the expression

$$\begin{aligned} A_{pq}^{(1)} &= \int_x \int_y \left[\frac{\partial B_p}{\partial x} \frac{\partial B_p}{\partial y} \right] \begin{bmatrix} \frac{\partial B_q}{\partial x} \\ \frac{\partial B_q}{\partial y} \end{bmatrix} dx dy \\ &= \frac{A}{4} \int_{\eta=-1}^1 \int_{\xi=-1}^1 \left[\frac{\partial B_p}{\partial \eta} \frac{\partial B_p}{\partial \xi} \right] \mathbf{J}^{-T} \mathbf{J}^{-1} \begin{bmatrix} \frac{\partial B_q}{\partial \eta} \\ \frac{\partial B_q}{\partial \xi} \end{bmatrix} d\eta d\xi \\ &= \frac{y_2 - y_1}{x_2 - x_1} \int_{\eta=-1}^1 \int_{\xi=-1}^1 \frac{\partial B_p}{\partial \eta} \frac{\partial B_q}{\partial \eta} + \frac{x_2 - x_1}{y_2 - y_1} \int_{\eta=-1}^1 \int_{\xi=-1}^1 \frac{\partial B_p}{\partial \xi} \frac{\partial B_q}{\partial \xi} \end{aligned} \quad (9.55)$$

The generation of the actual element matrix entries for the bilinear basis functions follows directly from (9.54) and (9.55) and will be left as an exercise.

Biquadratic functions may be defined to interpolate between nine nodes on a rectangular cell. The appropriate general form is obtained from Equation (9.46), with quadratic polynomials used for each ϕ . Specific expressions in local coordinates are

$$B_{11}(\eta, \xi) = \frac{\eta(\eta - 1)}{2} \frac{\xi(\xi - 1)}{2} \quad (9.56)$$

$$B_{12}(\eta, \xi) = \frac{\eta(\eta - 1)}{2} (1 + \xi)(1 - \xi) \quad (9.57)$$

$$B_{13}(\eta, \xi) = \frac{\eta(\eta - 1)}{2} \frac{\xi(\xi + 1)}{2} \quad (9.58)$$

$$B_{21}(\eta, \xi) = (1 + \eta)(1 - \eta) \frac{\xi(\xi - 1)}{2} \quad (9.59)$$

$$B_{22}(\eta, \xi) = (1 + \eta)(1 - \eta)(1 + \xi)(1 - \xi) \quad (9.60)$$

$$B_{23}(\eta, \xi) = (1 + \eta)(1 - \eta) \frac{\xi(\xi + 1)}{2} \quad (9.61)$$

$$B_{31}(\eta, \xi) = \frac{\eta(\eta + 1)}{2} \frac{\xi(\xi - 1)}{2} \quad (9.62)$$

$$B_{32}(\eta, \xi) = \frac{\eta(\eta + 1)}{2}(1 + \xi)(1 - \xi) \quad (9.63)$$

$$B_{33}(\eta, \xi) = \frac{\eta(\eta + 1)}{2} \frac{\xi(\xi + 1)}{2} \quad (9.64)$$

Each of these functions has unity value at one of the nine nodes and vanishes at the others. Element matrix entries for these functions can also be obtained from Equations (9.54) and (9.55). Extensions to higher order polynomials follow in an obvious manner. The general form employed in Equation (9.46) allows flexibility in deriving other expansion functions; in fact, a large variety may be constructed that are of mixed polynomial order (one degree along η and a different degree along ξ) [1].

Lagrangian functions on rectangular cells lack one important property associated with Lagrangian functions on triangles. On triangular cells, the expansion functions are complete to an exact polynomial order. The polynomial terms required for completeness to a particular degree are best illustrated through the Pascal triangle (Figure 9.10). Unfortunately, the Lagrangian functions used on rectangular cells are not complete to the highest order appearing in the representation. As an example, the biquadratic functions contain terms that vary as x^2y^2 but do not contain terms of y^4 or even y^3 ! Because the accuracy of the numerical solution is constrained by the first “missing” term in the expansion, the associated interpolation error may only decrease as $O(\Delta^3)$ rather than as $O(\Delta^5)$ as $\Delta \rightarrow 0$. Consequently, the rectangular Lagrangian functions might be construed to contain wasted degrees of freedom.

			Interpolation error as $\Delta \rightarrow 0$ $O(\Delta)$
1		Order 0	
x	y	Order 1	$O(\Delta^2)$
x^2	xy	Order 2	$O(\Delta^3)$
x^3	x^2y	Order 3	$O(\Delta^4)$
x^4	x^3y	Order 4	$O(\Delta^5)$
x^2y^2	xy^3		
x^3y^2	y^4		

Figure 9.10 Pascal’s triangle to illustrate completeness properties of polynomial expansions.

Obviously, a mesh restricted to rectangular cells is only useful for simple geometries. General quadrilateral cells offer much more flexibility while providing a conceptual similarity to rectangular cells. A bilinear transformation can be used to map basis functions from rectangular cells to quadrilateral cells.

Consider a quadrilateral cell in the (x, y) plane with vertices at $(x_i, y_i), i = 1, 2, 3, 4$ (Figure 9.11). The region $(-1 < \eta < 1, -1 < \xi < 1)$ can be mapped into the quadrilateral using the transformation

$$x = x_1 B_{22} + x_2 B_{12} + x_3 B_{11} + x_4 B_{21} \quad (9.65)$$

$$y = y_1 B_{22} + y_2 B_{12} + y_3 B_{11} + y_4 B_{21} \quad (9.66)$$

where B_{11}, B_{12}, B_{21} , and B_{22} are the bilinear basis functions defined in (9.47)–(9.50). The transformation can be written in expanded form as

$$\begin{aligned} x = & \frac{1}{4}[\eta\xi(x_1 - x_2 + x_3 - x_4) + \eta(x_1 - x_2 - x_3 + x_4) \\ & + \xi(x_1 + x_2 - x_3 - x_4) + (x_1 + x_2 + x_3 + x_4)] \end{aligned} \quad (9.67)$$

$$\begin{aligned} y = & \frac{1}{4}[\eta\xi(y_1 - y_2 + y_3 - y_4) + \eta(y_1 - y_2 - y_3 + y_4) \\ & + \xi(y_1 + y_2 - y_3 - y_4) + (y_1 + y_2 + y_3 + y_4)] \end{aligned} \quad (9.68)$$

An application of the chain rule produces

$$\begin{bmatrix} \frac{\partial}{\partial \eta} \\ \frac{\partial}{\partial \xi} \end{bmatrix} = \begin{bmatrix} \frac{\partial x}{\partial \eta} & \frac{\partial y}{\partial \eta} \\ \frac{\partial x}{\partial \xi} & \frac{\partial y}{\partial \xi} \end{bmatrix} \begin{bmatrix} \frac{\partial}{\partial x} \\ \frac{\partial}{\partial y} \end{bmatrix} = \mathbf{J} \begin{bmatrix} \frac{\partial}{\partial x} \\ \frac{\partial}{\partial y} \end{bmatrix} \quad (9.69)$$

where \mathbf{J} is the Jacobian of the transformation from the (η, ξ) system to the (x, y) system. For the mapping in (9.67) and (9.68), the matrix \mathbf{J} has the form

$$\mathbf{J} = \frac{1}{4} \begin{bmatrix} \xi(x_1 - x_2 + x_3 - x_4) + (x_1 - x_2 - x_3 + x_4) & \xi(y_1 - y_2 + y_3 - y_4) + (y_1 - y_2 - y_3 + y_4) \\ \eta(x_1 - x_2 + x_3 - x_4) + (x_1 + x_2 - x_3 - x_4) & \eta(y_1 - y_2 + y_3 - y_4) + (y_1 + y_2 - y_3 - y_4) \end{bmatrix} \quad (9.70)$$

An explicit expression for the bilinear basis functions in the (x, y) -coordinate system may be unnecessary, since knowledge of the linear behavior along cell edges is often sufficient for visualization purposes. However, a finite-element implementation requires a convenient way of computing the 4×4 element matrices, and again we seek a local evaluation directly in the (η, ξ) system.

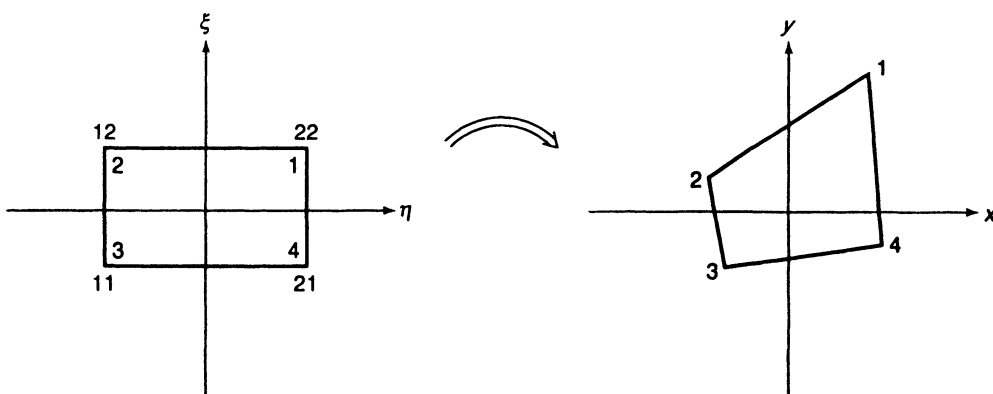


Figure 9.11 Mapping from a reference cell to a quadrilateral cell.

Using

$$dx dy = (\det \mathbf{J}) d\eta d\xi \quad (9.71)$$

the entries of (9.26) are given by

$$A_{pq}^{(2)} = \int_x \int_y B_p B_q dx dy = \int_{\eta=-1}^1 \int_{\xi=-1}^1 B_p B_q (\det \mathbf{J}) d\eta d\xi \quad (9.72)$$

where $\det \mathbf{J}$ is generally a function of (η, ξ) and cannot be extracted from the integrand. The evaluation of

$$A_{pq}^{(1)} = \int_x \int_y \left[\frac{\partial B_p}{\partial x} \frac{\partial B_p}{\partial y} \right] \begin{bmatrix} \frac{\partial B_q}{\partial x} \\ \frac{\partial B_q}{\partial y} \end{bmatrix} dx dy \quad (9.73)$$

requires the Jacobian of the inverse mapping, that is,

$$\begin{bmatrix} \frac{\partial}{\partial x} \\ \frac{\partial}{\partial y} \end{bmatrix} = \begin{bmatrix} \frac{\partial \eta}{\partial x} & \frac{\partial \xi}{\partial x} \\ \frac{\partial \eta}{\partial y} & \frac{\partial \xi}{\partial y} \end{bmatrix} \begin{bmatrix} \frac{\partial}{\partial \eta} \\ \frac{\partial}{\partial \xi} \end{bmatrix} = \mathbf{J}^{-1} \begin{bmatrix} \frac{\partial}{\partial \eta} \\ \frac{\partial}{\partial \xi} \end{bmatrix} \quad (9.74)$$

Since the mapping defines x and y in terms of η and ξ , it is usually easier to compute \mathbf{J}^{-1} from \mathbf{J} at the necessary quadrature points by matrix inversion than it is to construct \mathbf{J}^{-1} from the explicit inverse transformation. It follows that

$$A_{pq}^{(1)} = \int_{\eta=-1}^1 \int_{\xi=-1}^1 \left[\frac{\partial B_p}{\partial \eta} \frac{\partial B_p}{\partial \xi} \right] \mathbf{J}^{-T} \mathbf{J}^{-1} \begin{bmatrix} \frac{\partial B_q}{\partial \eta} \\ \frac{\partial B_q}{\partial \xi} \end{bmatrix} (\det \mathbf{J}) d\eta d\xi \quad (9.75)$$

Once the integrals are recast into the (η, ξ) system, (9.72) and (9.75) may be evaluated by numerical quadrature.

We have considered a bilinear mapping in order to create basis functions on quadrilateral cells with straight sides. For numerical stability, the transformation must map points in (η, ξ) uniquely to points in (x, y) and vice versa and must not allow interior angles of the quadrilateral to approach or exceed 180° . A similar procedure will be used in the following section in order to produce basis functions on cells with curved sides.

9.4 SCALAR BASIS FUNCTIONS FOR TWO-DIMENSIONAL CELLS WITH CURVED SIDES

Higher order polynomial basis functions generally produce better accuracy than simple functions at a modest additional cost. However, improvements in interpolation accuracy can be offset by errors in modeling the region of interest, especially if the geometry has curved boundaries. These modeling errors can be reduced by the use of basis functions defined on cells with curved sides. Parametric basis functions can be obtained by a mapping procedure similar to that introduced in Section 9.3 to generate basis functions for quadrilateral cells. The bilinear transformation used in Section 9.3 maps straight lines into straight lines. In this section, we consider a quadratic transformation capable of mapping straight lines into parabolic curves.

Figure 9.12 depicts a distorted triangular cell. The figure also shows six nodes, denoted by the triple index (i, j, k) introduced in Section 9.1. The curved geometry can be described by a transformation from simplex coordinates (L_1, L_2, L_3) to the (x, y) system

$$x = \sum_{i=0}^2 \sum_{j=0}^2 x_{ijk} B_{ijk}(L_1, L_2, L_3) \quad (9.76)$$

$$y = \sum_{i=0}^2 \sum_{j=0}^2 y_{ijk} B_{ijk}(L_1, L_2, L_3) \quad (9.77)$$

where (x_{ijk}, y_{ijk}) are the coordinates of the appropriate nodes, $\{B_{ijk}\}$ are the six quadratic functions defined in (9.15)–(9.20), and $k = 2 - i - j$. The cell shape defined by this transformation is entirely determined by the six-node coordinates, and the sides have at most a parabolic curvature.

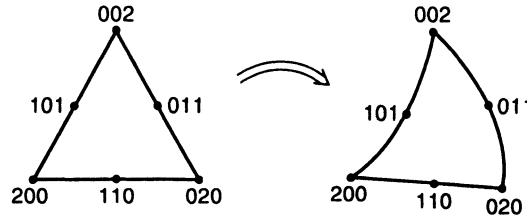


Figure 9.12 Mapping from a reference cell to a curved triangular cell.

Quadratic basis functions of the Lagrangian type may be defined on the curved cell using the same transformation, that is, (9.76) and (9.77). The use of quadratic basis functions on a cell whose shape is defined by a quadratic mapping is known as an *isoparametric* expansion. (In contrast, our previous use of quadratic Lagrangian functions on a triangular cell is a *subparametric* expansion.) Since the cell shapes are defined by the required nodes, the isoparametric expansion on a curved-cell mesh imposes no additional bookkeeping to describe the model beyond that required for the same order expansion on a triangular-cell mesh.

Using $L_1 + L_2 + L_3 = 1$, the transformation can be written entirely in terms of the variables L_1 and L_2 to produce

$$\begin{aligned} x &= x_{002} + L_1(4x_{101} - 3x_{002} - x_{200}) + L_2(4x_{011} - 3x_{002} - x_{020}) \\ &\quad + L_1^2(2x_{200} + 2x_{002} - 4x_{101}) + L_1 L_2(4x_{002} + 4x_{110} - 4x_{101} - 4x_{011}) \\ &\quad + L_2^2(2x_{020} + 2x_{002} - 4x_{011}) \end{aligned} \quad (9.78)$$

$$\begin{aligned} y &= y_{002} + L_1(4y_{101} - 3y_{002} - y_{200}) + L_2(4y_{011} - 3y_{002} - y_{020}) \\ &\quad + L_1^2(2y_{200} + 2y_{002} - 4y_{101}) + L_1 L_2(4y_{002} + 4y_{110} - 4y_{101} - 4y_{011}) \\ &\quad + L_2^2(2y_{020} + 2y_{002} - 4y_{011}) \end{aligned} \quad (9.79)$$

The chain rule dictates that

$$\left[\begin{array}{c} \frac{\partial}{\partial L_1} \\ \frac{\partial}{\partial L_2} \end{array} \right] = \mathbf{J} \left[\begin{array}{c} \frac{\partial}{\partial x} \\ \frac{\partial}{\partial y} \end{array} \right] \quad (9.80)$$

where

$$\mathbf{J} = \begin{bmatrix} \frac{\partial x}{\partial L_1} & \frac{\partial y}{\partial L_1} \\ \frac{\partial x}{\partial L_2} & \frac{\partial y}{\partial L_2} \end{bmatrix} \quad (9.81)$$

is the Jacobian matrix. The entries of \mathbf{J} are given by

$$\begin{aligned} \frac{\partial x}{\partial L_1} &= 4x_{101} - 3x_{002} - x_{200} + L_1(4x_{200} + 4x_{002} - 8x_{101}) \\ &\quad + L_2(4x_{002} + 4x_{110} - 4x_{101} - 4x_{011}) \end{aligned} \quad (9.82)$$

$$\begin{aligned} \frac{\partial y}{\partial L_1} &= (4y_{101} - 3y_{002} - y_{200}) + L_1(4y_{200} + 4y_{002} - 8y_{101}) \\ &\quad + L_2(4y_{002} + 4y_{110} - 4y_{101} - 4y_{011}) \end{aligned} \quad (9.83)$$

$$\begin{aligned} \frac{\partial x}{\partial L_2} &= (4x_{011} - 3x_{002} - x_{020}) + L_1(4x_{002} + 4x_{110} - 4x_{101} - 4x_{011}) \\ &\quad + L_2(4x_{020} + 4x_{002} - 8x_{011}) \end{aligned} \quad (9.84)$$

$$\begin{aligned} \frac{\partial y}{\partial L_2} &= (4y_{011} - 3y_{002} - y_{020}) + L_1(4y_{002} + 4y_{110} - 4y_{101} - 4y_{011}) \\ &\quad + L_2(4y_{020} + 4y_{002} - 8y_{011}) \end{aligned} \quad (9.85)$$

Required integrals for element matrices associated with the scalar Helmholtz operations can be obtained directly in the (L_1, L_2) system using

$$A_{pq}^{(1)} = \int_x \int_y \left[\frac{\partial B_p}{\partial x} \frac{\partial B_p}{\partial y} \right] \begin{bmatrix} \frac{\partial B_q}{\partial x} \\ \frac{\partial B_q}{\partial y} \end{bmatrix} dx dy \quad (9.86)$$

$$= \int_{L_1} \int_{L_2} \left[\frac{\partial B_p}{\partial L_1} \frac{\partial B_p}{\partial L_2} \right] \mathbf{J}^{-T} \mathbf{J}^{-1} \begin{bmatrix} \frac{\partial B_q}{\partial L_1} \\ \frac{\partial B_q}{\partial L_2} \end{bmatrix} (\det \mathbf{J}) dL_1 dL_2$$

$$A_{pq}^{(2)} = \int_x \int_y B_p B_q dx dy \quad (9.87)$$

$$= \int_{L_1} \int_{L_2} B_p B_q (\det \mathbf{J}) dL_1 dL_2$$

where \mathbf{J}^{-1} is the inverse of \mathbf{J} . The integrals in (9.86) and (9.87) are generally computed by numerical quadrature. Of course, for numerical stability the mapping from the (L_1, L_2, L_3) system to the (x, y) system must be one to one, and the interior angles of the distorted triangle must not approach or exceed 180° [8]. In addition, the location of the midside nodes must not deviate much from the halfway point along the edges of the curved cell; see Prob. P9.10 and reference [8].

A similar transformation can be used to define distorted nine-node quadrilateral cells (Figure 9.13) and map quadratic Lagrangian functions to those domains. The mapping has the form

$$x = \sum_{i=1}^3 \sum_{j=1}^3 x_{ij} B_{ij}(\eta, \xi) \quad (9.88)$$

$$y = \sum_{i=1}^3 \sum_{j=1}^3 y_{ij} B_{ij}(\eta, \xi) \quad (9.89)$$

where (x_{ij}, y_{ij}) are the coordinates of the appropriate nodes and $\{B_{ij}\}$ are the nine quadratic functions defined throughout the standard cell $(-1 < \eta < 1, -1 < \xi < 1)$ in Equations (9.56)–(9.64). The associated Jacobian relationship and element matrix entries can be obtained by calculations similar to those in (9.80)–(9.87). As an aid to implementation, a FORTRAN subroutine providing the element matrices associated with an eight-node quadrilateral expansion is available in reference [2]. (The eight-node expansion is slightly different from the nine-node Lagrangian basis used here.)

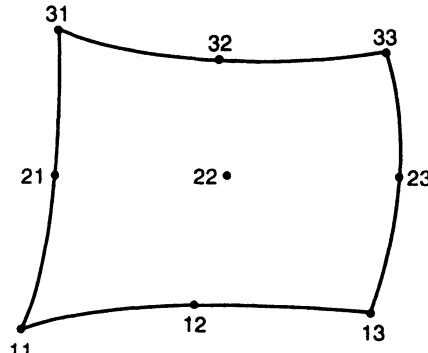


Figure 9.13 A nine-node curved quadrilateral cell.

Because of the straightforward nature of the transformation, curved cells are widely used when discretizing second-order differential equations [1, 2]. Scalar isoparametric expansions on curved cells have also been investigated for use with volume integral equation formulations [9, 10]. These formulations often require the integration of singular functions, and systematic procedures for treating the most common singularities have been developed [9]. The procedure can also be applied to create curved cells for surface integral equation discretizations, as illustrated in the following section.

9.5 DISCRETIZATION OF TWO-DIMENSIONAL SURFACE INTEGRAL EQUATIONS USING AN ISOPARAMETRIC QUADRATIC REPRESENTATION [11]

Chapters 2 and 6 presented a number of two-dimensional discretization schemes employing flat-cell models of the cylinder contours and piecewise-constant or piecewise-linear basis functions. The scatterer models can be improved by using cells with parabolic curvature. Suppose t is a parametric variable with the interval $-1 \leq t \leq 1$ used to describe a single cell. The cell can be defined by the three points (x_1, y_1) , (x_2, y_2) , and (x_3, y_3) , and the mapping

$$x(t) = x_1 B_1(t) + x_2 B_2(t) + x_3 B_3(t) \quad (9.90)$$

$$y(t) = y_1 B_1(t) + y_2 B_2(t) + y_3 B_3(t) \quad (9.91)$$

where

$$B_1(t) = \frac{1}{2}t(t - 1) \quad (9.92)$$

$$B_2(t) = 1 - t^2 \quad (9.93)$$

$$B_3(t) = \frac{1}{2}t(t + 1) \quad (9.94)$$

are the quadratic Lagrangian functions defined in Section 5.3. It is convenient to also use quadratic Lagrangian interpolation polynomials to represent the surface current density (an isoparametric expansion). For the TM polarization, the current density within a cell can be replaced by

$$J_z(t) \cong \sum_{n=1}^3 j_n B_n(t) \quad -1 \leq t \leq 1 \quad (9.95)$$

Consider the TM EFIE and the use of Dirac delta testing functions to complete the discretization. The entries of the system matrix involve integrals of the form

$$I_{mn}^{\text{cell } p} = \frac{k\eta}{4} \int_{\text{cell } p} B_n(t') H_0^{(2)}(kR_m) J(t') dt' \quad (9.96)$$

where m and n now denote global indices,

$$R_m = \sqrt{[x_m - x(t')]^2 + [y_m - y(t')]^2} \quad (9.97)$$

and J is the Jacobian

$$J(t) = \sqrt{\left(\frac{dx}{dt}\right)^2 + \left(\frac{dy}{dt}\right)^2} \quad (9.98)$$

The Jacobian can be evaluated using the mapping in (9.90) and (9.91), which yields

$$\frac{dx}{dt} = \left(\frac{x_3 - x_1}{2}\right) + (x_1 - 2x_2 + x_3)t \quad (9.99)$$

$$\frac{dy}{dt} = \left(\frac{y_3 - y_1}{2}\right) + (y_1 - 2y_2 + y_3)t \quad (9.100)$$

within a particular cell. In general, the integrals defined by (9.96) must be evaluated by numerical quadrature. In the case where R_m vanishes within the interval of integration, the integral can be evaluated by the procedures described in Chapter 2 or Appendix A.

Because the Lagrangian functions interpolatory at the intercell nodes (x_1, y_1) or (x_3, y_3) actually span two cells, two integrals of the general form (9.96) are required for each matrix entry. Functions interpolatory at the interior point (x_2, y_2) are confined to a single cell, and the corresponding matrix entries are limited to a single integral of the form (9.96).

For the TE MFIE, a similar discretization can be developed. The off-diagonal matrix entries involve integrals of the form

$$I_{mn}^{\text{cell } p} = \frac{k}{4j} \int_{\text{cell } p} B_n(t') \left(\sin \Omega(t') \frac{x_m - x(t')}{R_m} - \cos \Omega(t') \frac{y_m - y(t')}{R_m} \right) H_1^{(2)}(kR_m) J(t') dt' \quad (9.101)$$

where J is defined in (9.98), R_m is defined in (9.97), and Ω denotes the angle defined in Section 2.2 (except that Ω is now a continuous function since the cells are curved). If

node m lies at an intercell node, the diagonal matrix entries have the form

$$Z_{mm} = -\frac{\Gamma_m}{2\pi} + I_{mm}^{\text{cell } p} + I_{mm}^{\text{cell } q} \quad (9.102)$$

where Γ_m denotes the total interior wedge angle formed by the conductor at node m and $I_{mm}^{\text{cell } p}$ and $I_{mm}^{\text{cell } q}$ have the form of (9.101), except that a small region in the vicinity of node m is excluded from the integral. If node m lies in the cell interior, the associated diagonal entries are

$$Z_{mm} = -\frac{1}{2} + I_{mm}^{\text{cell } p} \quad (9.103)$$

where again a small region around node m is excluded from the integral.

To illustrate the accuracy of the isoparametric Lagrangian approach, Table 9.3 shows the TE surface current density induced on a circular cylinder by a uniform plane wave. Results are repeated from Table 2.8 for comparison. For 40 unknowns/ λ , there is a consistent improvement in accuracy as the basis function order is increased.

TABLE 9.3 Comparison of Current Density Induced on Circular Cylinder with Circumference $1\lambda_0$ by TE Plane Wave Propagating in $\phi = 0$ Direction

ϕ (deg)	Magnitude				Phase (deg)			
	MFIE Pulse Basis, Flat Cells	MFIE Linear Basis, Flat Cells	MFIE Quadratic Basis, Parabolic Cells	Exact	MFIE Pulse Basis, Flat Cells	MFIE Linear Basis, Flat Cells	MFIE Quadratic Basis, Parabolic Cells	Exact
	0	0.8907	0.8891	0.8883	0.8882	66.29	66.66	66.56
45	0.6733	0.6729	0.6722	0.6722	113.41	113.57	113.56	113.56
90	1.1751	1.1708	1.1714	1.1713	-164.88	-164.80	-164.82	-164.82
135	1.6232	1.6201	1.6199	1.6199	-125.83	-125.82	-125.84	-125.84
180	1.7094	1.7076	1.7073	1.7071	-110.77	-110.82	-110.83	-110.83

Note: MFIE results obtained with pulse, linear, and quadratic basis functions are compared with the exact solution for a 40-unknown discretization. The quadratic case employs parabolic cells defined by (9.90) and (9.91); the other results were obtained using flat cells. After [11].

9.6 SCALAR LAGRANGIAN FUNCTIONS IN THREE DIMENSIONS [1, 2]

The rectangular/quadrilateral-cell scalar Lagrangian functions introduced in Section 9.3 can be easily extended to the three-dimensional situation in order to represent fields using hexahedral cell shapes [1]. We will leave the full development of these functions as an exercise for the reader. The representation on tetrahedrons is perhaps somewhat more complicated, because of the use of simplex coordinates, and we briefly summarize it below.

Consider a point (x, y, z) within a tetrahedron. The point divides the cell into four smaller tetrahedra, each with a volume that is some fraction of the total. Simplex coordinates (L_1, L_2, L_3, L_4) may be defined by the respective ratio of the volume of each of the smaller

cells to that of the original. Equivalently,

$$x = L_1 x_1 + L_2 x_2 + L_3 x_3 + L_4 x_4 \quad (9.104)$$

$$y = L_1 y_1 + L_2 y_2 + L_3 y_3 + L_4 y_4 \quad (9.105)$$

$$z = L_1 z_1 + L_2 z_2 + L_3 z_3 + L_4 z_4 \quad (9.106)$$

where (x_i, y_i, z_i) is the coordinate of vertex i . Since the sum of the volumes of the smaller cells must equal that of the original tetrahedron,

$$1 = L_1 + L_2 + L_3 + L_4 \quad (9.107)$$

A Cartesian representation may be obtained from

$$\begin{bmatrix} L_1 \\ L_2 \\ L_3 \\ L_4 \end{bmatrix} = \begin{bmatrix} x_1 & x_2 & x_3 & x_4 \\ y_1 & y_2 & y_3 & y_4 \\ z_1 & z_2 & z_3 & z_4 \\ 1 & 1 & 1 & 1 \end{bmatrix}^{-1} \begin{bmatrix} x \\ y \\ z \\ 1 \end{bmatrix} \quad (9.108)$$

and written in the form

$$L_i = \frac{1}{6V} (a_i + b_i x + c_i y + d_i z) \quad (9.109)$$

We leave the task of constructing the explicit Cartesian representation to the reader.

Lagrangian expansion functions having polynomial order M can be defined on tetrahedral cells containing m regularly spaced nodes, where

$$m = \frac{1}{6}(M+1)(M+2)(M+3) \quad (9.110)$$

In terms of a quadruple index (i, j, k, l) , subject to $i + j + k + l = M$, these nodes are located at

$$(L_1, L_2, L_3, L_4) = \left(\frac{i}{M}, \frac{j}{M}, \frac{k}{M}, \frac{l}{M} \right) \quad (9.111)$$

Basis functions can be defined in general according to

$$B_{ijkl}(L_1, L_2, L_3, L_4) = R_i(M, L_1)R_j(M, L_2)R_k(M, L_3)R_l(M, L_4) \quad (9.112)$$

where $R_s(M, L)$ is the auxiliary polynomial defined in Equations (9.11) and (9.12). The function B_{ijkl} has unity value at node $ijkl$ and vanishes at every other node in the cell.

There are 4 linear functions ($M = 1$) spanning a cell. These have the simple representation

$$B_i = L_i \quad (9.113)$$

A quadratic representation requires the superposition of 10 functions. The 4 quadratic functions that interpolate to the corner nodes can be expressed as

$$B_i = (2L_i - 1)L_i \quad (9.114)$$

The 6 remaining quadratic functions interpolate to nodes located in the middle of each edge and are given by

$$B_{1100} = 4L_1 L_2 \quad (9.115)$$

$$B_{1010} = 4L_1 L_3 \quad (9.116)$$

$$B_{1001} = 4L_1 L_4 \quad (9.117)$$

$$B_{0101} = 4L_2 L_4 \quad (9.118)$$

$$B_{0110} = 4L_2 L_3 \quad (9.119)$$

$$B_{0011} = 4L_3 L_4 \quad (9.120)$$

Basis functions of cubic and greater order may be constructed using Equation (9.112).

The scalar Lagrangian functions for hexahedral or tetrahedral cells are widely used in electrostatic and acoustic applications, where the primary unknowns are scalar in nature. Since the primary unknowns in three-dimensional electromagnetic applications are usually vector functions, a scalar representation can only be employed if each component is represented independently. In addition, if the electric or magnetic field is the primary unknown, it is generally necessary to permit jump discontinuities at medium interfaces. Since the Lagrangian functions impose continuity between cells, they have limited applicability in three-dimensional problems. However, they can be used if the primary unknowns are auxiliary vector potential functions instead of the fields [12]. When used to model electric or magnetic fields, even if the primary unknown field is a continuous function throughout the region of interest, there are difficulties with a Lagrangian representation. The following section illustrates some of the difficulties and provides the motivation for special vector basis functions developed in Sections 9.8 and 9.9.

9.7 SCALAR LAGRANGIAN DISCRETIZATION OF THE VECTOR HELMHOLTZ EQUATION FOR CAVITIES: SPURIOUS EIGENVALUES AND OTHER DIFFICULTIES

To illustrate several drawbacks associated with the scalar representation of vector quantities, we consider a discretization of the curl–curl form of the vector Helmholtz equation

$$\nabla \times \left(\frac{1}{\varepsilon_r} \nabla \times \bar{H} \right) = k^2 \mu_r \bar{H} \quad (9.121)$$

within a two-dimensional cavity containing material with relative permittivity $\varepsilon_r(x, y)$ and constant relative permeability μ_r . The cavity interior Γ is bounded by perfect electric walls. Here, \bar{H} denotes the transverse magnetic field

$$\bar{H} = \hat{x} H_x + \hat{y} H_y \quad (9.122)$$

throughout cavity interior. By multiplying (9.121) with a transverse testing function \bar{T} and employing the vector identities

$$\bar{T} \cdot \nabla \times \bar{H} = \nabla \times \bar{T} \cdot \bar{H} - \nabla \cdot (\bar{T} \times \bar{H}) \quad (9.123)$$

$$(\bar{T} \times \bar{H}) \cdot \hat{n} = -\bar{T} \cdot (\hat{n} \times \bar{H}) \quad (9.124)$$

and the divergence theorem

$$\iint_{\Gamma} \nabla \cdot (\bar{T} \times \bar{H}) dx dy = \int_{\partial\Gamma} (\bar{T} \times \bar{H}) \cdot \hat{n} dt \quad (9.125)$$

the vector Helmholtz equation can be recast as the weak equation

$$\begin{aligned} \iint_{\Gamma} \frac{1}{\epsilon_r} \nabla \times \bar{T} \cdot \nabla \times \bar{H} dx dy &= k^2 \iint_{\Gamma} \mu_r \bar{T} \cdot \bar{H} dx dy \\ &\quad - \int_{\partial\Gamma} \frac{1}{\epsilon_r} \bar{T} \cdot \hat{n} \times (\nabla \times \bar{H}) dt \end{aligned} \quad (9.126)$$

where $\partial\Gamma$ denotes the cavity boundary. Along perfect electric walls, the magnetic field must satisfy the natural boundary condition

$$\hat{n} \times \nabla \times \bar{H} = 0 \quad (9.127)$$

which eliminates the boundary integral on the right-hand side of (9.126). The remainder of (9.126) constitutes an eigenvalue equation for the resonant wavenumber k and the eigenfunction \bar{H} associated with the TM cavity modes. Note that the TM cavity modes are also described by the scalar Helmholtz equation for E_z ; here we deliberately investigate the vector formulation to gain an appreciation for issues that do not arise in the scalar case.

Assuming that the cavity cross section is modeled with triangular cells, each with constant μ_r and ϵ_r , consider an independent expansion for the x - and y -components of the magnetic field according to

$$H_x(x, y) \cong \sum_{n=1}^N h_{xn} B_n(x, y) \quad (9.128)$$

$$H_y(x, y) \cong \sum_{n=1}^N h_{yn} B_n(x, y) \quad (9.129)$$

where B_n denotes a Lagrangian expansion function (Section 9.1) interpolatory at node n . The Lagrangian functions provide a continuous expansion and would not be suitable for representing the transverse magnetic field in regions where μ_r exhibits jump discontinuities. The restriction to continuous μ_r is one limitation of this specific scalar discretization.

Following common practice, we choose testing functions identical to the basis functions and therefore test the equation with independent functions $\hat{x}T_{xn} = \hat{x}B_{xn}$ and $\hat{y}T_{yn} = \hat{y}B_{yn}$. This procedure produces the generalized matrix eigenvalue equation

$$\begin{bmatrix} A^{11} & A^{12} \\ A^{21} & A^{22} \end{bmatrix} \begin{bmatrix} H_x \\ H_y \end{bmatrix} = k^2 \begin{bmatrix} B^{11} & 0 \\ 0 & B^{22} \end{bmatrix} \begin{bmatrix} H_x \\ H_y \end{bmatrix} \quad (9.130)$$

with entries

$$A_{mn}^{11} = \frac{1}{\epsilon_r} \iint \nabla \times \bar{T}_{xm} \cdot \nabla \times \bar{B}_{xn} dx dy \quad (9.131)$$

$$A_{mn}^{12} = \frac{1}{\epsilon_r} \iint \nabla \times \bar{T}_{xm} \cdot \nabla \times \bar{B}_{yn} dx dy \quad (9.132)$$

$$A_{mn}^{21} = \frac{1}{\epsilon_r} \iint \nabla \times \bar{T}_{ym} \cdot \nabla \times \bar{B}_{xn} dx dy \quad (9.133)$$

$$A_{mn}^{22} = \frac{1}{\epsilon_r} \iint \nabla \times \bar{T}_{ym} \cdot \nabla \times \bar{B}_{yn} dx dy \quad (9.134)$$

$$B_{mn}^{11} = \mu_r \iint \bar{T}_{xm} \cdot \bar{B}_{xn} dx dy \quad (9.135)$$

$$B_{mn}^{22} = \mu_r \iint \bar{T}_{ym} \cdot \bar{B}_{yn} dx dy \quad (9.136)$$

where all integrals are over the region Γ .

Suppose we employ linear-order Lagrangian functions within each cell, that is,

$$T_{xm} = B_{xm} = T_{ym} = B_{ym} = L_m \quad m = 1, 2, 3 \quad (9.137)$$

where $\{L_i\}$ are defined in Section 9.1. Using Equation (9.4), we observe that

$$\nabla \times \bar{T}_{xm} = \nabla \times \bar{B}_{xm} = -\hat{z} \frac{\partial L_m}{\partial y} = -\hat{z} \frac{c_m}{2A} \quad (9.138)$$

$$\nabla \times \bar{T}_{ym} = \nabla \times \bar{B}_{ym} = \hat{z} \frac{\partial L_m}{\partial x} = \hat{z} \frac{b_m}{2A} \quad (9.139)$$

and with (9.37) and (9.40) immediately obtain the element matrix entries for a single cell as

$$A_{mn}^{11} = \frac{1}{4A\varepsilon_r} c_m c_n \quad (9.140)$$

$$A_{mn}^{12} = \frac{-1}{4A\varepsilon_r} c_m b_n \quad (9.141)$$

$$A_{mn}^{21} = \frac{-1}{4A\varepsilon_r} b_m c_n \quad (9.142)$$

$$A_{mn}^{22} = \frac{1}{4A\varepsilon_r} b_m b_n \quad (9.143)$$

and

$$B_{mn}^{11} = B_{mn}^{22} = \mu_r \iint L_m L_n dx dy = \mu_r \begin{cases} \frac{1}{6}A & m = n \\ \frac{1}{12}A & \text{otherwise} \end{cases} \quad (9.144)$$

where $\{b_i\}$ and $\{c_i\}$ are defined in (9.6) and (9.7) and A denotes the cell area.

Since there are two unknown coefficients (h_{xn} and h_{yn}) associated with each node of the triangular-cell mesh, the boundary condition in (9.127) is not sufficient to uniquely determine the solution. We must also enforce the Dirichlet condition

$$\hat{n} \cdot \bar{H} = 0 \quad (9.145)$$

on the boundary $\partial\Gamma$. The process of enforcing Equation (9.145) would be trivial if the basis set happened to separate into normal and tangential components along $\partial\Gamma$, since the appropriate coefficient could simply be set to zero. Instead, the coefficients in (9.128) and (9.129) are associated with the x - and y -components, and the formulation is complicated by the fact that for a general boundary orientation (9.145) couples several coefficients together.

The entries of the finite-element system in (9.140)–(9.144) are each purely local in character. In contrast, the essential boundary condition in (9.145) acts as a constraint on the global system. Suppose that the normal vector to the boundary is given by

$$\hat{n} = \hat{x} \cos \theta + \hat{y} \sin \theta \quad (9.146)$$

where $\theta(t)$ is an ordinary polar angle defined along $\partial\Gamma$. At any point along the boundary, Equation (9.145) can be written as

$$H_x \cos \theta + H_y \sin \theta = 0 \quad (9.147)$$

which is a constraint between the x - and y -components of the field. If enforced at a node on the boundary, (9.147) involves two coefficients; if imposed along a cell edge, it involves four coefficients. In order to implement this type of constraint in a manner that systematically

reduces the rank of the matrix eigensystem, we rewrite Equation (9.130) as

$$\mathbf{A}_{2N \times 2N} \mathbf{h}_{2N \times 1} = k^2 \mathbf{B}_{2N \times 2N} \mathbf{h}_{2N \times 1} \quad (9.148)$$

Suppose that there are $2N - M$ constraints from (9.147). These can be collected together in matrix form as

$$\mathbf{h}_{2N \times 1} = \mathbf{C}_{2N \times M} \tilde{\mathbf{h}}_{M \times 1} \quad (9.149)$$

where $\tilde{\mathbf{h}}$ contains the M coefficients to be retained in the eigensystem. Equation (9.149) can be used to reduce the original $2N \times 2N$ system to the $M \times M$ eigensystem

$$\mathbf{C}_{M \times 2N}^T \mathbf{A}_{2N \times 2N} \mathbf{C}_{2N \times M} \tilde{\mathbf{h}}_{M \times 1} = k^2 \mathbf{C}_{M \times 2N}^T \mathbf{B}_{2N \times 2N} \mathbf{C}_{2N \times M} \tilde{\mathbf{h}}_{M \times 1} \quad (9.150)$$

The process of implementing Equation (9.145) does not require the explicit matrix operations indicated above; instead rows and columns can be combined in order to impose one constraint at a time. However, this type of global constraint is always much more cumbersome to implement than the local constraints encountered in our previous study of scalar finite-element methods (e.g., Chapter 3, Sections 8.6 and 9.2) and substantially complicates a sparse storage scheme. The need to impose global conditions is a consequence of the fact that the primary unknowns represent the x - and y -field components, instead of tangential and normal components of the field at cell edges, and is a second limitation of this specific discretization.

After the eigensystem in Equation (9.130) is constructed and reduced to (9.150), the resulting generalized eigenvalue equation can be solved by standard algorithms [13]. However, the results are far from satisfactory. Table 9.4 shows the smallest resonant wavenumbers generated by this procedure for a homogeneous, circular cavity of unit radius. The triangular-cell model contained 31 nodes, producing an original eigensystem of rank 62 that was reduced to a system of rank 44 after imposing the essential boundary condition in (9.145). From an inspection of Table 9.4, it is clear that most of the numerical eigenvalues are incorrect. Interestingly, the solutions do not improve with smaller cells. In this case, the numerical data are not just inaccurate but are completely corrupted by the presence of spurious eigenvalues and eigenfunctions. The few values that appear to represent true wavenumbers are interspersed with spurious eigenvalues and are impossible to identify without extensive postprocessing.

In summary, we have identified three difficulties with the approach outlined in Equations (9.128)–(9.150): the inability of this expansion to model discontinuous magnetic material, the cumbersome procedure needed to implement the essential boundary condition, and (by far the most serious) the appearance of spurious eigenfunctions and eigenvalues in the spectrum of the discrete operator.

The source of the “spurious” eigenvalues in Table 9.4 is the curl–curl operator itself, which admits eigenfunctions that do not satisfy the complete set of Maxwell’s equations. In fact, the eigenfunctions of this equation can generally be separated into two families, one of which is a valid electromagnetic field and the other of which has the form $\{\vec{H} = \nabla\Phi\}$. Both eigenfamilies satisfy the boundary conditions as well as the Helmholtz equation. The gradient $\nabla\Phi$ is a valid mathematical solution to (9.121) for $k = 0$, since $\nabla \times \nabla\Phi = 0$, but is not required to satisfy Gauss’ law

$$\nabla \cdot (\mu_0 \mu_r \vec{H}) = 0 \quad (9.151)$$

Therefore, $\nabla\Phi$ cannot represent a time-varying magnetic field in a source-free region. Since their associated eigenvalues are zero, eigenfunctions of this form comprise the *nullspace* of

TABLE 9.4 Smallest TM Resonant Wavenumbers for Homogeneous Circular (Two-Dimensional) Cavity of Unit Radius Produced by Equation (9.150)

Numerical	Exact
0.00 (5)	2.405 (TM_{01})
0.49 (2)	3.832 (TM_{11})
0.73 (2)	5.136 (TM_{21})
1.13 (2)	5.520 (TM_{02})
1.47 (1)	6.380 (TM_{31})
2.40 (2)	7.016 (TM_{12})
2.47 (1)	7.588 (TM_{41})
2.59 (2)	8.417 (TM_{22})
3.25 (1)	•
4.12 (2)	•
4.51 (1)	•
5.56 (2)	
5.67 (2)	
6.37 (1)	
7.06 (1)	
7.20 (1)	
7.75 (2)	
8.00 (2)	
•	
•	

Note: Numerical solutions are obtained using piecewise-linear Lagrangian interpolation functions. The cavity model consists of a relatively coarse triangular-cell mesh with 31 nodes and 42 cells and produced an eigensystem of order 44. The resonant wavenumbers are listed in order of increasing values with their degree of multiplicity in parentheses. The boldface results are believed to represent the first four genuine solutions; the rest appear to be spurious.

the curl–curl operator. Problem P9.13 illustrates an example of nullspace eigenfunctions for a rectangular cavity.

The solution family $\{\nabla\Phi\}$ is of interest, even when k is not zero, because a general discretization of the Helmholtz operator will capture eigenfunctions from both families (Section 5.7). In other words, unless the basis functions are orthogonal to all functions in the nullspace, a matrix representing the curl–curl operator will have some eigenvectors that approximate those functions. The difficulty is that the spurious eigenvalues in Table 9.4 are not zero, apparently a consequence of the fact that the low-order Lagrangian basis cannot adequately represent the nullspace eigenfunctions. It has been reported that fifth-order polynomial expansions do adequately model the nullspace eigenfunctions and produce associated eigenvalues of zero [14]. (A fifth-order representation has enough degrees of freedom so that the function, its tangential derivative, and its normal derivative are independent at cell boundaries; refer to the discussion at the end of Section 9.1.) It has also been observed that representations not imposing normal-field continuity between cells produce the correct nullspace eigenvalues of zero [14, 15]. It appears that relaxing the continuity conditions (by only imposing tangential continuity) also alleviates one of

the other difficulties encountered above, namely that the resulting expansion can represent jump discontinuities in the normal-field components at material interfaces.

It is of interest to consider properties of the nullspace eigensolutions in more detail. First, note that both eigensolution families must maintain tangential continuity across any mathematical boundary, and in the absence of medium discontinuities the true electromagnetic fields are expected to exhibit normal continuity. However, the nullspace functions $\{\nabla\Phi\}$ may exhibit jump discontinuities in their normal component, even in homogeneous media, while still maintaining the property that $\nabla \times \nabla\Phi = 0$. As an illustration, the function

$$\bar{H}^{\text{spurious}} = \begin{cases} (1-y)\hat{x} + (1-x)\hat{y} & (\text{quadrant 1}) \\ (y-1)\hat{x} + (1+x)\hat{y} & (\text{quadrant 2}) \\ -(1+y)\hat{x} - (1+x)\hat{y} & (\text{quadrant 3}) \\ (1+y)\hat{x} + (x-1)\hat{y} & (\text{quadrant 4}) \end{cases} \quad (9.152)$$

defined in the usual quadrants of the x - y plane is the gradient of a scalar function and has identically zero curl. This function can be terminated discontinuously at $x = \pm 1$ and $y = \pm 1$, as though it resided on a square-cell mesh surrounding the origin and had its domain of support truncated to these cells. The resulting function (Figure 9.14) is a nullspace eigenfunction of the curl-curl operator for electric wall boundary conditions applied at some location removed from these cells or magnetic wall boundary conditions applied at $x = \pm 1$ and $y = \pm 1$. Note that Equation (9.152) has a strong discontinuity at the origin in addition to the discontinuous normal component at the cell edges. Although (9.152) has zero curl, its projection onto a continuous basis set does not (Prob. P9.14). If the field expansion permits discontinuous normal components, functions similar to (9.152) are observed in the set of numerical eigenfunctions.

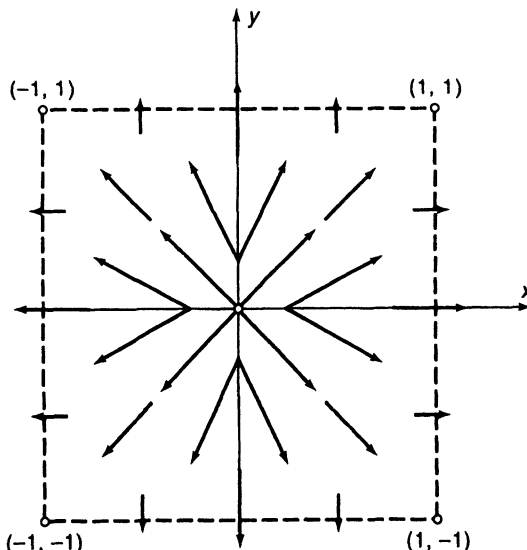


Figure 9.14 Discontinuous vector function defined in (9.152).

In summary, we conclude that a discretization of the vector Helmholtz equation (9.121) should employ a basis set that imposes tangential continuity but not normal continuity between cells. On a fine enough mesh, such an expansion should be able to accurately represent the lower order electromagnetic eigenfunctions in continuous or discontinuous

media as well as the nullspace eigenfunctions. The following sections will investigate the performance of several vector basis sets of this type. In the finite-element literature, basis functions that maintain continuity between cells are known as *conforming* functions. Similarly, vector basis functions that only impose tangential continuity between cells have been described as *curl conforming* [16].

9.8 POLYNOMIAL-COMPLETE VECTOR BASIS FUNCTIONS THAT IMPOSE TANGENTIAL CONTINUITY BUT NOT NORMAL CONTINUITY BETWEEN TRIANGULAR CELLS [17]

The previous section identified several difficulties associated with the use of Lagrangian-type interpolation polynomials to independently represent the Cartesian components of the vector function. The major difficulty is that associated with the continuity of the representation: The expansion functions should impose tangential continuity but not normal continuity. A second difficulty identified in Section 9.7 is the cumbersome imposition of boundary conditions at general interfaces when the primary unknowns are the Cartesian components of the vector field. The second difficulty can be eliminated by developing basis functions with coefficients that represent the normal or tangential components along cell edges. In this section, a polynomial-complete family of vector basis functions are described with these properties.

Consider a triangular cell in the x - y plane and an associated vector basis function expressed as a linear polynomial

$$\bar{B}(x, y) = \hat{x}(A + Bx + Cy) + \hat{y}(D + Ex + Fy) \quad (9.153)$$

The six coefficients provide six degrees of freedom in the expansion, and we are free to impose six conditions on the representation in order to generate specific basis functions. For triangular cells, this might translate into two constraints per edge or two constraints per corner node. By appropriate constraints, several different basis sets can be obtained from Equation (9.153).

For instance, suppose we constrain the tangential component of the basis function \bar{B} to equal unity at one node of a cell edge while simultaneously vanishing at the opposite node. In addition, the tangential component along the other two edges can be constrained to vanish at both nodes of each edge (and therefore vanish entirely along both edges). Since the basis function is at most linear, these six constraints completely specify its shape within the triangle. Five other basis functions can be defined in a similar fashion to produce a set of six that each interpolate to the tangential component along one end of an edge (Figure 9.15). These basis functions can be forced to maintain tangential continuity between cells by the simple expedient of sharing coefficients with the analogous functions in the adjacent cell. From a global perspective, each basis function straddles two triangular cells and interpolates to the tangential component along one end of the common edge. Thus, there are a total of two basis functions per edge throughout the model. The normal component of each global basis function is discontinuous at the common edge, and therefore these functions do not impose normal continuity between cells. The simplex-coordinate representation of these basis functions within a cell is given by

$$w_i L_j \nabla L_k \quad i \neq j \neq k \quad (9.154)$$

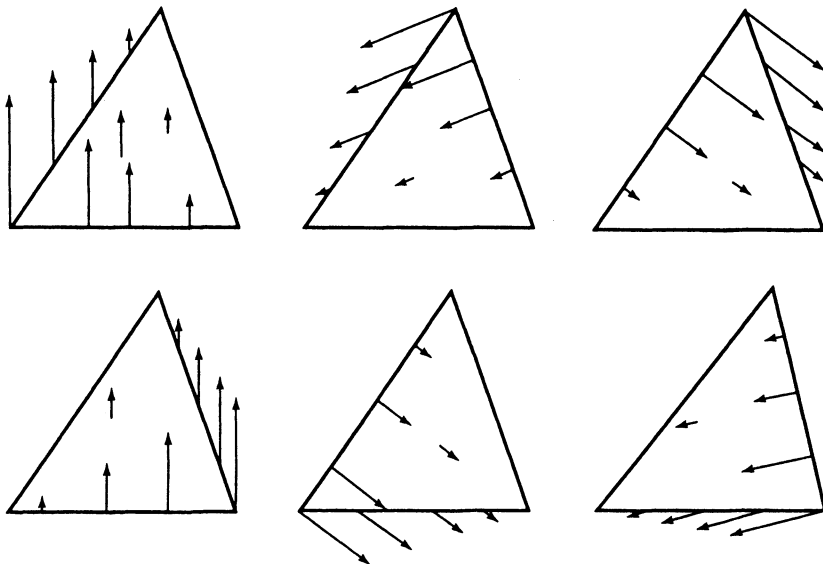


Figure 9.15 Set of six polynomial-complete curl-conforming linear vector basis functions.

where w_i denotes the length of the edge opposite node i , and i, j , and k assume values between 1 and 3. The normalization in (9.154) is investigated in Prob. P9.16.

Since the coefficients of the vector basis functions in (9.154) represent the tangential component along cell edges, boundary conditions such as $\hat{n} \times \vec{E} = 0$ can be implemented in a purely local fashion by zeroing the appropriate coefficient. Therefore, these basis functions make it easier to incorporate essential boundary conditions into the solution process. Although these functions are complete to linear polynomial order, they do not produce the same representation as a linear Lagrangian expansion of the Cartesian vector components since they are not completely continuous between cells. Consequently, there are more degrees of freedom (and more unknowns) associated with the vector functions than with the usual Lagrangian expansion on the same mesh. However, as demonstrated below, the vector basis functions in (9.154) eliminate the spurious nonzero eigenvalues encountered in Section 9.7.

Analogous basis functions can be created that provide a complete quadratic representation. An expansion of the form

$$\begin{aligned}\bar{B}(x, y) = & \hat{x}(A + Bx + Cy + Dx^2 + Exy + Fy^2) \\ & + \hat{y}(G + Hx + Iy + Jx^2 + Kxy + Ly^2)\end{aligned}\quad (9.155)$$

contains 12 degrees of freedom, and basis functions can be defined that interpolate to the tangential components at three locations along each edge of a triangular cell and the normal component at the middle of each edge. For instance, in simplex coordinates, we can define six functions of the form

$$w_i L_j (2L_j - 1) \nabla L_k \quad i \neq j \neq k \quad (9.156)$$

that interpolate to a unity tangential component at the outside nodes of each edge, three functions of the form

$$2w_i L_j L_k (\nabla L_j - \nabla L_k) \quad i \neq j \neq k \quad (9.157)$$

that interpolate to a unity tangential component at the midside nodes, and three functions of the form

$$L_i L_j \nabla L_k \quad i \neq j \neq k \quad (9.158)$$

that provide a linearly independent normal component along each edge. The three functions in (9.158) are not interpolatory, since in general the functions of (9.157) also contribute a normal component at the midside nodes. The possible normalization of (9.158) is left as an exercise, as is the task of sketching the set of 12 functions (Prob. P9.17).

To maintain tangential continuity between cells, the nine quadratic basis functions in (9.156) and (9.157) share coefficients with the analogous functions in the adjacent cells. The three basis functions per cell in (9.158) are entirely local and thus have coefficients that are independent from those of the neighboring cells. Consequently, the normal component can be discontinuous between cells. The global representation produced by the quadratic functions requires three unknowns per edge and three unknowns per cell.

Table 9.5 shows numerical eigenvalues produced when the basis functions from (9.154) and (9.156)–(9.158) are used to discretize the vector Helmholtz equation

$$\nabla \times \left(\frac{1}{\mu_r} \nabla \times \bar{E} \right) - k^2 \epsilon_r \bar{E} = 0 \quad (9.159)$$

for a circular, homogeneous cavity bounded by a p.e.c. wall. The solution procedure can be organized along the lines of the previous finite-element formulations; that is, the field can be represented by an expansion

$$\bar{E}(x, y) \cong \sum_{n=1}^N e_n \bar{B}_n(x, y) \quad (9.160)$$

where \bar{B}_n denotes a vector expansion function and is substituted into the weak vector

TABLE 9.5 Smallest Eigenvalues Produced by Discretization of Circular Cavity with $\epsilon_r = 1$, $\mu_r = 1$, and Unit Radius Using Polynomial-Complete Linear^a and Polynomial-Complete Quadratic^b Basis Functions for TE polarization

LT/LN	QT/QN	Exact
0.0 (67)	0.0 (163)	
1.87 (2)	1.84 (2)	1.841 (2)
3.20 (2)	3.06 (2)	3.054 (2)
4.13 (1)	3.84 (1)	3.832 (1)
4.6 (2)	4.21 (2)	4.201 (2)
6.0 (2)	5.35 (2)	5.318 (2)
6.1 (2)	5.37 (2)	5.331 (2)

^a LT/LN; from Equation (9.154).

^b QT/QN; from Equations (9.156)–(9.158).

Note: The model consisted of 42 triangular cells and resulted in a matrix of order 108 for the LT/LN functions and 288 for the QT/QN functions.

equation

$$\iint_{\Gamma} \left(\frac{1}{\mu_r} \nabla \times \bar{T} \cdot \nabla \times \bar{E} - k^2 \epsilon_r \bar{T} \cdot \bar{E} \right) dx dy = - \int_{\partial\Gamma} \frac{1}{\mu_r} \bar{T} \cdot \hat{n} \times (\nabla \times \bar{E}) dt \quad (9.161)$$

obtained in a manner analogous to (9.126). For the TE polarization, the boundary condition $\hat{n} \times \bar{E} = 0$ on the p.e.c. wall is enforced by omitting any basis function with a nonzero tangential value on the boundary from the system of equations. Since there are no basis functions remaining with nonzero tangential components along the boundary $\partial\Gamma$, there will be no need for testing functions with tangential components along $\partial\Gamma$ and the boundary integral in (9.161) will not contribute to the system. The discretization process yields a matrix eigenvalue equation $\mathbf{A}\mathbf{e} = k^2\mathbf{B}\mathbf{e}$ with entries

$$A_{mn} = \frac{1}{\mu_r} \iint \nabla \times \bar{T}_m \cdot \nabla \times \bar{B}_n dx dy \quad (9.162)$$

and

$$B_{mn} = \epsilon_r \iint \bar{T}_m \cdot \bar{B}_n dx dy \quad (9.163)$$

We will employ the same vector functions for expansion and testing.

In common with our previous finite-element implementations, the region of interest is divided into triangular cells, with the mesh terminating on the cavity boundary $\partial\Gamma$. The matrices \mathbf{A} and \mathbf{B} are constructed on a cell-by-cell basis using a connectivity array that identifies the rows and columns of the matrix associated with a particular cell. The ordinary connectivity array employed with “node-based” scalar finite-element analysis identifies the three nodes associated with each cell. However, the coefficients of the vector basis functions represent the tangential or normal fields along cell edges. In this “edge-based” formulation, it is much more convenient to employ a connectivity array that identifies the three edges associated with each cell. (A second pointer array is also necessary to identify the two nodes associated with each edge.) The matrices may be constructed by scanning through the global model, computing 6×6 element matrices from the integrals in (9.162)–(9.163) for the linear basis functions and 12×12 element matrices for the quadratic basis functions. The connectivity arrays identify the appropriate locations of the element matrix entries within the global system. To ensure that the basis functions (those that overlap two cells) have a common orientation on either side of a given edge, we adopt the convention that the vector basis functions tangential to an edge always point from the smaller node index to the larger node index, according to the global numbering. The details of the element matrix calculations for the functions of (9.154) are suggested in Prob. P9.18.

The nonzero eigenvalues in Table 9.5 appear to have a one-to-one correlation with analytical results for the electromagnetic cavity modes. The results also contain a large number of zero eigenvalues that represent the nullspace. Overall, these results support the hypothesis that the spurious eigenvalues observed previously can be eliminated by an expansion that only imposes tangential continuity between cells. In addition to remediating the spurious eigenvalue problem, the vector basis functions simplify the task of imposing boundary conditions since the coefficients directly represent the tangential field at the boundary. The polynomial-complete vector basis functions developed in (9.154) and (9.156)–(9.158) appear to be equivalent to those used in various electromagnetic applications previously described in the literature [17–19].

Unfortunately, Table 9.5 also shows that more than half of the available degrees of freedom in the vector expansions are used to capture nullspace eigensolutions. Since these

are nonphysical results, a substantial amount of computational effort is wasted. It would be desirable to eliminate some or all of these wasted degrees of freedom. The following section considers alternative vector basis functions that eliminate some of the nullspace eigenfunctions.

9.9 MIXED-ORDER VECTOR BASIS FUNCTIONS THAT IMPOSE TANGENTIAL BUT NOT NORMAL CONTINUITY FOR TRIANGULAR AND RECTANGULAR CELLS [16, 20]

As illustrated in Table 9.5, a polynomial-complete discretization of the curl–curl operator captures many nullspace eigensolutions. Some of the wasted degrees of freedom can be eliminated by the use of special mixed-order polynomial basis functions proposed in 1980 by Nedelec [16]. In common with the polynomial-complete functions used in Section 9.8, the mixed-order functions are curl conforming: They impose tangential continuity between cells but do not impose normal continuity. Thus, if used to discretize the curl–curl operator, they should not produce spurious nonzero eigenvalues.

Consider a vector representation for triangular cells. Within a cell, a complete linear representation has the form

$$\hat{x}(A + Bx + Cy) + \hat{y}(D + Ex + Fy) \quad (9.164)$$

Equation (9.164) can be decomposed into two parts, one with three degrees of freedom

$$\bar{B}(x, y) = \hat{x} \left(A + \frac{1}{2}[C - E]y \right) + \hat{y} \left(D + \frac{1}{2}[E - C]x \right) \quad (9.165)$$

and a complementary representation, also containing three degrees of freedom,

$$\bar{B}_{\text{grad}}(x, y) = \hat{x} \left(Bx + \frac{1}{2}[C + E]y \right) + \hat{y} \left(\frac{1}{2}[E + C]x + Fy \right) \quad (9.166)$$

The functions in (9.166) are actually the gradient of the quadratic-order function

$$\Phi(x, y) = \left(\frac{1}{2}Bx^2 + \frac{1}{2}[E + C]xy + \frac{1}{2}Fy^2 \right) \quad (9.167)$$

and therefore have identically zero curl within the cell. If functions of the form (9.166) are constrained to have tangential continuity from cell to cell, their curl will be identically zero over the entire problem domain. Therefore, if used to discretize the curl–curl operator, the degrees of freedom in (9.166) can only represent nullspace eigenfunctions. Furthermore, the linear degrees of freedom in (9.166) are not needed to balance terms in the discretized vector Helmholtz equation, since the curl of (9.165) only produces a constant. By restricting the basis set to the functions in (9.165) and discarding the degrees of freedom in (9.166), we obtain a vector representation with only half the unknowns as the polynomial-complete linear basis functions introduced in Section 9.7. Below, we demonstrate that the use of (9.165) reduces the number of nullspace eigensolutions by exactly the number of discarded degrees of freedom without a detrimental effect on accuracy.

Nedelec presented constraints that can be imposed on a polynomial-complete expansion of any order to produce the desired mixed-order representation. For the two-

dimensional linear case, the three constraints are [16]

$$\frac{\partial B_x}{\partial x} = 0 \quad \frac{\partial B_y}{\partial y} = 0 \quad \frac{\partial B_x}{\partial y} + \frac{\partial B_y}{\partial x} = 0 \quad (9.168)$$

which reduce (9.164) to (9.165). It is interesting to observe that the identical representation can be obtained from (9.164) and the constraint that the tangential component of the basis function \bar{B} equal unity at both endpoints of a common edge while simultaneously vanishing along the other two edges. In fact, within a triangular domain (9.165) is a vector function with a constant-tangential component along one edge and zero tangential component along the other two edges (Figure 9.16). There is also a nonzero normal component along each of the edges that varies linearly. Consequently, these basis functions provide a constant-tangential, linear-normal (CT/LN) representation of the field. To obtain tangential continuity between cells, the coefficients of the three basis functions can be shared by similar functions in the adjacent cells. In the global model, the support of this type of vector basis function would be the two triangles associated with each edge (Figure 9.16). These basis functions offer a simple approach for representing tangentially continuous vector quantities and have been widely used under the name “edge elements.” Although first introduced for finite-element formulations by Nedelec [16], they appear to have been developed independently by other researchers for magnetics applications [21, 22].

Within a cell, the CT/LN basis functions can be expressed in terms of the simplex coordinates as

$$\bar{B}_i = w_i (L_{i+1} \nabla L_{i+2} - L_{i+2} \nabla L_{i+1}) \quad (9.169)$$

where the index i denotes the edge opposite vertex i in the triangle and w_i denotes the length of edge i . These functions are oriented so that they point from node $i + 1$ to node $i + 2$ along edge i . Using the relation

$$\nabla L_i = \frac{1}{2A} (\hat{x} b_i + \hat{y} c_i) \quad (9.170)$$

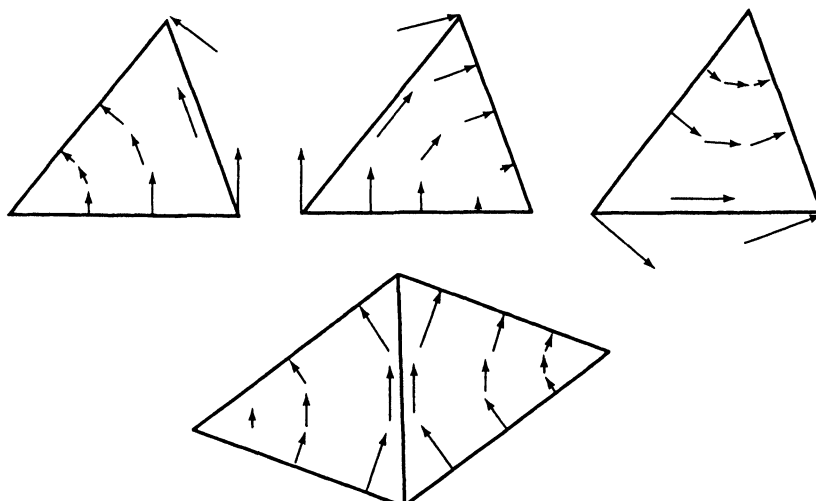


Figure 9.16 Constant tangential/linear normal (CT/LN) curl-conforming vector basis functions.

where b_i and c_i are defined in Section 9.1 and A is the cell area, we obtain the Cartesian representation

$$\begin{aligned}\bar{B}_i = \frac{w_i}{4A^2} & \{\hat{x}[a_j b_k - a_k b_j + (c_j b_k - c_k b_j)y] \\ & + \hat{y}[a_j c_k - a_k c_j + (b_j c_k - b_k c_j)x]\}\end{aligned}\quad (9.171)$$

confirming that (9.169) is equivalent to (9.165). We also observe that

$$\nabla \times \bar{B}_i = \hat{z} \frac{w_i}{2A^2} (b_j c_k - b_k c_j) = \pm \hat{z} \frac{w_i}{A} \quad (9.172)$$

and

$$\nabla \cdot \bar{B}_i = 0 \quad (9.173)$$

Thus, the CT/LN functions have constant curl and zero divergence within a cell. It is important to note, however, that because the normal component is discontinuous across edges, their divergence is not zero (or even finite) at cell boundaries. As an aid to visualization, consider a triangle having one node located at the origin of a polar coordinate system (ρ, ϕ) . The basis function oriented along the edge opposite the node at the origin can be written as

$$\bar{B}(\rho, \phi) = K\rho\hat{\phi} \quad (9.174)$$

where K is a normalization constant.

A similar procedure can be used to develop vector basis functions of higher polynomial orders. In the quadratic case, the polynomial-complete representation in (9.155) can be decomposed into an expansion

$$\begin{aligned}\bar{B}(x, y) = \hat{x} & \left(A + Bx + Cy + \frac{1}{3}[E - 2J]xy + \frac{1}{3}[2F - K]y^2 \right) \\ & + \hat{y} \left(G + Hx + Iy + \frac{1}{3}[2J - E]x^2 + \frac{1}{3}[K - 2F]xy \right)\end{aligned}\quad (9.175)$$

containing eight degrees of freedom and a complementary representation

$$\begin{aligned}\bar{B}_{\text{grad}}(x, y) = \hat{x} & \left(Dx^2 + \frac{2}{3}[E + J]xy + \frac{1}{3}[F + K]y^2 \right) \\ & + \hat{y} \left(\frac{1}{3}[E + J]x^2 + \frac{2}{3}[K + F]xy + Ly^2 \right)\end{aligned}\quad (9.176)$$

containing four degrees of freedom. Equation (9.176) is the gradient of a cubic-order function and consequently has identically zero curl. Therefore, those degrees of freedom can only represent functions in the nullspace of the curl-curl operator. Since they are not needed to balance terms in the discretized vector Helmholtz equation, they can be discarded to improve computational efficiency. Equation (9.175) can also be obtained from (9.155) by imposing the four conditions [16]

$$\frac{\partial^2 B_x}{\partial x^2} = 0 \quad (9.177)$$

$$\frac{\partial^2 B_y}{\partial y^2} = 0 \quad (9.178)$$

$$\frac{\partial^2 \mathbf{B}_x}{\partial y^2} + 2 \frac{\partial^2 \mathbf{B}_y}{\partial x \partial y} = 0 \quad (9.179)$$

$$\frac{\partial^2 \mathbf{B}_y}{\partial x^2} + 2 \frac{\partial^2 \mathbf{B}_x}{\partial x \partial y} = 0 \quad (9.180)$$

which eliminate the degrees of freedom associated with (9.176).

Equation (9.175) provides a linear-tangential, quadratic-normal (LT/QN) representation along any cut through a triangular cell. Several equivalent sets of LT/QN basis functions can be constructed. It is important to note that these functions should be distributed around the triangle in a symmetric way, and a symmetric distribution of eight basis functions may not be immediately obvious. One possibility is to define six basis functions that are entirely linear, having the simplex-coordinate description

$$w_i L_j \nabla L_k \quad i \neq j \neq k \quad (9.181)$$

where w_i denotes the length of the edge opposite node i . These are the polynomial-complete basis functions introduced in Section 9.8, and they provide the simplest way of interpolating to a linear-tangential component on the edges. The remaining two functions must provide a quadratic-normal component along three edges, and a suitable choice for these functions is

$$L_2 L_3 \nabla L_1 - L_1 L_2 \nabla L_3 \quad (9.182)$$

$$L_1 L_3 \nabla L_2 - L_1 L_2 \nabla L_3 \quad (9.183)$$

It can be verified that the functions in (9.182) and (9.183) satisfy the conditions in (9.177)–(9.180). These eight basis functions are depicted in Figure 9.17. The six functions in (9.181) interpolate to a unity-tangential component at the cell edges and will share a coefficient with similar functions in adjacent cells to maintain tangential continuity. The functions in (9.182) and (9.183) each contribute a quadratic-normal component to two of the three edges and have no tangential component along any of the edges. Their coefficients are independent of those in neighboring cells, allowing them to reproduce a discontinuity in the normal component of the vector field at cell junctions. Since the functions in (9.181) also contribute a nonzero normal component along the cell edges, (9.182) and (9.183) are not interpolatory.

To verify that the mixed-order basis functions in (9.169) and (9.181)–(9.183) provide a robust discretization of the curl–curl operator, we again consider a numerical solution of the vector Helmholtz equation (9.159) for a circular, homogeneous cavity bounded by a p.e.c. wall. The formulation parallels that of Equations (9.159)–(9.163) and produces a matrix eigenvalue equation $\mathbf{A}\mathbf{e} = k^2\mathbf{B}\mathbf{e}$. The boundary condition $\hat{n} \times \hat{\mathbf{E}} = 0$ is imposed along the p.e.c. wall by omitting from the system of equations those basis functions that represent the tangential electric field along the conductor. For the CT/LN basis and testing functions, the matrix entries in (9.162) and (9.163) can be evaluated on a cell-by-cell basis using the expressions

$$\begin{aligned} & \iint \nabla \times \bar{\mathbf{B}}_m \cdot \nabla \times \bar{\mathbf{B}}_n dx dy \\ &= \frac{w_m w_n}{4A^3} (b_{m+1} c_{m+2} - b_{m+2} c_{m+1})(b_{n+1} c_{n+2} - b_{n+2} c_{n+1}) \end{aligned} \quad (9.184)$$

$$\begin{aligned} & \iint \bar{\mathbf{B}}_m \cdot \bar{\mathbf{B}}_n dx dy \\ &= \frac{w_m w_n}{2A} \sum_{i=1}^2 \sum_{j=1}^2 \alpha_{ij} \beta_{mn}^{ij} (b_{m+3-i} b_{n+3-j} + c_{m+3-i} c_{n+3-j}) \end{aligned} \quad (9.185)$$

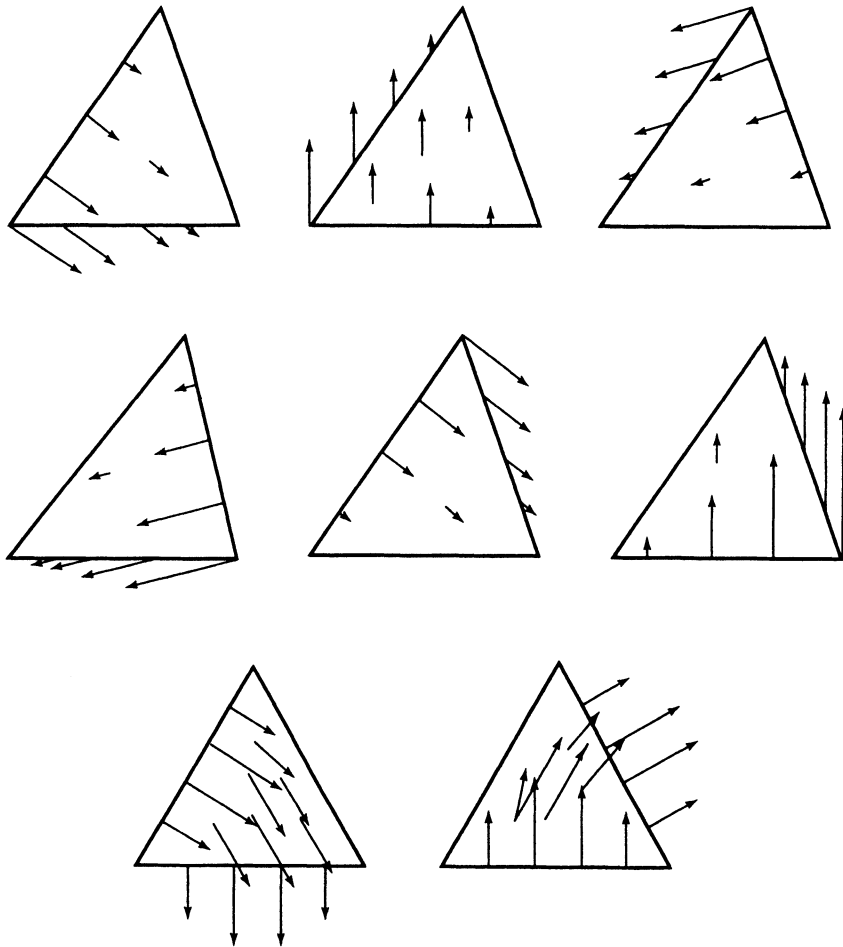


Figure 9.17 Set of eight linear tangential/quadratic normal (LT/QN) curl-conforming vector basis functions.

for the integrals over a single triangular cell, where w_i is the width of edge i , A is the cell area, $\{b_i\}$ and $\{c_i\}$ are defined in (9.6) and (9.7), and

$$\alpha_{ij} = \begin{cases} +1 & \text{if } i = j \\ -1 & \text{otherwise} \end{cases} \quad (9.186)$$

$$\beta_{mn}^{ij} = \begin{cases} \frac{1}{12} & \text{if } m + i = n + j \\ \frac{1}{24} & \text{otherwise} \end{cases} \quad (9.187)$$

The evaluation of element matrix entries for the LT/QN functions is left as an exercise. The generalized matrix eigenvalue equation is solved using standard techniques [13]. Table 9.6 presents numerical eigenvalues obtained using the CT/LN discretization for the identical cavity model used to generate Table 9.5. Results are also shown for the LT/QN functions from (9.181)–(9.183). The mixed-order vector basis functions clearly separate the true electromagnetic eigenvalues from the zero eigenvalues associated with the nullspace. Furthermore, the CT/LN results in Table 9.6 and the polynomial-complete linear results in Table 9.5 contain the same number of nonzero eigenvalues, but the CT/LN functions produce far

TABLE 9.6 Lowest Eigenvalues Produced by Discretization of Circular Cavity with $\epsilon_r = 1$, $\mu_r = 1$, and Unit Radius Using Mixed-Order Basis Functions for TE Polarization

CT/LN	LT/QN	Exact
0.0 (13)	0.0 (67)	
1.86 (2)	1.84 (2)	1.841 (2)
3.10 (2)	3.05 (2)	3.054 (2)
3.82 (1)	3.84 (1)	3.832 (1)
4.28 (2)	4.20 (2)	4.201 (2)
5.27 (2)	5.32 (2)	5.318 (2)
5.39 (2)	5.35 (2)	5.331 (2)

Note: The 42-cell model produced a matrix with order 54 for the CT/LN functions and 192 for the LT/QN functions.

fewer zero eigenvalues. The number of zero eigenvalues is reduced by exactly the number of basis functions excluded by imposing (9.168), which is half the original matrix order. The LT/QN results also contain the same number of nonzero eigenvalues but far fewer zero eigenvalues than produced by the polynomial-complete quadratic expansion in Table 9.5. For the LT/QN functions, the number of zero eigenvalues is reduced by exactly the number of basis functions excluded by imposing (9.177)–(9.180).

It is noteworthy that the six polynomial-complete linear basis functions in (9.154) form a subset of the LT/QN functions. By comparing Tables 9.5 and 9.6, we observe that the LT/QN expansion produces exactly the same number of zero eigenvalues as the complete linear expansion. This suggests that the additional basis functions used to build up the set of 8 LT/QN functions do not contribute to nullspace eigensolutions. However, their addition to the set of six polynomial-complete linear functions clearly improves the accuracy of the nonzero eigenvalues, as can be seen by comparing the LT/LN results in Table 9.5 with the LT/QN results in Table 9.6.

To illustrate the implementation of the CT/LN and LT/QN basis functions for the TM polarization, we repeat the circular cavity analysis while treating the transverse magnetic field as the unknown to be determined. The magnetic field can be represented as

$$\bar{H}(x, y) \cong \sum_{n=1}^N h_n \bar{B}_n(x, y) \quad (9.188)$$

and substituted into the weak equation defined in (9.126). For these expansion functions, the boundary condition $\hat{n} \times (\nabla \times \bar{H}) = 0$ along $\partial\Gamma$ eliminates the boundary integral in (9.126) and is sufficient. The resulting eigensystem has the matrix form $\mathbf{Ah} = k^2 \mathbf{Bh}$. Table 9.7 shows results obtained using CT/LN basis and testing functions with the element matrix entries presented in (9.184)–(9.187) for two different triangular-cell meshes. Eigenvalues obtained using LT/QN basis and testing functions are presented in Table 9.8. These results show that the different type of boundary condition imposed in the TM case does not affect the basic character of the numerical eigenvalues. For a given mesh, the LT/QN basis functions produce numerical eigenvalues that are more accurate than those of the CT/LN functions.

TABLE 9.7 Smallest TM Resonant Wavenumbers for Homogeneous Circular (Two-Dimensional) Cavity of Unit Radius Produced by Discretization of Equation (9.121) Using CT/LN Basis Functions

31-Node, 72-Edge Model	55-Node, 138-Edge Model	Exact
0.0 (30)	0.0 (54)	
2.45	2.42	2.405 (TM_{01})
3.87 (2)	3.85 (2)	3.832 (TM_{11})
5.08 (2)	5.14 (2)	5.136 (TM_{21})
5.41	5.50	5.520 (TM_{02})
6.14 (2)	6.36 (2)	6.380 (TM_{31})
6.32 (2)	6.91 (2)	7.016 (TM_{12})
7.13 (2)	7.49 (2)	7.588 (TM_{41})

Note: The resonant wavenumbers are listed in order of increasing values with their degree of multiplicity in parentheses.

TABLE 9.8 Smallest TM Resonant Wavenumbers for Homogeneous Circular (Two-Dimensional) Cavity of Unit Radius Produced by Discretization of Equation (9.121) Using LT/QN Basis Functions

31-Node, 72-Edge Model	55-Node, 138-Edge Model	Exact
0.0 (102)	0.0 (192)	
2.405	2.404	2.405 (TM_{01})
3.837 (2)	3.833 (2)	3.832 (TM_{11})
5.16 (2)	5.141 (2)	5.136 (TM_{21})
5.55	5.526	5.520 (TM_{02})
6.46 (2)	6.394 (2)	6.380 (TM_{31})
7.19 (2)	7.036 (2)	7.016 (TM_{12})
7.66 (2)	7.616 (2)	7.588 (TM_{41})

Note: The resonant wavenumbers are listed in order of increasing values with their degree of multiplicity in parentheses.

In summary, the triangular-cell CT/LN and LT/QN basis functions developed in this section enable a reduction in the degrees of freedom used to represent nullspace eigenolutions without reducing the number of true electromagnetic eigenfunctions. Furthermore, they appear to produce eigenvalues that are no less accurate than those obtained using a polynomial-complete expansion of comparable order.

Vector basis functions of greater polynomial order can be developed following the procedure described above and the analogous Nedelec constraints [16]. In general, a two-dimensional vector expansion of polynomial degree k will have $k(k+2)$ degrees of freedom remaining after eliminating the gradient of a higher polynomial order. For example, a general cubic-polynomial representation of a vector function in two-dimensions contains 20 degrees of freedom. There are 5 degrees of freedom associated with the gradient of a

fourth-order polynomial, which can be excluded to reduce the Cartesian form of the basis functions to

$$\begin{aligned}\bar{B}(x, y) = & \hat{x}(A + Bx + Cy + Dx^2 + Exy + Fy^2 + Gx^2y + Hxy^2 + 3Iy^3) \\ & + \hat{y}(J + Kx + Ly + Mx^2 + Nxy + Oy^2 - 3Gx^3 - Hx^2y - Ixy^2)\end{aligned}\quad (9.189)$$

Within a cell, one possible form of the 15 basis functions is given in simplex coordinates in Table 9.9. Nine of these functions interpolate to the tangential vector component along cell edges, while six functions build up the normal component. Together, these 15 basis functions provide a representation with quadratic-tangential and cubic-normal components (QT/CuN).

TABLE 9.9 Summary of Simplex-Coordinate Representation of First Three Types of Mixed-Order Basis Functions within Triangular Cell

CT/LN	LT/QN	QT/CuN
$L_1\nabla L_2 - L_2\nabla L_1$	$L_1\nabla L_2$	$L_2(2L_2 - 1)\nabla L_1$
$L_1\nabla L_3 - L_3\nabla L_1$	$L_2\nabla L_1$	$L_3(2L_3 - 1)\nabla L_1$
$L_2\nabla L_3 - L_3\nabla L_2$	$L_1\nabla L_3$	$L_1(2L_1 - 1)\nabla L_2$
	$L_3\nabla L_1$	$L_3(2L_3 - 1)\nabla L_2$
	$L_2\nabla L_3$	$L_1(2L_1 - 1)\nabla L_3$
	$L_3\nabla L_2$	$L_2(2L_2 - 1)\nabla L_3$
	$L_2L_3\nabla L_1 - L_1L_2\nabla L_3$	$L_2L_3(\nabla L_2 - \nabla L_3)$
	$L_1L_3\nabla L_2 - L_1L_2\nabla L_3$	$L_1L_3(\nabla L_3 - \nabla L_1)$
		$L_1L_2(\nabla L_1 - \nabla L_2)$
		$\nabla(L_1L_2L_3)$
		$L_2(2L_2 - 1)(L_3\nabla L_1 - L_1\nabla L_3)$
		$L_3(2L_3 - 1)(L_1\nabla L_2 - L_2\nabla L_1)$
		$L_1^2(L_2\nabla L_3 - L_3\nabla L_2)$
		$L_2^2(L_3\nabla L_1 - L_1\nabla L_3)$
		$L_3^2(L_1\nabla L_2 - L_2\nabla L_1)$

Note: The last two LT/QN and the last six QT/CuN functions are entirely local. The functions are not normalized.

The CT/LN, LT/QN, and QT/CuN basis functions for triangular cells are summarized in Table 9.9. Note that there are equivalent basis functions that differ from those presented here but still provide a representation consistent with Nedelec's spaces (Prob. P9.21 and [23]). On the other hand, there have been alternative mixed-order functions proposed in the literature [14, 24] that are not equivalent to those presented here and do not eliminate the same degrees of freedom associated with the nullspace of the curl operator.

Mixed-order basis functions for rectangular and quadrilateral cells are also possible and in fact were also originally proposed by Nedelec [16]. These functions have a different number of degrees of freedom and a different mathematical expression in Cartesian coordinates than those used on triangles. However, they are based on the common idea of discarding degrees of freedom associated with nullspace eigensolutions.

The mixed-order functions for triangular cells discard all the degrees of freedom associated with the gradient of a higher order polynomial function. In the case of rectangular cells, some of these degrees of freedom must be kept to provide a symmetric distribution of basis functions. For instance, consider the quadratic case. As an alternative to the

decomposition defined by (9.175) and (9.176), a quadratic expansion can be separated into

$$\bar{B}(x, y) = \hat{x}(A + Bx + Cy + Dxy + Ey^2) + \hat{y}(F + Gx + Hy + Ix^2 + Jxy) \quad (9.190)$$

and

$$\bar{B}_{\text{grad}}(x, y) = \hat{x}Kx^2 + \hat{y}Ly^2 \quad (9.191)$$

This decomposition eliminates 2 degrees of freedom, leaving 10 in (9.190). However, 12 degrees of freedom are required to build up an LT/QN component along the sides of a rectangular cell. The polynomial components in (9.191) do not contribute to an LT/QN behavior, and instead it is convenient to add two cubic-order degrees,

$$\hat{x}Kxy^2 + \hat{y}Lx^2y \quad (9.192)$$

to (9.190). The resulting function provides an LT/QN representation along the cell edges, although, unlike (9.175), this expansion is not purely LT/QN along any cut within a cell.

To develop specific vector basis functions, consider a standard rectangular cell ($-1 < \eta < 1$, $-1 < \xi < 1$). The mathematical form of the LT/QN functions obtained by combining (9.190) and (9.192) is equivalent to the 12 functions [16, 25]

$$\bar{B}_{ij}^\eta = \hat{\eta}\phi_i^{(1)}(\eta)\phi_j^{(2)}(\xi) \quad i = 1, 2 \quad j = 1, 2, 3 \quad (9.193)$$

$$\bar{B}_{ij}^\xi = \hat{\xi}\phi_i^{(2)}(\eta)\phi_j^{(1)}(\xi) \quad i = 1, 2, 3 \quad j = 1, 2, \quad (9.194)$$

where $\phi_j^{(N)}$ is an N th order Lagrangian polynomial, defined on the interval $[x_1, x_{N+1}]$ by

$$\phi_j^{(N)} = \frac{(x - x_1)(x - x_2) \cdots (x - x_{j-1})(x - x_{j+1}) \cdots (x - x_N)(x - x_{N+1})}{(x_j - x_1) \cdots (x_j - x_{j-1})(x_j - x_{j+1}) \cdots (x_j - x_{N+1})} \quad (9.195)$$

Figure 9.18 illustrates the arrangement of these functions. The six η -component functions in (9.193) can be written explicitly as

$$\bar{B}_{11}^\eta = \hat{\eta} \frac{1 - \eta}{2} \frac{(\xi - 1)\xi}{2} \quad (9.196)$$

$$\bar{B}_{12}^\eta = \hat{\eta} \frac{1 - \eta}{2} (1 - \xi)(1 + \xi) \quad (9.197)$$

$$\bar{B}_{13}^\eta = \hat{\eta} \frac{1 - \eta}{2} \frac{\xi(1 + \xi)}{2} \quad (9.198)$$

$$\bar{B}_{21}^\eta = \hat{\eta} \frac{1 + \eta}{2} \frac{(\xi - 1)\xi}{2} \quad (9.199)$$

$$\bar{B}_{22}^\eta = \hat{\eta} \frac{1 + \eta}{2} (1 - \xi)(1 + \xi) \quad (9.200)$$

$$\bar{B}_{23}^\eta = \hat{\eta} \frac{1 + \eta}{2} \frac{\xi(1 + \xi)}{2} \quad (9.201)$$

These basis functions produce an LT/QN component along each edge, similar to the LT/QN functions for triangular cells. The absence of the highest polynomial order in the principal vector direction is consistent with the discarded degrees of freedom in (9.191).

The four basis functions in (9.196), (9.198), (9.199), and (9.201) interpolate to tangential fields along the cell edges. To maintain tangential continuity, the coefficients of these four functions will be shared with similar functions tangential to the same edge in

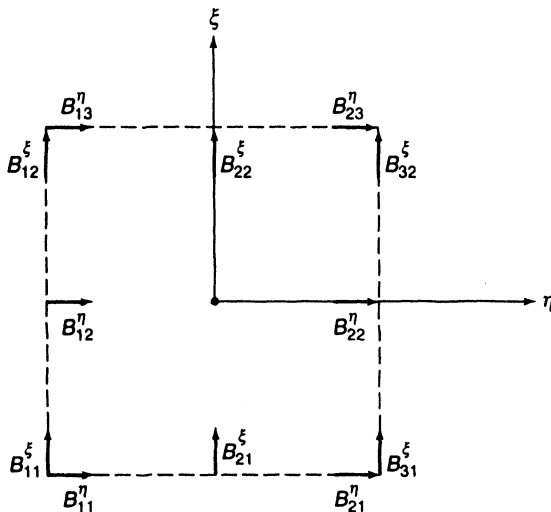


Figure 9.18 Locations of 12 LT/QN curl-conforming vector basis functions on a standard cell.

the adjacent cell. The functions \bar{B}_{12} and \bar{B}_{22} are associated with normal fields at the middle of the cell side, however, and will not share coefficients with neighboring cells. At a node where four cells come together in the global model, there will be four independent coefficients, one associated with the tangential field along each incoming or outgoing edge. Therefore, the rectangular-cell LT/QN expansion involves a total of two basis functions per edge and four additional basis functions per cell.

Similar basis functions can be developed that provide a CT/LN or QT/CuN representation [16, 25]. Table 9.10 summarizes the three lowest order functions for rectangular cells. Equivalent basis sets can be constructed that distribute the degrees of freedom in a different manner (Prob. P9.23 and [23]). As described in Section 9.14, a covariant mapping can be used to generalize these basis functions to quadrilateral or curvilinear cell shapes while preserving the property of tangential continuity between cells.

As indicated in Section 5.4, a subsectional basis function that is complete to polynomial order p provides a representation with interpolation error of $O(\Delta^{p+1})$ as $\Delta \rightarrow 0$, where Δ is the maximum cell dimension. These estimates also apply in general to the multidimensional vector case. Consequently, the polynomial-complete vector basis functions

TABLE 9.10 Summary of Local-Coordinate Representation of First Three Types of Mixed-Order Basis Functions within Rectangular Cell ($-1 < \eta < 1, -1 < \xi < 1$)

CT/LN	LT/QN	QT/CuN
$\hat{\eta}(1 \pm \xi)/2$	$\hat{\eta}(1 \pm \eta)\xi(\xi \pm 1)/4$	$\hat{\eta} \eta(\eta \pm 1)(\xi \pm 1)(\xi + 1/3)(\xi - 1/3) 9/32$
$\hat{\xi}(1 \pm \eta)/2$	$\hat{\xi}(1 \pm \xi)\eta(\eta \pm 1)/4$	$\hat{\xi} \xi(\xi \pm 1)(\eta \pm 1)(\eta + 1/3)(\eta - 1/3) 9/32$
	$\hat{\eta}(1 \pm \eta)(1 - \xi)(\xi + 1)/2$	$\hat{\eta} (\eta + 1)(\eta - 1)(\xi \pm 1)(\xi + 1/3)(\xi - 1/3) 9/16$
	$\hat{\xi}(1 \pm \xi)(1 - \eta)(\eta + 1)/2$	$\hat{\xi} (\xi + 1)(\xi - 1)(\eta \pm 1)(\eta + 1/3)(\eta - 1/3) 9/16$
		$\hat{\eta} \eta(\eta \pm 1)(\xi + 1)(\xi \pm 1/3)(\xi - 1) 27/32$
		$\hat{\xi} \xi(\xi \pm 1)(\eta + 1)(\eta \pm 1/3)(\eta - 1) 27/32$
		$\hat{\eta} (\eta + 1)(\eta - 1)(\xi + 1)(\xi \pm 1/3)(\xi - 1) 27/16$
		$\hat{\xi} (\xi + 1)(\xi - 1)(\eta + 1)(\eta \pm 1/3)(\eta - 1) 27/16$

Note: The last 4 LT/QN and last 12 QT/CuN functions are entirely local.

introduced in Section 9.8 are expected to provide $O(\Delta^{p+1})$ interpolation error. However, since the mixed-order vector basis functions of the present section are not complete to the highest polynomial order, the error analysis suggests that they provide one less order of interpolation accuracy. For instance, the LT/QN functions would be expected to provide $O(\Delta^2)$ accuracy as $\Delta \rightarrow 0$, not $O(\Delta^3)$.

However, data presented in the previous sections suggest that, when used within a discretization of the vector Helmholtz equation, the LT/QN functions actually provide slightly more accurate eigenvalues than the polynomial-complete quadratic basis functions (Tables 9.5 and 9.6). These results suggest that the interpolation error analysis might not take into account the nature of the discarded degrees of freedom in the mixed-order expansion. Consequently, it is possible that the analysis produces overly pessimistic conclusions when applied to the mixed-order functions.

In fact, a very different conclusion can be obtained from a dispersion analysis similar to that described in Section 5.5. The procedure considers the error associated with a uniform plane wave propagating in an arbitrary direction on an infinite regular mesh when the wave is represented by some type of basis function. Despite the complexity of dispersion analysis in the multidimensional case, some progress has been made in extending it to the two- and three-dimensional vector basis functions considered in this chapter [26, 27]. The results of this analysis show that mixed-order vector basis functions (containing orders up to $p - 1$ and p on triangles or tetrahedra and orders $p - 1$, p , and $p + 1$ on quadrilateral and hexahedral cells) appear to produce a discretization error of $O(\Delta^{p+1})$ when used to represent a plane wave. In common with scalar basis functions, the error appears entirely as phase error for electrically small cells in a homogeneous region, and the phase constant converges at the superconvergent rate of $O(\Delta^{2p})$. These findings confirm that the mixed-order vector basis functions are well suited for representing electromagnetic fields and suggest that the pessimistic result of the interpolation error analysis should be discounted, at least in source-free regions.

A dispersion analysis permits a direct comparison of the efficiency of several different expansions. Warren compared the CT/LN and LT/QN representations for triangular and quadrilateral cells (Tables 9.9 and 9.10) with the polynomial-complete representation in (9.154) [27]. Table 9.11 shows the unknown density needed to limit the phase error to $0.1 \text{ deg}/\lambda$ in the worst-case direction for an infinite square-cell mesh. For the triangular-cell expansions, the square cells are divided diagonally, with all the diagonals running in the same direction. Despite the fact that such a triangular-cell mesh produces relatively large errors in the worst-case direction, the triangular-cell expansions are about as efficient as the quadrilateral-cell expansions. For high accuracies, the quadratic-order basis functions are far more efficient than the linear-order basis functions. It is interesting that the polynomial-complete expansion from (9.154) requires four times as many unknowns to produce dispersion error as low as that of the CT/LN representation for triangles.

The curl-conforming vector basis functions introduced in this section eliminate some of the degrees of freedom associated with the nullspace of the curl–curl operator. One might wonder if the entire nullspace could be eliminated. The answer is yes, but the process of separating the nullspace involves global matrix operations that may not be compatible with sparse matrix storage and will generally prevent a purely local approach to constructing the finite-element system. For example, Manges and Cendes propose a partitioning based on the tree and cotree of the finite-element mesh [28]. A similar partitioning can be constructed by combining the standard mixed-order basis functions into *loop* and *star* functions, as suggested by Wilton [29]. Each loop function encircles a cell of the mesh, while star functions

TABLE 9.11 Approximate Cell Size Δ and Unknown Density Required to Limit Phase Error to 0.1 deg/ λ for Plane-Wave Dispersion Analysis

Basis Function Type	Δ	Unknowns/ λ^2
LT/LN, triangular, (9.154)	0.013λ	35570
CT/LN, quadrilateral	0.013λ	11860
CT/LN, triangular	0.018λ	8880
LT/QN, quadrilateral	0.127λ	246
LT/QN, triangular	0.140λ	307

Note: Several two-dimensional vector representations are compared on an infinite mesh of $\Delta \times \Delta$ square cells divided diagonally into triangular cells. The unknown density calculation assumes that the interior LT/QN unknowns are eliminated. Adapted from Warren's data [27].

are directed outward from each node. In the simplest case, the loop and star functions are a linear combination of the standard CT/LN functions and provide an equivalent representation. The star functions have zero curl and exhibit a one-to-one correspondence with nullspace eigenfunctions. However, either approach to eliminating the nullspace requires matrix transformations similar in form to (9.148)–(9.150) to collapse the system order to the non-nullspace eigenrank.

The use of the mixed-order vector basis functions described in this section resolves the three difficulties identified in Section 9.7. Not only do these functions eliminate the spurious nonzero eigenvalues, but boundary conditions are easy to incorporate since the coefficients are primarily associated with tangential fields at cell edges. Because they permit a jump discontinuity in the normal field, they place no restriction on the medium continuity from cell to cell. Furthermore, the mixed-order nature of these functions suppresses some of the degrees of freedom associated with the nullspace of the curl operator, enhancing their efficiency for modeling fields in source-free regions. In the following sections, we demonstrate that these functions are also easily adapted to scattering and waveguide formulations.

9.10 TE SCATTERING USING THE VECTOR HELMHOLTZ EQUATION WITH CT/LN AND LT/QN VECTOR BASIS FUNCTIONS DEFINED ON TRIANGULAR CELLS [30]

Prior to attacking a three-dimensional formulation (Chapter 11), we will consider the use of curl-conforming vector basis functions for discretizing the vector Helmholtz equation for TE scattering from infinite, inhomogeneous cylinders. Although a scalar formulation is likely to be more efficient for the two-dimensional situation, we turn to the vector formulation in order to study issues associated with the three-dimensional problem without the computational requirements of three-dimensional analysis. Since the use of CT/LN and LT/QN functions has already been demonstrated for cavity analysis, the principal focus of this section is the incorporation of an RBC into the formulation. We would also like to explore the extent to which these vector basis functions can represent jump discontinuities in the normal-field components at medium interfaces.

The curl–curl form of the vector Helmholtz equation for \bar{E} can be written as

$$\nabla \times \left(\frac{1}{\mu_r} \nabla \times \bar{E} \right) - k^2 \epsilon_r \bar{E} = 0 \quad (9.202)$$

We will develop an outward-looking formulation incorporating a local RBC. Following a procedure similar to that used to develop the scalar Bayliss–Turkel conditions in Section 3.8, we seek an RBC that forces the scattered field to have the form of the asymptotic expansion

$$\bar{E}^s(\rho, \phi) \cong \frac{e^{-jk\rho}}{\sqrt{\rho}} \sum_{n=0}^{\infty} \frac{\bar{E}_n(\phi)}{\rho^n} \quad (9.203)$$

It is easily verified that the condition

$$\hat{\rho} \times \nabla \times \bar{E}^s = \hat{\phi} \left(jk - \frac{1}{2\rho} \right) E_\phi^s \quad (9.204)$$

forces the scattered field to agree with the first two terms in (9.203). A second-order RBC can be obtained as

$$\left(\hat{\rho} \times (\nabla \times \cdot) - jk - \frac{3}{2\rho} \right) \left(\hat{\rho} \times (\nabla \times \bar{E}^s) - jk \bar{E}_\phi^s + \frac{1}{2\rho} \bar{E}_\phi^s \right) = 0 \quad (9.205)$$

and, using (9.202), can be rewritten as

$$\hat{\rho} \times \nabla \times \bar{E}^s = \alpha(\rho) \bar{E}_\phi^s + \frac{jk - 1/2\rho}{2jk + 2/\rho} \nabla^{\text{tan}}(\hat{\rho} \cdot \bar{E}^s) \quad (9.206)$$

where

$$\alpha(\rho) = \frac{-2k^2 + jk/\rho - 1/4\rho^2}{2jk + 2/\rho} \quad (9.207)$$

Equation (9.206) forces the scattered field to agree with the first four terms in the preceding expansion and reduces the error to $O(\rho^{-9/2})$. However, the single derivative in this RBC gives rise to a nonsymmetric matrix operator when incorporated into the weak form of the vector Helmholtz equation. Consequently, after observing

$$E_\rho = \frac{1}{k^2} \hat{\rho} \cdot \nabla \times \nabla \times \bar{E} = -\frac{1}{k^2} \nabla \cdot (\hat{\rho} \times \nabla \times \bar{E}) \quad (9.208)$$

we are motivated to substitute the RBC recursively into itself to recast the first-order derivative into a second-order derivative [31]. Neglecting higher order terms, the result can be written as

$$\hat{n} \times \nabla \times \bar{E}^s = \alpha(\rho) \bar{E}_\phi^s + \beta(\rho) \frac{\partial^2 \bar{E}_\phi^s}{\partial \phi^2} \quad (9.209)$$

where $\alpha(\rho)$ is defined in (9.207) and

$$\beta(\rho) = -\frac{\alpha(\rho)}{k^2 \rho^2} \frac{jk - 1/2\rho}{2jk + 2/\rho} \quad (9.210)$$

The RBC in (9.209) is to be imposed on a circular boundary of radius ρ , as illustrated in Figure 9.19. After combining this RBC with the incident field and substituting the result

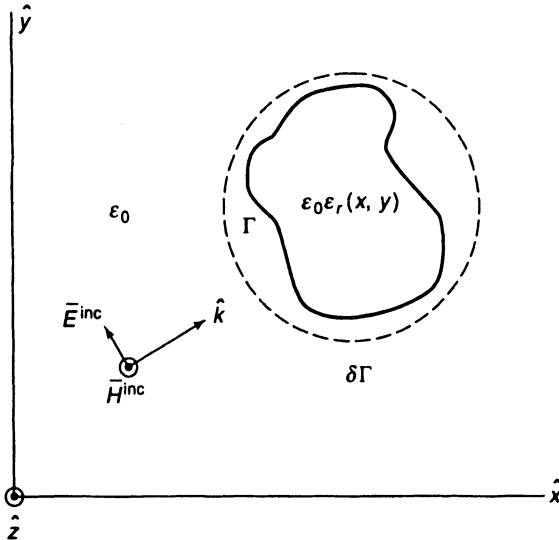


Figure 9.19 Cross section of an inhomogeneous cylinder enclosed within a mathematical radiation boundary $\partial\Gamma$. After [30]. ©1994 IEEE.

into the weak equation associated with (9.202), we obtain

$$\begin{aligned} & \iint_{\Gamma} \left(\frac{1}{\mu_r} \nabla \times \bar{T} \cdot \nabla \times \bar{E} - k^2 \epsilon_r \bar{T} \cdot \bar{E} \right) dx dy + \int_{\partial\Gamma} \left(\alpha \bar{T} \cdot \bar{E}_\phi - \beta \rho^2 \frac{\partial T_\phi}{\partial t} \frac{\partial E_\phi}{\partial t} \right) dt \\ &= - \int_{\partial\Gamma} \bar{T} \cdot \left(\hat{n} \times \nabla \times \bar{E}^{inc} - \alpha \bar{E}_\phi^{inc} - \beta \frac{\partial^2 \bar{E}_\phi^{inc}}{\partial \phi^2} \right) dt \end{aligned} \quad (9.211)$$

as the equation describing the scattering problem.

Within the region Γ , the unknown electric field can be expressed in terms of the vector expansion

$$\bar{E}(x, y) \cong \sum_{n=1}^N e_n \bar{B}_n(x, y) \quad (9.212)$$

and substituted into (9.211). Testing functions identical to the basis functions can be employed to construct the $N \times N$ matrix equation $\mathbf{A}\mathbf{e} = \mathbf{b}$, where

$$\begin{aligned} A_{mn} &= \iint_{\Gamma} \left(\frac{1}{\mu_r} \nabla \times \bar{B}_m \cdot \nabla \times \bar{B}_n - k^2 \epsilon_r \bar{B}_m \cdot \bar{B}_n \right) dx dy \\ &+ \int_{\partial\Gamma} \left(\alpha \bar{B}_m \cdot \bar{B}_n - \beta \rho^2 \frac{\partial \bar{B}_m}{\partial t} \cdot \frac{\partial \bar{B}_n}{\partial t} \right) dt \end{aligned} \quad (9.213)$$

and

$$b_m = - \int_{\partial\Gamma} \bar{B}_m \cdot \left(\hat{n} \times \nabla \times \bar{E}^{inc} - \alpha \bar{E}_\phi^{inc} - \beta \frac{\partial^2 \bar{E}_\phi^{inc}}{\partial \phi^2} \right) dt \quad (9.214)$$

Two different types of basis and testing functions will be considered, the CT/LN and the LT/QN functions introduced in Section 9.9.

In common with our previous finite-element implementations, the region of interest is divided into triangular cells, with the mesh terminating on a circular outer boundary. The matrix \mathbf{A} is constructed on a cell-by-cell basis using a connectivity array that identifies the rows and columns of the matrix associated with a particular cell. As suggested in

Section 9.8, we find it convenient to employ a connectivity array that identifies the three edges associated with each cell. A second pointer array is used to identify the two nodes associated with each edge. For the CT/LN functions, 3×3 element matrices are required for the volumetric integrals in (9.213), while 3×3 element matrices also arise from the boundary integrals as explained below. To ensure a common orientation on either side of a given edge, we adopt the convention that the tangential vector basis functions always point from a smaller node index to a larger node index, according to the global numbering.

Equations (9.184)–(9.187) provide element matrix entries for the volumetric integrals in (9.213). The boundary integrals appearing in (9.213) require a tangential differentiation of the field along $\partial\Gamma$. The CT/LN basis functions are discontinuous along $\partial\Gamma$, and consequently the tangential differentiation produces Dirac delta functions between cells. Since basis and testing function discontinuities coincide, the boundary integral involves the product of two delta functions! To alleviate this difficulty, we approximate the problematic Dirac delta functions by piecewise-constant functions straddling two cell edges, as illustrated in Figure 9.20. This approximation is justified since the fictitious discontinuities are introduced by the basis representation, while the true field along $\partial\Gamma$ is continuous. Using this approximation and assuming that the basis functions \bar{B}_m and \bar{B}_n have a common vector orientation along $\partial\Gamma$, element matrix entries providing the boundary integrals over a single cell are obtained as

$$\int_{\text{edge } m} B_m B_n dt = \begin{cases} w_m & m = n \\ 0 & \text{otherwise} \end{cases} \quad (9.215)$$

and

$$\int_{\text{edge } m} \frac{\partial B_m}{\partial t} \frac{\partial B_n}{\partial t} dt \cong \begin{cases} \frac{-2}{w_{m-1} + w_m} & n = m - 1 \\ \frac{2}{w_{m-1} + w_m} + \frac{2}{w_m + w_{m+1}} & n = m \\ \frac{-2}{w_m + w_{m+1}} & n = m + 1 \\ 0 & \text{otherwise} \end{cases} \quad (9.216)$$

where w_m is the width of edge m and the ordered triple $(m - 1, m, m + 1)$ describes three adjacent edges along $\partial\Gamma$ with the index increasing in the ϕ direction.

The treatment of imbedded perfectly conducting material requires the homogeneous Dirichlet condition $\hat{n} \times \bar{E} = 0$, which can be imposed by equating coefficients of tangential basis functions along the conducting boundary to zero. Usually, these coefficients are not included in the global system, and contributions from the element matrices associated with these edges are simply ignored when constructing the global matrix. In any case, a list of edges located on conducting boundaries is a necessary part of the scatterer model.

As a general rule, there are between two and three times as many edges as nodes in a typical triangular-cell model. This result suggests that the system arising from the CT/LN basis functions will always be of larger order than the matrix equation arising from a linear Lagrangian discretization of the scalar Helmholtz equation using the same mesh. (This might be expected, since the transverse fields exhibit more degrees of freedom than E_z or H_z simply because they are vector rather than scalar entities.) The increase in unknowns for a particular model is offset by the fact that the triangular-cell CT/LN functions produce exactly five nonzero entries per row of matrix, except for cells adjacent to conductors, as

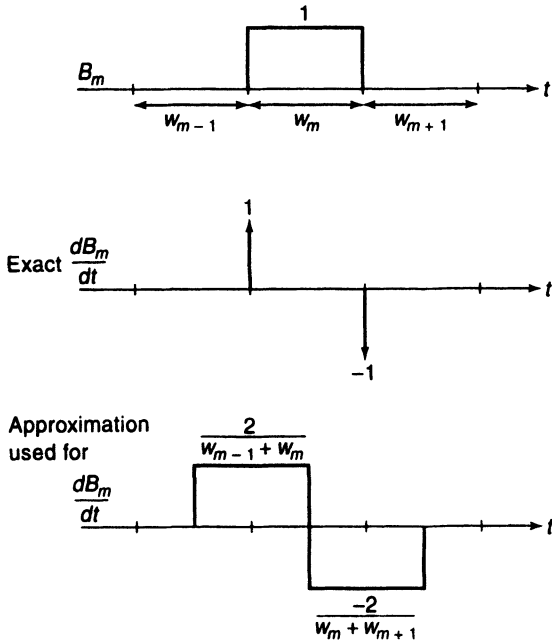


Figure 9.20 Approximation employed to replace the Dirac delta functions with pulse functions.
After [30]. ©1994 IEEE.

compared to some larger (and highly variable) number for node-based expansions. Thus, the matrix arising from the edge-based expansion is generally sparser than that produced by a node-based expansion and is more amenable to packed storage because of its predictable sparsity pattern.

To illustrate the accuracy of the procedure, Figure 9.21 shows the dominant component of the (transverse) electric field induced along a cut through a cylinder having core material of relative permittivity $\epsilon_r = 7-j7$ and radius $0.15\lambda_0$ surrounded by a cladding of $\epsilon_r = 3-j0$ and radius $0.25\lambda_0$, where λ_0 denotes the free-space wavelength. Figure 9.21 is a composite that depicts two numerical results. The left half of the figure shows data obtained using a triangular-cell model with 84 cells in the core region, 112 cells in the cladding, and 320 cells outside the cylinder. The cells are roughly uniform in size, and the longest cell edge in the mesh is $0.075\lambda_0$. The cell densities in the model vary from $112 \text{ cells}/\lambda_d^2$ in the core region to $727 \text{ cells}/\lambda_d^2$ outside the cylinder, where λ_d is the dielectric wavelength and the number of edges (matrix order) is 798. To demonstrate numerical convergence, the right half of the figure shows data obtained with cells that are reduced in linear dimension to approximately one-fourth of that used in the 798-edge model, to produce a mesh with 6956 cells and 10,520 edges. The triangular-cell model is aligned so that the field component shown in Figure 9.21 is entirely tangential to cell edges and is therefore a piecewise-constant function. Plots of the phase of the electric field show similar agreement with exact solutions. From the jump discontinuities present at cell edges, it is apparent that the CT/LN representation is poor at resolving field discontinuities at medium interfaces unless electrically small cells are employed. The RBC used in this approach was imposed at a radius of 0.41λ and for these examples appears to produce a residual error that is much lower than the discretization error associated with the basis function expansion.

We next consider a discretization obtained from the LT/QN basis functions depicted in Figure 9.17. The procedure parallels that of the CT/LN functions and, if naively imple-

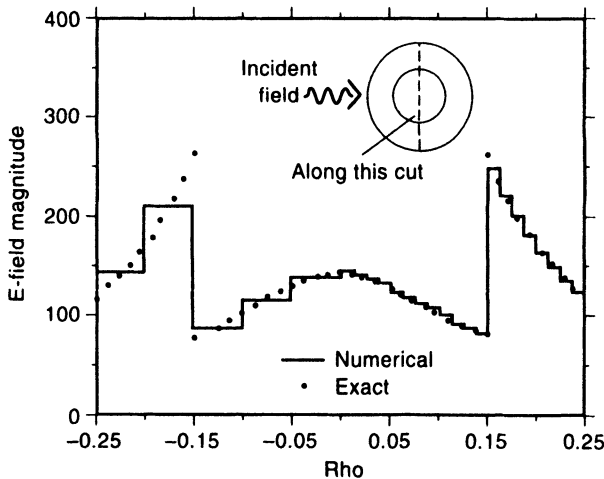


Figure 9.21 Composite result showing the electric field within a layered dielectric cylinder.

The left half of the figure shows data obtained with a 798-edge mesh, while the right half shows data obtained with a 10,520-edge mesh. Both results were obtained using a CT/LN expansion on triangular cells. After [30]. ©1994 IEEE.

mented, produces a matrix with 14, 10, or 8 nonzero entries per row, depending on whether the basis functions are located tangential to an interior edge, tangential to an edge on the radiation boundary, or normal to an edge, respectively. (Fewer entries will be produced in the vicinity of perfectly conducting boundaries.) Both the normal and tangential components of the LT/QN basis functions are discontinuous at cell corners, and the representation along $\partial\Gamma$ is therefore discontinuous from cell to cell. Consequently, an approximation similar to that illustrated in Figure 9.20 is necessary to implement the boundary integral calculations required in Equation (9.213). We leave the development of the element matrix entries as an exercise for the reader (Probs. P9.28 and P9.29).

Some reduction in the total number of LT/QN unknowns is possible, however, since the two interior basis functions per cell only interact with other functions within that cell. These functions can be eliminated from the system of equations at the element matrix level, permitting a reduction in the matrix order without an increase in the number of nonzero entries per row or column. (In traditional finite-element literature, the analogous procedure is named *condensation*.) Consequently, the number of unknowns can be reduced to two per edge throughout the mesh, and the resulting sparse system will have at most 10 nonzero entries per row and column.

Figure 9.22 shows the transverse electric field produced by the LT/QN expansion within a layered dielectric cylinder having core material $\epsilon_r = 7 - j7$ and radius 0.15λ surrounded by a cladding with $\epsilon_r = 3 - j0$ and radius 0.25λ . The RBC is imposed at a radius of 0.45λ . The left half of Figure 9.22 shows data obtained with a 1556-order system based on a 304-cell mesh, with longest cell edge $0.1\lambda_0$, while the right half shows results from an order-4904 system based on a 968-cell mesh with longest edge $0.055\lambda_0$. The field component displayed in Figure 9.22 is entirely tangential to cell edges and is therefore a piecewise-linear function that is not constrained to be continuous from one cell to the next. Despite the freedom in the representation, the discontinuities between cells are very small, except at the dielectric interface where they track the exact solution very closely.

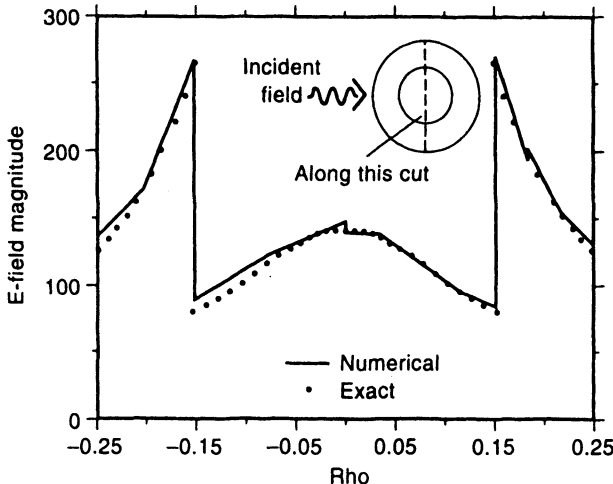


Figure 9.22 Composite result showing the electric field within a layered dielectric cylinder.

The left half of the figure shows data obtained with a 304-cell mesh, while the right half shows data obtained with a 968-cell mesh. Both results were obtained using a LT/QN expansion on triangular cells. After [30]. ©1994 IEEE.

This section has illustrated the implementation of CT/LN and LT/QN basis functions within a two-dimensional scattering formulation. The formulation is straightforward, with one exception. Because a local RBC is incorporated into the formulation, the evaluation of boundary integrals is complicated by cell-to-cell discontinuities in the expansion. A simple approximation (replacing the delta functions by pulse functions) is introduced to circumvent this difficulty. Overall, numerical results for the interior fields exhibit excellent accuracy. Of particular interest is the fact that observed discontinuities in the LT/QN representation are small in homogeneous regions and closely track the desired discontinuous behavior at material interfaces.

9.11 ANALYSIS OF DIELECTRIC-LOADED WAVEGUIDES USING CURL-CONFORMING VECTOR BASIS FUNCTIONS

Consider a waveguide structure aligned with the z -axis and a waveguide mode propagating with z -dependence $e^{i\beta z}$. The task of waveguide analysis is to determine the field distribution and the phase constant β as a function of frequency associated with a waveguide mode of interest. Homogeneously filled waveguiding structures can be formulated in terms of the scalar Helmholtz equation for E_z or H_z and solved by a purely two-dimensional analysis, since the propagation constant β can be found directly from the cutoff wavenumber k_c of a mode according to

$$\beta = \sqrt{k^2 - k_c^2} \quad (9.217)$$

The cutoff wavenumbers are the resonant wavenumbers of the analogous two-dimensional

cavity. For an inhomogeneously filled waveguide, Equation (9.217) no longer applies. Nor does the TM/TE characterization that permits an independent solution for E_z and H_z . Consequently, in the general case we are unable to pose the analysis in terms of a scalar Helmholtz equation.

A number of alternative waveguide formulations are described in the literature, and we focus our attention on one approach based in part on reference [24]. For illustration, we consider an inhomogeneous waveguide bounded by p.e.c. walls and base the analysis on the vector Helmholtz equation

$$\nabla \times \left(\frac{1}{\epsilon_r} \nabla \times \bar{H} \right) = k^2 \mu_r \bar{H} \quad (9.218)$$

where ϵ_r and μ_r are functions of transverse position throughout the waveguide cross section. The magnetic field can be written in the form

$$\bar{H}(x, y, z) = [\bar{H}_t(x, y) + \hat{z} H_z(x, y)] e^{-j\beta z} \quad (9.219)$$

After expanding the curl according to

$$\nabla \times \bar{H} = \nabla_t \times \bar{H}_t - \hat{z} \times (\nabla_t H_z + j\beta \bar{H}_t) \quad (9.220)$$

and

$$\nabla \times \left(\frac{1}{\epsilon_r} \nabla \times \bar{H} \right) = \nabla \times \left(\frac{1}{\epsilon_r} \nabla_t \times \bar{H}_t \right) - \nabla \times \left(\frac{1}{\epsilon_r} \hat{z} \times (\nabla_t H_z + j\beta \bar{H}_t) \right) \quad (9.221)$$

where ∇_t is the transverse part of the ∇ operator, the vector Helmholtz equation can be separated into its transverse components

$$\nabla_t \times \left(\frac{1}{\epsilon_r} \nabla_t \times \bar{H}_t \right) - \frac{1}{\epsilon_r} (j\beta \nabla_t H_z - \beta^2 \bar{H}_t) = k^2 \mu_r \bar{H}_t \quad (9.222)$$

and its z -component

$$-\nabla_t \cdot \left(\frac{1}{\epsilon_r} (\nabla_t H_z + j\beta \bar{H}_t) \right) = k^2 \mu_r H_z \quad (9.223)$$

In order to facilitate the use of either k or β as the eigenvalue, Lee, Sun, and Cendes introduced the scaling [24]

$$\bar{h}_t = \beta \bar{H}_t \quad (9.224)$$

They also proposed the substitution

$$h_z = -j H_z \quad (9.225)$$

which produces a real-valued system of equations in the lossless case. These substitutions convert (9.222) and (9.223) into

$$\nabla_t \times \left(\frac{1}{\epsilon_r} \nabla_t \times \bar{h}_t \right) + \frac{1}{\epsilon_r} (\beta^2 \nabla_t h_z + \beta^2 \bar{h}_t) = k^2 \mu_r \bar{h}_t \quad (9.226)$$

$$-\nabla_t \cdot \left(\frac{1}{\epsilon_r} (\nabla_t h_z + \bar{h}_t) \right) = k^2 \mu_r h_z \quad (9.227)$$

and can be used to construct an eigenvalue formulation for the waveguide problem.

Equation (9.226) is a vector equation with the same leading-order derivatives as the two-dimensional vector Helmholtz equation. This equation can be converted into a weak

form by introducing a transverse vector testing function $\bar{T}(x, y)$ and applying the operations indicated in Equations (9.123)–(9.125) to produce

$$\begin{aligned} & \iint_{\Gamma} \frac{1}{\epsilon_r} (\nabla_t \times \bar{T} \cdot \nabla_t \times \bar{h}_t + \beta^2 \bar{T} \cdot \bar{h}_t + \beta^2 \bar{T} \cdot \nabla_t h_z) \\ &= k^2 \iint_{\Gamma} \mu_r \bar{T} \cdot \bar{h}_t - \int_{\partial\Gamma} \frac{1}{\epsilon_r} \bar{T} \cdot \hat{n} \times \nabla_t \times \bar{h}_t \end{aligned} \quad (9.228)$$

where Γ denotes the guide interior and $\partial\Gamma$ denotes the guide walls. Equation (9.227) is a scalar equation similar in form to the two-dimensional scalar Helmholtz equation, and after introducing a scalar testing function $T(x, y)$, an analogous weak equation can be written in the form

$$\iint_{\Gamma} \frac{1}{\epsilon_r} (\nabla_t T \cdot \nabla_t h_z + \nabla_t T \cdot \bar{h}_t) = k^2 \iint_{\Gamma} \mu_r T h_z + \int_{\partial\Gamma} \frac{1}{\epsilon_r} \left(T \frac{\partial h_z}{\partial n} + T \hat{n} \cdot \bar{h}_t \right) \quad (9.229)$$

Since $\partial\Gamma$ consists of p.e.c. material, appropriate boundary conditions dictate that

$$\hat{n} \times \nabla_t \times \bar{h}_t = 0 \quad (9.230)$$

$$\frac{\partial h_z}{\partial n} = 0 \quad (9.231)$$

and

$$\hat{n} \cdot \bar{h}_t = 0 \quad (9.232)$$

along $\partial\Gamma$. Imposing these conditions eliminates the boundary integrals in (9.228) and (9.229).

Suppose the waveguide interior is divided into triangular cells and the function $\bar{h}_t(x, y)$ is represented by mixed-order vector basis functions of the form introduced in Section 9.9. Similarly, the function h_z can be represented by ordinary scalar Lagrangian basis functions. Given a set of linearly independent vector testing functions and a set of linearly independent scalar testing functions, Equations (9.228) and (9.229) can be written in the form of the matrix eigenvalue equation

$$\begin{bmatrix} \mathbf{A}^{tt} & \mathbf{A}^{tz} \\ \mathbf{A}^{zt} & \mathbf{A}^{zz} \end{bmatrix} \begin{bmatrix} \mathbf{h}_t \\ \mathbf{h}_z \end{bmatrix} = k^2 \begin{bmatrix} \mathbf{B}^{tt} & \mathbf{0} \\ \mathbf{0} & \mathbf{B}^{zz} \end{bmatrix} \begin{bmatrix} \mathbf{h}_t \\ \mathbf{h}_z \end{bmatrix} \quad (9.233)$$

where

$$A_{mn}^{tt} = \iint \frac{1}{\epsilon_r} (\nabla_t \times \bar{T}_m \cdot \nabla_t \times \bar{B}_n + \beta^2 \bar{T}_m \cdot \bar{B}_n) \quad (9.234)$$

$$A_{mn}^{tz} = \beta^2 \iint \frac{1}{\epsilon_r} (\bar{T}_m \cdot \nabla_t B_n) \quad (9.235)$$

$$A_{mn}^{zt} = \beta^2 \iint \frac{1}{\epsilon_r} (\nabla_t T_m \cdot \bar{B}_n) \quad (9.236)$$

$$A_{mn}^{zz} = \beta^2 \iint \frac{1}{\epsilon_r} (\nabla_t T_m \cdot \nabla_t B_n) \quad (9.237)$$

$$B_{mn}^{tt} = \iint \mu_r \bar{T}_m \cdot \bar{B}_n \quad (9.238)$$

$$B_{mn}^{zz} = \beta^2 \iint \mu_r T_m B_n \quad (9.239)$$

and where the integrals encompass the appropriate cells of the mesh. The scalar equation has been scaled by a factor β^2 to improve the symmetry in (9.233). If the vector testing functions are identical to the vector basis functions and the scalar testing functions are identical to scalar basis functions, element matrices for (9.234), (9.237), (9.238), and (9.239) are identical to those discussed in previous sections. The calculation of element matrices for (9.235) and (9.236) is left as an exercise.

To illustrate the approach, Figure 9.23 shows a portion of the k - β diagram for a circular guide concentrically loaded with a circular dielectric rod having $\epsilon_r = 2$. This result was obtained using linear Lagrangian basis functions for h_z and CT/LN basis functions for \bar{h}_t . The mesh contained 124 triangular cells and resulted in a sparse eigenvalue equation of order 273. For this magnetic field formulation, there were 75 nullspace eigenvalues (with value zero) computed, one for each node of the finite-element mesh.

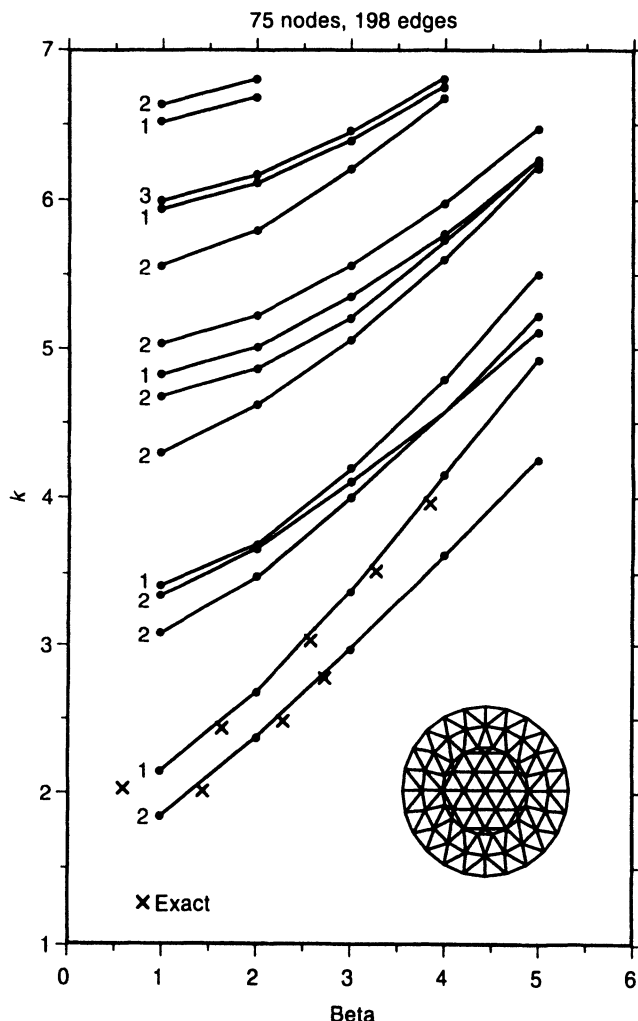


Figure 9.23 The k - β diagram for a concentrically loaded circular waveguide. (The model contained 75 nodes and 198 edges).

In summary, this waveguide formulation incorporates ordinary scalar basis functions to represent the z -component of the field and mixed-order vector basis functions to represent the transverse component, following [24]. The approach offers the possibility of treating material with simultaneous discontinuities in both ϵ_r and μ_r , and it eliminates spurious eigenvalues since the vector basis functions permit jump discontinuities in the normal-field component. Although Equation (9.233) is a generalized matrix eigenvalue equation for k^2 as the eigenvalue, an alternate arrangement of entries in (9.233) can be used to produce an eigenvalue equation for β^2 instead of k^2 (Prob. P9.30). The approach can also be modified to treat the electric field as the primary unknown, in which case the boundary conditions of (9.230)–(9.232) must be replaced by conditions appropriate for the electric field.

9.12 MIXED-ORDER CURL-CONFORMING VECTOR BASIS FUNCTIONS FOR TETRAHEDRAL AND HEXAHEDRAL CELLS [20]

Three-dimensional counterparts of the mixed-order curl-conforming vector basis functions (e.g., CT/LN) can be developed for tetrahedral and hexahedral cells. The general procedure follows the approach employed in Section 9.9. A polynomial-complete linear representation of a vector in three dimensions has the form

$$\hat{x}(A + Bx + Cy + Dz) + \hat{y}(E + Fx + Gy + Hz) + \hat{z}(I + Jx + Ky + Lz) \quad (9.240)$$

containing 12 degrees of freedom. To eliminate degrees of freedom that can only represent the gradient of a quadratic function, we impose the six Nedelec constraints [16]

$$\frac{\partial B_x}{\partial x} = 0 \quad (9.241)$$

$$\frac{\partial B_y}{\partial y} = 0 \quad (9.242)$$

$$\frac{\partial B_z}{\partial z} = 0 \quad (9.243)$$

$$\frac{\partial B_x}{\partial y} + \frac{\partial B_y}{\partial x} = 0 \quad (9.244)$$

$$\frac{\partial B_x}{\partial z} + \frac{\partial B_z}{\partial x} = 0 \quad (9.245)$$

$$\frac{\partial B_y}{\partial z} + \frac{\partial B_z}{\partial y} = 0 \quad (9.246)$$

and reduce the linear representation to the form

$$\bar{B}(x, y, z) = \hat{x}(A + Cy + Dz) + \hat{y}(E - Cx + Hz) + \hat{z}(I - Dx - Hy) \quad (9.247)$$

An identical Cartesian representation is obtained by constraining the tangential component of a linear basis function to be constant along one edge of a tetrahedron and vanish along the other five edges. Six such functions, overlapping a tetrahedral cell, provide a CT/LN representation. To maintain tangential continuity throughout a tetrahedral-cell model, the coefficient for the basis function defined at an edge must be shared by each cell adjacent to that edge. Note that in a general tetrahedral-cell mesh, there may be many cells sharing a

single edge, and thus the sparsity pattern is not as predictable as it was in the two-dimensional examples considered in Sections 9.9 and 9.10.

A convenient representation within a tetrahedron is given in terms of the simplex coordinates (L_1, L_2, L_3, L_4) defined in Section 9.6. The basis function localized along the edge from node i to node j can be written as

$$\bar{B}_{ij} = w_{ij}(L_i \nabla L_j - L_j \nabla L_i) \quad (9.248)$$

where w_{ij} is the length of the edge between nodes i and j . By comparing Equations (9.248) and (9.169), we observe that the CT/LN type of basis function has the same simplex representation in two and three dimensions. As in the two-dimensional case, the three-dimensional functions do not impose continuity of the normal-field component and therefore have the freedom to properly model nullspace eigenfunctions of the curl–curl operator. It is a straightforward matter to show that the three-dimensional CT/LN functions have zero divergence and constant curl within a tetrahedral cell, with a delta function divergence at cell boundaries.

An LT/QN basis can be obtained from a complete quadratic expansion in three dimensions by imposing the 10 conditions [16]

$$\frac{\partial^2 B_i}{\partial i^2} = 0 \quad (i = x, y, z) \quad (9.249)$$

$$\frac{\partial^2 B_i}{\partial j^2} + 2 \frac{\partial^2 B_j}{\partial i \partial j} = 0 \quad (i, j = x, y, z; i \neq j) \quad (9.250)$$

$$\frac{\partial^2 B_x}{\partial y \partial z} + \frac{\partial^2 B_y}{\partial x \partial z} + \frac{\partial^2 B_z}{\partial x \partial y} = 0 \quad (9.251)$$

These serve to eliminate degrees of freedom associated with the gradient of a cubic function and reduce the number of coefficients in a three-dimensional quadratic expansion function from 30 to 20. A quadratic basis set can be defined on tetrahedral cells in three dimensions so that 12 basis functions interpolate to a linear tangential component along each edge of the tetrahedron (again, 2 per edge) while 8 additional functions provide a quadratic normal vector component along each edge and face (two degrees of freedom per face). The edge-based functions straddle all the cells sharing a common edge, while the face-based functions have their domain limited to the two cells that share the appropriate face. One specific form of the LT/QN basis functions in simplex coordinates is presented in Table 9.12.

Vector basis functions with a QT/CuN behavior can be obtained by imposing the 15 constraints embodied in the general expression [16]

$$\frac{\partial^3 B_i}{\partial u_j \partial u_k \partial u_l} + \frac{\partial^3 B_j}{\partial u_i \partial u_k \partial u_l} + \frac{\partial^3 B_k}{\partial u_i \partial u_j \partial u_l} + \frac{\partial^3 B_l}{\partial u_i \partial u_j \partial u_k} = 0 \quad (9.252)$$

where indices i, j, k , and l run from 1 to 3, u_1 denotes x , u_2 denotes y , and u_3 denotes z , and B_1 denotes B_x , and so on. The resulting 45 QT/CuN basis functions are summarized in Table 9.12 and consist of edge-based, face-based, and cell-based functions. In the general case, a three-dimensional expansion of polynomial degree k has

$$N = \frac{1}{2}[k(k+2)(k+3)] \quad (9.253)$$

coefficients within a tetrahedral cell after eliminating the degrees of freedom that can represent the gradient of a $(k+1)$ -order polynomial. Element matrix entries for the CT/LN and LT/QN functions on tetrahedral cells are developed in Chapter 11.

TABLE 9.12 Simplex-Coordinate Definition of Mixed-Order Basis Functions within Tetrahedral Cell

CT/LN (6 Functions, All Edge-Based)	LT/QN (20 Functions)	QT/CuN (45 Functions)
	Edge based	Edge based
$L_1\nabla L_2 - L_2\nabla L_1$	$L_1\nabla L_2$	12 of the form $L_i(2L_i-1)\nabla L_j, i \neq j$
$L_1\nabla L_3 - L_3\nabla L_1$	$L_2\nabla L_1$	6 of the form $L_iL_j(\nabla L_i - \nabla L_j), i \neq j$
$L_1\nabla L_4 - L_4\nabla L_1$	$L_1\nabla L_3$	Face based
$L_2\nabla L_3 - L_3\nabla L_2$	$L_3\nabla L_1$	8 of the form $L_i(2L_i-1)(L_j\nabla L_k - L_k\nabla L_j), i \neq j \neq k$, also omit combinations $ijk = 123, 124, 134, 234$
$L_2\nabla L_4 - L_4\nabla L_2$	$L_1\nabla L_4$	4 of the form $\nabla(L_1L_2L_3)$
$L_3\nabla L_4 - L_4\nabla L_3$	$L_4\nabla L_1$	$\nabla(L_1L_2L_4)$
	$L_2\nabla L_3$	$\nabla(L_1L_3L_4)$
	$L_3\nabla L_2$	$\nabla(L_2L_3L_4)$
	$L_2\nabla L_4$	12 of the form $L_i^2(L_j\nabla L_k - L_k\nabla L_j), i \neq j \neq k$
	$L_4\nabla L_2$	Cell based
	$L_3\nabla L_4$	$L_1L_2L_3\nabla L_4 - L_2L_3L_4\nabla L_1$
	$L_4\nabla L_3$	$L_1L_2L_4\nabla L_3 - L_2L_3L_4\nabla L_1$
	Face based	$L_1L_3L_4\nabla L_2 - L_2L_3L_4\nabla L_1$
$L_1L_2\nabla L_3 - L_1L_3\nabla L_2$		
$L_2L_3\nabla L_1 - L_1L_3\nabla L_2$		
$L_1L_2\nabla L_4 - L_1L_4\nabla L_2$		
$L_2L_4\nabla L_1 - L_1L_4\nabla L_2$		
$L_2L_3\nabla L_4 - L_2L_4\nabla L_3$		
$L_3L_4\nabla L_2 - L_2L_4\nabla L_3$		
$L_1L_3\nabla L_4 - L_1L_4\nabla L_3$		
$L_3L_4\nabla L_1 - L_1L_4\nabla L_3$		

Note: These functions are not normalized.

Mixed-order vector basis functions can also be defined for general hexahedral cell shapes, by transforming standard functions defined on a cube as described in Section 9.14. The standard p th-order functions can be constructed according to

$$\bar{B}_{ijk}^\eta = \hat{\eta}\phi_i^{(p-1)}(\eta)\phi_j^{(p)}(\xi)\phi_k^{(p)}(\nu) \quad i = 1, \dots, p; j = 1, \dots, p+1; k = 1, \dots, p+1 \quad (9.254)$$

$$\bar{B}_{ijk}^\xi = \hat{\xi}\phi_i^{(p)}(\eta)\phi_j^{(p-1)}(\xi)\phi_k^{(p)}(\nu) \quad i = 1, \dots, p+1; j = 1, \dots, p; k = 1, \dots, p+1 \quad (9.255)$$

$$\bar{B}_{ijk}^\nu = \hat{\nu}\phi_i^{(p)}(\eta)\phi_j^{(p)}(\xi)\phi_k^{(p-1)}(\nu), \quad i = 1, \dots, p+1; j = 1, \dots, p+1; k = 1, \dots, p \quad (9.256)$$

where $\phi_j^{(N)}$ is the N th-order Lagrangian polynomial defined in Equation (9.195), and the domain of interest spans $(-1 < \eta < 1, -1 < \xi < 1, -1 < \nu < 1)$.

The lowest order ($p = 1$) basis set consists of 12 functions exhibiting a CT/LN behavior along the edges of the standard cube. Each basis function interpolates to the tangential field at an edge of the global mesh, and the coefficient for that function is shared by all the cells adjacent to that edge to ensure tangential continuity between cells. The $p = 2$ basis set consists of 54 functions that provide a LT/QN representation along the faces of the cube, with 24 functions associated with tangential components along edges, 24 functions associated with tangential components on cell faces, and 6 functions that are confined to a single cell and provide a linearly independent normal-field component at the center of each face.

Vector basis functions of this type were first proposed by Nedelec [16]. A subroutine for calculating the 54×54 element matrix entries for these functions of order $p = 2$ when used to discretize the vector Helmholtz equation for general hexahedral cell shapes was presented by Crowley [25]. Recently, fully interpolatory vector basis functions were developed for tetrahedral and hexahedral cells [23]. These functions are a linear combination of those presented above and satisfy the Nedelec conditions. The interpolatory form is particularly advantageous for functions of order $p \geq 2$.

9.13 DIVERGENCE-CONFORMING VECTOR BASIS FUNCTIONS FOR DISCRETIZATIONS OF THE EFIE

Previous sections introduced curl-conforming vector basis functions. These functions ensure the continuity of the tangential vector component from cell to cell and are well suited for discretizing the vector Helmholtz equation. Because they do not impose normal continuity between cells, curl-conforming functions properly represent eigenfunctions belonging to the nullspace of the curl operator and therefore resolve the spurious mode problem.

In EFIE formulations, the integro-differential operator involves the divergence of the unknown surface current density or volume current density. Consequently, it is necessary to employ expansion functions that ensure a finite divergence across cell boundaries, or equivalently basis functions that maintain normal continuity between cells. To properly represent eigenfunctions from the nullspace of the divergence operator with relatively low-order expansion functions, it appears necessary to allow the current density to have a discontinuous tangential component. Basis functions having finite divergence and possibly discontinuous tangential components are known as *divergence-conforming* functions.

Consider a triangular cell in the x - y plane and an associated vector basis function expressed as a linear polynomial

$$\hat{x}(A + Bx + Cy) + \hat{y}(D + Ex + Fy) \quad (9.257)$$

The six coefficients provide six degrees of freedom in the expansion, and we are free to impose six conditions on the representation in order to generate specific basis functions. Suppose we constrain the normal component of the basis function B to equal unity at both endpoints of one edge of the triangle while simultaneously vanishing along the other two edges. The result of imposing these six constraints on (9.257) is a vector function having constant normal component along one edge and zero normal component along the other two edges. There is also a linear-tangential component along each of the edges, but there are no additional degrees of freedom to constrain the tangential component. Thus, in general, the tangential component will be discontinuous between cells. A simple vector basis can be obtained by superimposing three such functions per triangle and associating the coefficients of each with the normal component at the appropriate edge. When two triangles are adjacent to a common edge, continuity of the normal component can be maintained by assigning the negative coefficient to the basis function in the adjacent triangle. In the global model, the support of this type of vector basis function would be the two triangles associated with each edge (Figure 9.24). The basis provides a CN/LT divergence-conforming representation.

The CN/LT representation can also be obtained by discarding degrees of freedom in (9.257) associated with the curl of a quadratic vector

$$\bar{V} = \hat{z}(Gx^2 + Hxy + Iy^2) \quad (9.258)$$

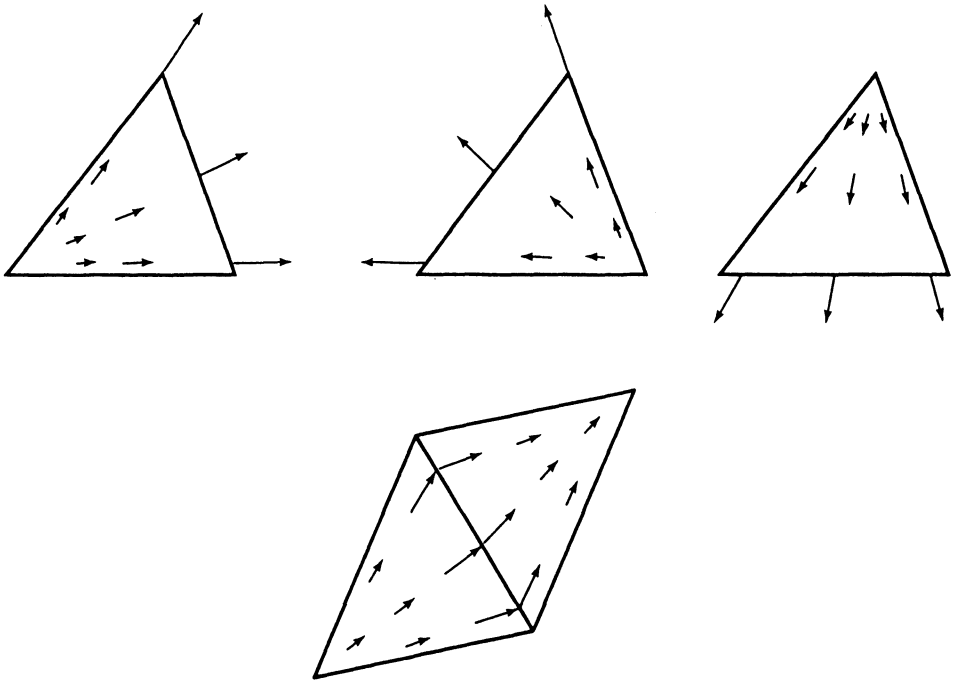


Figure 9.24 Divergence-conforming CN/LT triangular rooftop functions.

The degrees of freedom

$$\nabla \times \bar{V} = \hat{x}(Hx + 2Iy) - \hat{y}(2Gx + Hy) \quad (9.259)$$

have zero divergence and therefore can only represent nullspace eigenfunctions of the divergence operator. They also are not needed to balance terms in an equation involving the field and its divergence. Discarding these degrees of freedom reduces (9.257) to the form

$$\bar{B} = \hat{x}(A + Bx) + \hat{y}(D + By) \quad (9.260)$$

Note that the vector \bar{B} defined in (9.260) is equivalent to $\hat{z} \times \bar{B}_{\text{curl}}$, where \bar{B}_{curl} is the mixed-order curl-conforming basis function defined in (9.165).

Within a cell, a representation of the CN/LT functions is easily obtained using the simplex coordinates defined in Equations (9.1)–(9.7). Each basis function can be written as

$$\bar{B}_i = w_i \hat{z} \times (L_{i+2} \nabla L_{i+1} - L_{i+1} \nabla L_{i+2}) \quad (9.261)$$

where w_i is the length of edge i and edge i is located opposite from node i in the triangle. If the nodes are numbered sequentially in a counterclockwise fashion around the triangle, the basis function \bar{B}_i points away from node i , as depicted in Figure 9.24.

Since

$$\nabla L_i = \frac{1}{2A}(\hat{x} b_i + \hat{y} c_i) \quad (9.262)$$

we obtain the Cartesian representation

$$\begin{aligned}\bar{B}_i = \frac{w_i}{4A^2} & [\hat{x}[a_j c_k - a_k c_j + (b_j c_k - b_k c_j)x] \\ & - \hat{y}[a_j b_k - a_k b_j + (c_j b_k - c_k b_j)y]]\end{aligned}\quad (9.263)$$

demonstrating the equivalence of (9.260) and (9.261). Consequently,

$$\nabla \cdot \bar{B}_i = \frac{w_i}{2A^2} (b_j c_k - b_k c_j) = \pm \frac{w_i}{A} \quad (9.264)$$

and

$$\nabla \times \bar{B}_i = 0 \quad (9.265)$$

The CN/LT basis functions exhibit constant divergence and zero curl within a cell, although the curl assumes a Dirac delta behavior at the cell edges and is therefore not zero globally. As an aid in visualizing these functions, consider a cell having one node located at the origin of a polar coordinate system (ρ, ϕ) . The basis function oriented away from the origin can be written

$$\bar{B}(\rho, \phi) = K\rho\hat{\rho} \quad (9.266)$$

where K is a normalization constant.

The CN/LT basis functions, sometimes known as *triangular rooftop* or *Rao–Wilton–Glisson (RWG)* functions, were proposed by Glisson in 1978 for representing the surface current density within EFIE formulations [32] and subsequently implemented for this purpose [33]. Because they are divergence conforming, these functions permit no charge accumulation at the edge between two cells. The nonphysical charge accumulation was identified as a source of difficulty in EFIE formulations (Section 2.3). Several examples illustrating the CN/LT functions appear in Chapter 10.

Nedelec presented a general family of divergence-conforming functions that include the CN/LT functions as the lowest order member [16]. In the two-dimensional case, the p th-order function can be obtained from the p th-order curl-conforming basis functions presented in Section 9.9, since within a cell

$$\bar{B}_{\text{div-conforming}} = \hat{z} \times \bar{B}_{\text{curl-conforming}} \quad (9.267)$$

As an example, LN/QT functions for triangular cells can be obtained from (9.181)–(9.183) and are depicted in Figure 9.25. The property in (9.267) can also be used to generate divergence-conforming basis functions for rectangular cells. The lowest order members of this family, sometimes known as *rooftop* functions, can be defined with an η -component of the form

$$\bar{B}(\eta, \xi) = \hat{\eta}t(\eta; \eta_3, \eta_4, \eta_5)p(\xi; \xi_1, \xi_2) \quad (9.268)$$

and a ξ -component

$$\bar{B}(\eta, \xi) = \hat{\xi}p(\eta; \eta_1, \eta_2)t(\xi; \xi_3, \xi_4, \xi_5) \quad (9.269)$$

where p and t denote the scalar pulse and subsectional triangle functions discussed in Section 5.3. The coefficients of the rooftop functions represent the vector component normal to an edge, and the expansion provides normal continuity and has a CN/LT behavior along the edges of a cell. These functions are widely used for representing surface currents on

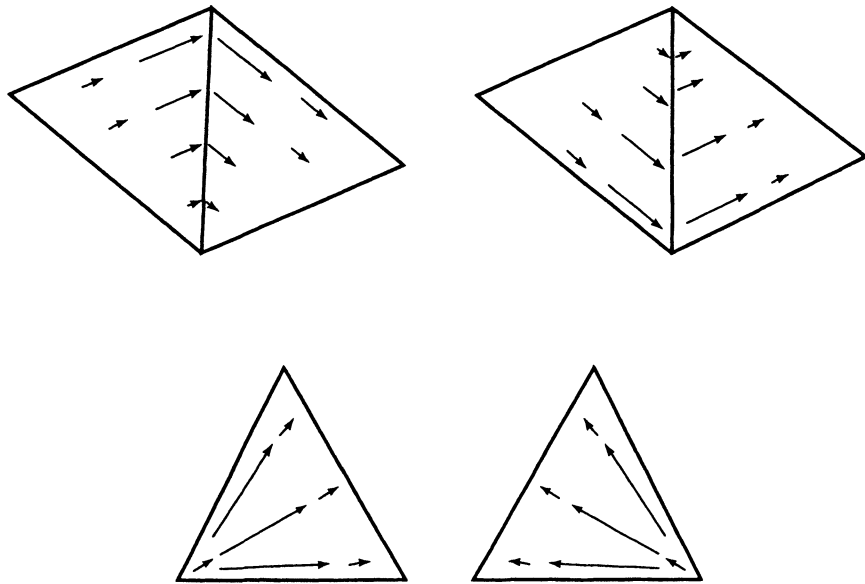


Figure 9.25 Divergence-conforming LN/QT basis functions for triangular cells. The complete set includes two per edge and two per cell.

planar scatterers and microwave devices [34, 35] and will be illustrated in Section 10.1 for expanding the surface current density on flat conducting plates.

Similar vector basis functions can be developed in three dimensions in order to represent a volume current density. Consider a tetrahedral cell and assume that within the tetrahedron the basis function is a linear polynomial

$$\bar{B}(x, y, z) = \hat{x}(A + Bx + Cy + Dz) + \hat{y}(E + Fx + Gy + Hz) + \hat{z}(I + Jx + Ky + Lz) \quad (9.270)$$

Equation (9.270) contains 12 coefficients to be determined by imposing constraints on the function. One possibility is to realize a vanishing normal component along three of the four faces and a constant normal component along the fourth face. (The normal component must be specified at the three corner nodes defining a face of the tetrahedron; thus this procedure uses all 12 degrees of freedom.) The resulting tetrahedral functions provide a CN/LT behavior and exhibit zero curl and constant divergence within a cell. The identical representation can be obtained by discarding the degrees of freedom associated with the curl of a general quadratic-polynomial vector (Prob. P9.34). By assigning one basis function per cell face throughout the mesh and sharing coefficients to ensure normal continuity across cell faces, one obtains a divergence-conforming representation. Vector functions of the divergence-conforming type are well suited for representing volume currents, since they do not permit charge accumulation at the common face between cells. The CN/LT tetrahedral rooftop functions have been used to represent the volumetric polarization current density within a three-dimensional EFIE formulation for dielectric scatterers [36]. Their simplex-coordinate description is investigated in Prob. P9.35.

Families of mixed-order divergence-conforming vector basis functions for tetrahedral and hexahedral cells were originally developed in reference [16]. The CN/LT functions are

the lowest order members of these families. A systematic procedure for generating fully interpolatory basis functions of this type was recently proposed [23].

9.14 MAPPING VECTOR BASIS FUNCTIONS TO CURVILINEAR CELLS IN TWO AND THREE DIMENSIONS

The vector basis functions introduced in preceding sections can be mapped to curved cells in two dimensions or curved surfaces or volumes in three dimensions. In the two-dimensional case, the domain can be mapped according to the scalar procedure described in Sections 9.3 and 9.4, which involves a transformation from (η, ξ) -coordinates to (x, y) -coordinates defined via Lagrangian interpolation polynomials and makes use of the Jacobian relationship in Equation (9.69). For scalar basis functions defined in (η, ξ) -coordinates, a transformation defined by this process uniquely specifies the mapped functions on the curved cells. In addition, the continuity of a scalar basis function is maintained across curved-cell boundaries, although derivative continuity is not.

When transforming vector basis functions, however, there is an additional degree of freedom embodied in the vector direction of the basis function. A local mapping that describes the curved-cell shape via Lagrangian polynomials will generally not be able to maintain the complete continuity of a vector basis function across cell boundaries. In addition, as discussed in Section 9.7, complete continuity may not be desired. Consequently, it is critical to define the vector projection in a way that provides the desired continuity properties. Suppose we have a reference cell described by (η, ξ, ν) -coordinates, and a specific mapping into (x, y, z) -space. In order to define and manipulate vector quantities within a curvilinear cell, we introduce the base vectors

$$\bar{\eta} = \frac{\partial x}{\partial \eta} \hat{x} + \frac{\partial y}{\partial \eta} \hat{y} + \frac{\partial z}{\partial \eta} \hat{z} \quad (9.271)$$

$$\bar{\xi} = \frac{\partial x}{\partial \xi} \hat{x} + \frac{\partial y}{\partial \xi} \hat{y} + \frac{\partial z}{\partial \xi} \hat{z} \quad (9.272)$$

$$\bar{\nu} = \frac{\partial x}{\partial \nu} \hat{x} + \frac{\partial y}{\partial \nu} \hat{y} + \frac{\partial z}{\partial \nu} \hat{z} \quad (9.273)$$

and the reciprocal base vectors

$$\bar{\eta}' = \frac{\partial \eta}{\partial x} \hat{x} + \frac{\partial \eta}{\partial y} \hat{y} + \frac{\partial \eta}{\partial z} \hat{z} = \nabla \eta \quad (9.274)$$

$$\bar{\xi}' = \frac{\partial \xi}{\partial x} \hat{x} + \frac{\partial \xi}{\partial y} \hat{y} + \frac{\partial \xi}{\partial z} \hat{z} = \nabla \xi \quad (9.275)$$

$$\bar{\nu}' = \frac{\partial \nu}{\partial x} \hat{x} + \frac{\partial \nu}{\partial y} \hat{y} + \frac{\partial \nu}{\partial z} \hat{z} = \nabla \nu \quad (9.276)$$

In general, neither the base vectors nor the reciprocal base vectors are mutually orthogonal within a curvilinear cell. However, they always satisfy

$$\bar{\eta} \cdot \bar{\eta}' = 1 \quad \bar{\xi} \cdot \bar{\xi}' = 1 \quad \bar{\nu} \cdot \bar{\nu}' = 1 \quad (9.277)$$

and

$$\bar{\eta} \cdot \bar{\xi}' = 0 \quad \bar{\eta} \cdot \bar{v}' = 0 \quad (9.278)$$

and so on. Furthermore, the base and reciprocal base vectors are related by

$$\bar{\eta}' = \frac{1}{\det \mathbf{J}} \bar{\xi} \times \bar{v} \quad (9.279)$$

$$\bar{\xi}' = \frac{1}{\det \mathbf{J}} \bar{v} \times \bar{\eta} \quad (9.280)$$

$$\bar{v}' = \frac{1}{\det \mathbf{J}} \bar{\eta} \times \bar{\xi} \quad (9.281)$$

$$\bar{\eta} = (\det \mathbf{J}) \bar{\xi}' \times \bar{v}' \quad (9.282)$$

$$\bar{\xi} = (\det \mathbf{J}) \bar{v}' \times \bar{\eta}' \quad (9.283)$$

$$\bar{v} = (\det \mathbf{J}) \bar{\eta}' \times \bar{\xi}' \quad (9.284)$$

where the Jacobian matrix is defined by

$$\begin{bmatrix} \frac{\partial}{\partial \eta} \\ \frac{\partial}{\partial \xi} \\ \frac{\partial}{\partial v} \end{bmatrix} = \begin{bmatrix} \frac{\partial x}{\partial \eta} & \frac{\partial y}{\partial \eta} & \frac{\partial z}{\partial \eta} \\ \frac{\partial x}{\partial \xi} & \frac{\partial y}{\partial \xi} & \frac{\partial z}{\partial \xi} \\ \frac{\partial x}{\partial v} & \frac{\partial y}{\partial v} & \frac{\partial z}{\partial v} \end{bmatrix} \begin{bmatrix} \frac{\partial}{\partial x} \\ \frac{\partial}{\partial y} \\ \frac{\partial}{\partial z} \end{bmatrix} = \mathbf{J} \begin{bmatrix} \frac{\partial}{\partial x} \\ \frac{\partial}{\partial y} \\ \frac{\partial}{\partial z} \end{bmatrix} \quad (9.285)$$

The base vectors and reciprocal base vectors for a two-dimensional cell are depicted in Figure 9.26. As indicated, the base vectors are tangential to the cell boundaries (constant-coordinate surfaces) while the reciprocal base vectors are normal to the cell boundaries.

Returning to the two-dimensional case, consider a vector basis function defined in the reference cell ($-1 < \eta < 1$, $-1 < \xi < 1$), with the transformation defined so that

$$\begin{bmatrix} \frac{\partial}{\partial \eta} \\ \frac{\partial}{\partial \xi} \end{bmatrix} = \begin{bmatrix} \frac{\partial x}{\partial \eta} & \frac{\partial y}{\partial \eta} \\ \frac{\partial x}{\partial \xi} & \frac{\partial y}{\partial \xi} \end{bmatrix} \begin{bmatrix} \frac{\partial}{\partial x} \\ \frac{\partial}{\partial y} \end{bmatrix} = \mathbf{J} \begin{bmatrix} \frac{\partial}{\partial x} \\ \frac{\partial}{\partial y} \end{bmatrix} \quad (9.286)$$

This vector can be represented by its covariant components

$$\bar{B} = (\bar{B} \cdot \bar{\eta}') \bar{\eta}' + (\bar{B} \cdot \bar{\xi}') \bar{\xi}' \quad (9.287a)$$

or its contravariant components

$$\bar{B} = (\bar{B} \cdot \bar{\eta}) \bar{\eta} + (\bar{B} \cdot \bar{\xi}) \bar{\xi} \quad (9.287b)$$

When constructing a curl-conforming basis function on a curvilinear cell, the appropriate mapping is given by

$$\begin{bmatrix} B_x \\ B_y \end{bmatrix} = \mathbf{J}^{-1} \begin{bmatrix} B_\eta \\ B_\xi \end{bmatrix} \quad (9.288)$$

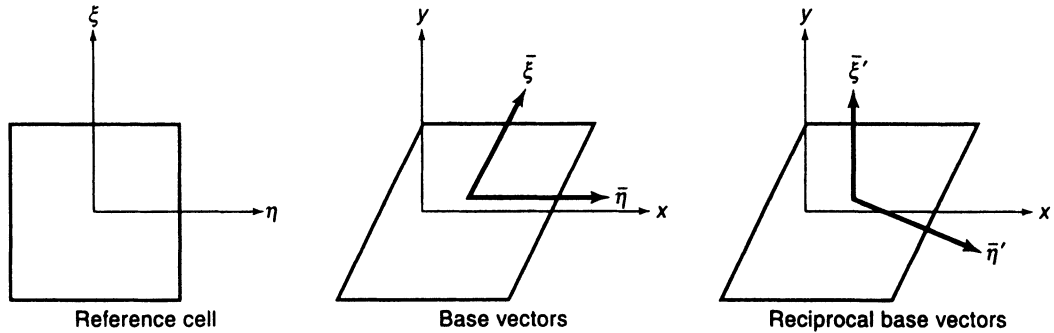


Figure 9.26 Base vectors and reciprocal base vectors for a skewed cell.

where B_η and B_ξ denote the covariant components in the reference cell. The projection defined by (9.288) is a covariant mapping [25] and maintains tangential-vector continuity between cells in the x - y space. When constructing a divergence-conforming basis function, the appropriate mapping is given by

$$\begin{bmatrix} B_x \\ B_y \end{bmatrix} = \frac{1}{\det J} J^T \begin{bmatrix} B_\eta \\ B_\xi \end{bmatrix} \quad (9.289)$$

where B_η and B_ξ denote the contravariant components in the reference cell. The projection defined by (9.289) is a contravariant mapping [25] and maintains normal-vector continuity across cell boundaries in the x - y space.

To demonstrate these ideas, consider an example where we map the square domain $(-1 < \eta < 1, -1 < \xi < 1)$ to the quadrilateral region defined by the points $(x = 0, y = 1)$, $(x = 2, y = 1)$, $(x = -1, y = -1)$, and $(x = 1, y = -1)$. The mapping defined by Equations (9.65) and (9.66) simplifies to

$$x = \eta + \frac{1}{2}\xi + \frac{1}{2} \quad (9.290)$$

$$y = \xi \quad (9.291)$$

and produces a Jacobian matrix

$$J = \begin{bmatrix} 1 & 0 \\ \frac{1}{2} & 1 \end{bmatrix} \quad (9.292)$$

For illustration, consider the vector basis function

$$\bar{B}(\eta, \xi) = \frac{1}{4}(\eta + 1)(\xi + 1)\bar{\eta}' \quad (9.293)$$

defined on $(-1 < \eta < 1, -1 < \xi < 1)$. If mapped according to the covariant projection of (9.288), the Cartesian components of the resulting basis function are

$$B_x = \frac{1}{4}(\eta + 1)(\xi + 1) \quad (9.294)$$

$$B_y = -\frac{1}{8}(\eta + 1)(\xi + 1) \quad (9.295)$$

On the other hand, the same function on the reference cell can be expressed as

$$\bar{B}(\eta, \xi) = \frac{1}{4}(\eta + 1)(\xi + 1)\bar{\eta} \quad (9.296)$$

since the covariant and contravariant components are identical in the reference cell. Equation (9.296) can be mapped according to the contravariant projection of (9.289) to produce

the Cartesian components

$$B_x = \frac{1}{4}(\eta + 1)(\xi + 1) \quad (9.297)$$

$$B_y = 0 \quad (9.298)$$

These two projections are sketched in Figure 9.27.

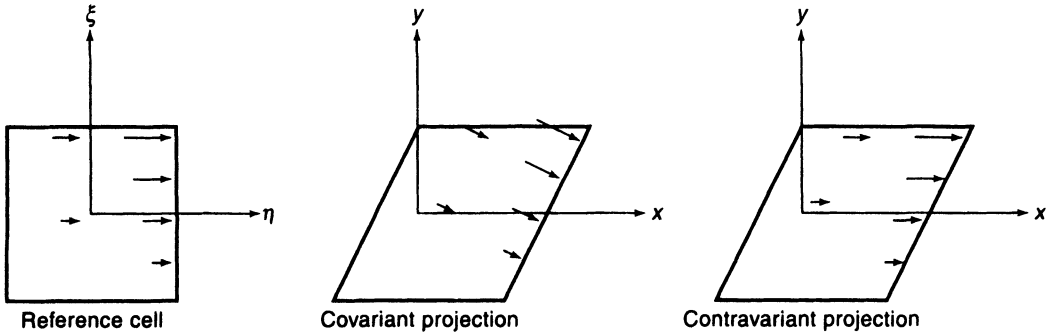


Figure 9.27 Covariant and contravariant projections of a vector function.

Consider the basis function produced by the covariant projection. Along the edge at $y = 1$ in the skewed cell, the tangential component is B_x in (9.294), which is identical to the tangential component of the original basis function along the edge $\xi = 1$. Along the edge of the skewed cell that passes through $(x = 1.5, y = 0)$, the tangential component of the basis function is

$$\left[\frac{\hat{x} + 2\hat{y}}{\sqrt{5}} \cdot \bar{B} \right]_{\eta=1} = 0 \quad (9.299)$$

Along the other two edges, the tangential projection is also zero. Therefore, the covariant mapping does not produce a tangential component except along the cell edge where one exists in the original (η, ξ) domain. (The normal components are not preserved by the mapping, as indicated by the normal component along $y = 1$ that was not present in the reference cell.) Consequently, individual basis functions can be projected onto irregular regions using (9.288) while maintaining the tangential interpolation properties typically associated with curl-conforming functions. By considering two adjacent cells, it can be shown that the continuity of the tangential component across cell boundaries is also maintained (Prob. P9.36).

In a similar manner, the contravariant projection can be shown to preserve normal interpolation properties and normal continuity along cell boundaries. Along the edge at $y = 1$ in the skewed cell, for instance, the normal component is B_y , which is zero according to (9.298). Along the edge of the skewed cell that passes through $(x = 1.5, y = 0)$, the normal component is given by

$$\left[\frac{2\hat{x} - \hat{y}}{\sqrt{5}} \cdot \bar{B} \right]_{\eta=1} = \frac{\xi + 1}{\sqrt{5}} = \frac{y + 1}{\sqrt{5}} \quad (9.300)$$

Along the other two edges, the normal component is zero. Therefore, the contravariant mapping has produced a vector basis function on the quadrilateral cell with no nonzero normal components except where they occurred in the reference cell. Consequently, normal-

component interpolation properties are preserved by (9.289). The continuity properties of the mapping are also maintained, as demonstrated by the example in Prob. P9.37.

When working with mapped basis functions, it is convenient to perform most of the calculations directly in the (η, ξ) system. Consider the element matrix calculations necessary for the vector Helmholtz equation. Since a discretization of the vector Helmholtz equation involves curl-conforming basis functions, the mapping is performed using the covariant projection of (9.288). In the two-dimensional case, the curl operation may be evaluated according to (Prob. P9.38)

$$\hat{z} \cdot \nabla \times \bar{\mathbf{B}} = \left(\frac{\partial B_y}{\partial x} - \frac{\partial B_x}{\partial y} \right) = \frac{1}{(\det \mathbf{J})} \left(\frac{\partial B_{\xi}}{\partial \eta} - \frac{\partial B_{\eta}}{\partial \xi} \right) \quad (9.301)$$

Therefore, element matrix entries for the two-dimensional vector Helmholtz operator can be computed directly in local coordinates via the integrals

$$\begin{aligned} A_{mn}^{(1)} &= \int_x \int_y \nabla \times \bar{\mathbf{B}}_m \cdot \nabla \times \bar{\mathbf{B}}_n dx dy \\ &= \int_{\eta=-1}^1 \int_{\xi=-1}^1 \frac{1}{(\det \mathbf{J})} \left(\frac{\partial B_{m\xi}}{\partial \eta} - \frac{\partial B_{m\eta}}{\partial \xi} \right) \left(\frac{\partial B_{n\xi}}{\partial \eta} - \frac{\partial B_{n\eta}}{\partial \xi} \right) d\eta d\xi \end{aligned} \quad (9.302)$$

$$\begin{aligned} A_{mn}^{(2)} &= \int_x \int_y \bar{\mathbf{B}}_m \cdot \bar{\mathbf{B}}_n dx dy = \int_x \int_y [B_{mx} B_{my}] \begin{bmatrix} B_{nx} \\ B_{ny} \end{bmatrix} dx dy \\ &= \int_{\eta=-1}^1 \int_{\xi=-1}^1 [B_{m\eta} B_{m\xi}] \mathbf{J}^{-T} \mathbf{J}^{-1} \begin{bmatrix} B_{n\eta} \\ B_{n\xi} \end{bmatrix} (\det \mathbf{J}) d\eta d\xi \end{aligned} \quad (9.303)$$

where we have used the relation $dx dy = (\det \mathbf{J}) d\eta d\xi$.

In the three-dimensional case, the curl can be expressed in the form

$$\nabla \times \bar{\mathbf{B}} = \frac{1}{(\det \mathbf{J})} \left[\bar{\eta} \left(\frac{\partial B_v}{\partial \xi} - \frac{\partial B_{\xi}}{\partial v} \right) + \bar{\xi} \left(\frac{\partial B_v}{\partial \nu} - \frac{\partial B_{\nu}}{\partial \eta} \right) + \bar{v} \left(\frac{\partial B_{\xi}}{\partial \eta} - \frac{\partial B_{\eta}}{\partial \xi} \right) \right] \quad (9.304)$$

where the three-dimensional Jacobian matrix is defined in (9.285), the base vectors are defined in (9.271)–(9.273), and B_{η} , B_{ξ} , and B_v denote the covariant components in the reference cell. Note that (9.304) involves the contravariant components of the curl and therefore must be transformed via the mapping

$$\begin{bmatrix} V_x \\ V_y \\ V_z \end{bmatrix} = \mathbf{J}^T \begin{bmatrix} V_{\eta} \\ V_{\xi} \\ V_v \end{bmatrix} \quad (9.305)$$

For notational purposes, let us introduce a column matrix \mathbf{V}_n to represent the contravariant components of the curl of the n th basis function, scaled by the determinant, namely,

$$\mathbf{V}_n^T = \left[\left(\frac{\partial B_{nv}}{\partial \xi} - \frac{\partial B_{n\xi}}{\partial v} \right) \left(\frac{\partial B_{n\eta}}{\partial \nu} - \frac{\partial B_{n\nu}}{\partial \eta} \right) \left(\frac{\partial B_{n\xi}}{\partial \eta} - \frac{\partial B_{n\eta}}{\partial \xi} \right) \right] \quad (9.306)$$

The necessary element matrix entries can be computed from the integrals

$$\begin{aligned} A_{mn}^{(1)} &= \int_x \int_y \int_z \nabla \times \bar{\mathbf{B}}_m \cdot \nabla \times \bar{\mathbf{B}}_n dx dy dz \\ &= \int_{\eta=-1}^1 \int_{\xi=-1}^1 \int_{\nu=-1}^1 \frac{1}{(\det \mathbf{J})} \mathbf{V}_m^T \mathbf{J} \mathbf{J}^T \mathbf{V}_n d\eta d\xi d\nu \end{aligned} \quad (9.307)$$

$$\begin{aligned}
A_{mn}^{(2)} &= \int_x \int_y \int_z \bar{B}_m \cdot \bar{B}_n dx dy dz = \int_x \int_y \int_z [B_{mx} B_{my} B_{mz}] \begin{bmatrix} B_{nx} \\ B_{ny} \\ B_{nz} \end{bmatrix} dx dy dz \\
&= \int_{\eta=-1}^1 \int_{\xi=-1}^1 \int_{\nu=-1}^1 [B_{m\eta} B_{m\xi} B_{m\nu}] \mathbf{J}^{-T} \mathbf{J}^{-1} \begin{bmatrix} B_{n\eta} \\ B_{n\xi} \\ B_{n\nu} \end{bmatrix} (\det \mathbf{J}) d\eta d\xi d\nu
\end{aligned} \tag{9.308}$$

In practice, the entries of the Jacobian matrix \mathbf{J} are obtained directly from the mapping, which typically specifies (x, y, z) as functions of (η, ξ, ν) . The inverse Jacobian and the determinant vary with location within a cell and are usually computed numerically from \mathbf{J} . The required integrations can be performed by numerical quadrature.

For volume EFIE calculations, divergence-conforming basis functions are suggested. It is also convenient to perform the calculations in the reference coordinates. In the two-dimensional case, assuming that the Cartesian components of the basis function are defined by the contravariant mapping in (9.289), the divergence of the basis function is given by (Prob. P9.39)

$$\nabla \cdot \bar{B} = \frac{\partial B_x}{\partial x} + \frac{\partial B_y}{\partial y} = \frac{1}{\det \mathbf{J}} \left(\frac{\partial B_\eta}{\partial \eta} + \frac{\partial B_\xi}{\partial \xi} \right) \tag{9.309}$$

where B_η and B_ξ denote the contravariant components in the reference cell. In the three-dimensional case, the divergence is

$$\nabla \cdot \bar{B} = \frac{1}{\det \mathbf{J}} \left(\frac{\partial B_\eta}{\partial \eta} + \frac{\partial B_\xi}{\partial \xi} + \frac{\partial B_\nu}{\partial \nu} \right) \tag{9.310}$$

We may also develop expressions for the matrix entries associated with a discretization of the EFIE on a curved surface. Since divergence-conforming basis functions have the appropriate properties for representing surface currents, the mapping is performed using a contravariant projection similar to (9.289). However, in this situation the mapping to the curved surface is defined by a transformation of the form

$$x = \sum_n x_n B_n(\eta, \xi) \tag{9.311}$$

$$y = \sum_n y_n B_n(\eta, \xi) \tag{9.312}$$

$$z = \sum_n z_n B_n(\eta, \xi) \tag{9.313}$$

where $\{B_n\}$ represents a set of scalar Lagrangian interpolation functions. Therefore, the Jacobian relationship is given by

$$\begin{bmatrix} \frac{\partial}{\partial \eta} \\ \frac{\partial}{\partial \xi} \end{bmatrix} = \begin{bmatrix} \frac{\partial x}{\partial \eta} & \frac{\partial y}{\partial \eta} & \frac{\partial z}{\partial \eta} \\ \frac{\partial x}{\partial \xi} & \frac{\partial y}{\partial \xi} & \frac{\partial z}{\partial \xi} \end{bmatrix} \begin{bmatrix} \frac{\partial}{\partial x} \\ \frac{\partial}{\partial y} \\ \frac{\partial}{\partial z} \end{bmatrix} = \mathbf{J} \begin{bmatrix} \frac{\partial}{\partial x} \\ \frac{\partial}{\partial y} \\ \frac{\partial}{\partial z} \end{bmatrix} \tag{9.314}$$

The differential surface area on the curved surface can be written in (η, ξ) -coordinates using the scaling

$$dS = Q d\eta d\xi \tag{9.315}$$

where

$$Q = \sqrt{\left(\frac{\partial y}{\partial \eta} \frac{\partial z}{\partial \xi} - \frac{\partial z}{\partial \eta} \frac{\partial y}{\partial \xi}\right)^2 + \left(\frac{\partial z}{\partial \eta} \frac{\partial x}{\partial \xi} - \frac{\partial x}{\partial \eta} \frac{\partial z}{\partial \xi}\right)^2 + \left(\frac{\partial x}{\partial \eta} \frac{\partial y}{\partial \xi} - \frac{\partial y}{\partial \eta} \frac{\partial x}{\partial \xi}\right)^2} \quad (9.316)$$

The basis function must be tangential to the curved patch at every point and ensure normal continuity between adjacent patches. These characteristics can be obtained if the Cartesian components of the basis function are defined by the mapping

$$\begin{bmatrix} B_x \\ B_y \\ B_z \end{bmatrix} = \frac{1}{Q} \mathbf{J}^T \begin{bmatrix} B_\eta \\ B_\xi \end{bmatrix} \quad (9.317)$$

where B_η and B_ξ denote the contravariant components in the reference cell. For a basis function defined by this contravariant mapping, the surface divergence operation happens to simplify to

$$\nabla_s \cdot \bar{\mathbf{B}} = \frac{1}{Q} \left(\frac{\partial B_\eta}{\partial \eta} + \frac{\partial B_\xi}{\partial \xi} \right) \quad (9.318)$$

Therefore, the scalar potential integral from the EFIE is given by

$$\begin{aligned} \Phi &= \frac{1}{j\omega\epsilon} \iint (\nabla_s' \cdot \bar{\mathbf{B}}_n) G dS' \\ &= \frac{1}{j\omega\epsilon} \int_{\eta'=-1}^1 \int_{\xi'=-1}^1 \left(\frac{\partial B_\eta}{\partial \eta'} + \frac{\partial B_\xi}{\partial \xi'} \right) G d\eta' d\xi' \end{aligned} \quad (9.319)$$

where G denotes the Green's function. Since the testing functions are also defined by the transformation in (9.317), a general form for the complete matrix entry is

$$\begin{aligned} \iint \bar{\mathbf{T}}_m \cdot \nabla \Phi dS &= - \iint (\nabla \cdot \bar{\mathbf{T}}_m) \Phi dS \\ &= - \int_{\eta=-1}^1 \int_{\xi=-1}^1 \left(\frac{\partial T_{m\eta}}{\partial \eta} + \frac{\partial T_{m\xi}}{\partial \xi} \right) \Phi d\eta d\xi \end{aligned} \quad (9.320)$$

The matrix entry involving the magnetic vector potential term in the EFIE can be written in terms of the integral

$$\begin{aligned} \iint \bar{\mathbf{T}}_m(\bar{r}) \cdot \left(\iint \bar{\mathbf{B}}_n(\bar{r}') G dS' \right) dS \\ = \int_{\eta=-1}^1 \int_{\xi=-1}^1 \int_{\eta'=-1}^1 \int_{\xi'=-1}^1 [T_{m\eta} T_{m\xi}] \mathbf{J}_m \mathbf{J}_n^T \begin{bmatrix} B_{n\eta} \\ B_{n\xi} \end{bmatrix} G d\eta' d\xi' d\eta d\xi \end{aligned} \quad (9.321)$$

Thus, in these integrals the scale factors arising from the basis functions cancel those arising from the differential surface areas. These expressions provide a convenient way of computing the matrix entries when a piecewise-parametric representation is used to define the curved surface. All calculations can be performed in the (η, ξ) -coordinate system. An example incorporating this procedure will be considered in Chapter 10.

9.15 SUMMARY

This chapter has introduced higher order polynomial basis functions for a variety of applications. In practice, the accuracy of most numerical solutions is limited by the interpolation error associated with the expansion, and the use of higher order functions usually provides better accuracy and faster convergence.

Scalar Lagrangian basis functions for expansions on triangular and quadrilateral cells are widely used for discretizing the scalar Laplacian and scalar Helmholtz operators and have been reviewed. An isoparametric mapping of these functions to cells with curved sides permits the systematic treatment of realistic geometries without an increase in model complexity.

Three-dimensional electromagnetic applications are vector in nature, and this chapter has also introduced a number of vector basis functions for discretizing integral and differential equations. Of particular concern is the appearance of spurious nonzero eigenvalues sometimes obtained in the spectrum of the matrix for the vector Helmholtz operator. Curl-conforming vector basis functions that do not impose normal-vector continuity have been shown to eliminate spurious eigenvalues. Basis functions with this property are presented and incorporated into cavity, scattering, and waveguide formulations to demonstrate their utility. We also introduced divergence-conforming vector basis functions for integral equation formulations. Chapters 10 and 11 will illustrate the application of vector basis functions.

REFERENCES

- [1] O. C. Zienkiewicz and R. L. Taylor, *The Finite Element Method*, London: McGraw-Hill, 1988.
- [2] P. P. Silvester and R. L. Ferrari, *Finite Elements for Electrical Engineers*, Cambridge: Cambridge University Press, 1990.
- [3] G. Strang and G. J. Fix, *An Analysis of the Finite Element Method*, Englewood Cliffs, NJ: Prentice-Hall, 1973.
- [4] L. J. Bahrmasel and R. A. Whitaker, “Convergence of the finite element method as applied to electromagnetic scattering problems in the presence of inhomogeneous media,” *IEEE Trans. Magnetics*, vol. 27, pp. 3845–3847, Sept. 1991.
- [5] J.-C. Sabonnadiere and J.-L. Coulomb, *Finite Element Methods in CAD: Electric and Magnetic Fields*, New York: Springer-Verlag, 1987.
- [6] P. Silvester, “Construction of triangular finite element universal matrices,” *Int. J. Num. Methods Eng.*, vol. 12, pp. 237–244, 1978.
- [7] Z. Zlatev, J. Wasniewski, and K. Schaumburg, *YL2M—Solution of Large and Sparse Systems of Linear Algebraic Equations*, Berlin: Springer-Verlag, 1981.
- [8] D. S. Burnett, *Finite Element Analysis*, Reading, MA: Addison-Wesley, 1987.
- [9] R. D. Graglia, “The use of parametric elements in the moment method solution of static and dynamic volume integral equations,” *IEEE Trans. Antennas Propagat.*, vol. 36, pp. 636–646, May 1988.
- [10] J.-M. Jin, J. L. Volakis, and V. V. Liepa, “A moment method solution of a volume-surface integral equation using isoparametric elements and point matching,” *IEEE Trans. Antennas Propagat.*, vol. 37, pp. 1641–1645, Oct. 1989.

- [11] A. F. Peterson and K. R. Aberegg, "Parametric mapping of vector basis functions for surface integral equation formulations," *Appl. Computat. Electromagnet. Soc. (ACES) J.*, vol. 10., pp. 107–115, Nov. 1995.
- [12] W. E. Boyse, D. R. Lynch, K. D. Paulsen, and G. N. Minerbo, "Nodal based finite element modeling of Maxwell's equations," *IEEE Trans. Antennas Propagat.*, vol. 40, pp. 642–651, June 1992.
- [13] B. T. Smith, J. M. Boyle, J. J. Dongarra, B. S. Garbow, Y. Ikebe, V. C. Klema, and C. B. Moler, *Matrix Eigensystem Routines—EISPACK Guide*, New York: Springer-Verlag, 1976.
- [14] Z. J. Cendes, "Vector finite elements for electromagnetic field computation," *IEEE Trans. Magnetics*, vol. 27, pp. 3958–3966, Sept. 1991.
- [15] D. Sun, J. Manges, X. Yuan, and Z. Cendes, "Spurious modes in finite element methods," *IEEE Antennas Propagat. Mag.*, vol. 37, no. 5, pp. 12–24, Oct. 1995.
- [16] J. C. Nedelec, "Mixed finite elements in R3," *Num. Math.*, vol. 35, pp. 315–341, 1980.
- [17] J. C. Nedelec, "A new family of mixed finite elements in R3," *Num. Math.*, vol. 50, pp. 57–81, 1986.
- [18] G. Mur and A. T. de Hoop, "A finite element method for computing three-dimensional electromagnetic fields in inhomogeneous media," *IEEE Trans. Magnetics*, vol. MAG-21, pp. 2188–2191, Nov. 1985.
- [19] G. Mur, "Edge elements, their advantages and their disadvantages," *IEEE Trans. Magnetics*, vol. 30, pp. 3552–3557, Sept. 1994.
- [20] A. F. Peterson and D. R. Wilton, "Curl-conforming mixed-order edge elements for discretizing the 2D and 3D vector Helmholtz equation," in *Finite Element Software for Microwave Engineering*, eds. T. Itoh, G. Pelosi, and P. P. Silvester, New York: Wiley, 1996.
- [21] A. Bossavit and J. C. Verite, "A mixed FEM-BIEM method to solve 3D eddy current problems," *IEEE Trans. Magnetics*, vol. MAG-18, pp. 431–435, Mar. 1982.
- [22] M. L. Barton and Z. J. Cendes, "New vector finite elements for three-dimensional magnetic field computation," *J. Appl. Phys.*, vol. 61, pp. 3919–3921, Apr. 1987.
- [23] R. D. Graglia, D. R. Wilton, and A. F. Peterson, "Higher order interpolatory vector bases for computational electromagnetics," *IEEE Trans. Antennas Propagat.*, vol. 45, pp. 329–342, Mar. 1997.
- [24] J.-F. Lee, D.-K. Sun, and Z. J. Cendes, "Full-wave analysis of dielectric waveguides using tangential vector finite elements," *IEEE Trans. Microwave Theory Tech.*, vol. 39, pp. 1262–1271, Aug. 1991.
- [25] C. W. Crowley, "Mixed-order covariant projection finite elements for vector fields," Ph.D. dissertation, McGill University, Montreal, Quebec, Feb. 1988.
- [26] G. S. Warren and W. R. Scott, "An investigation of numerical dispersion in the vector finite element method," *IEEE Trans. Antennas Propagat.*, vol. 42, pp. 1502–1508, Nov. 1994.
- [27] G. S. Warren, "The analysis of numerical dispersion in the finite element method using nodal and vector elements," Ph.D. dissertation, Georgia Institute of Technology, Atlanta, GA, 1995.
- [28] J. B. Manges and Z. J. Cendes, "A generalized tree-cotree gauge for magnetic field computations," *IEEE Trans. Magnetics*, vol. 31, pp. 1342–1347, May 1995.

- [29] D. R. Wilton, "Topological considerations in surface patch and volume cell modeling of electromagnetic scatterers," *Proceedings of the URSI Symposium on Electromagnetic Theory*, Santiago de Compostela (Spain), International Union of Radio Scientists (URSI), pp. 65–68, August 23–26, 1983.
- [30] A. F. Peterson, "Vector finite element formulation for scattering from two-dimensional heterogeneous bodies," *IEEE Trans. Antennas Propagat.*, vol. 43, pp. 357–365, Mar. 1994.
- [31] J. Parker, R. D. Ferraro, and P. C. Liewer, "A comparison of isoparametric edge elements and DnEt elements for 3D electromagnetic scattering problems," *Abstracts of the URSI Radio Science Meeting*, Dallas, TX, International Union of Radio Scientists (USRI), p. 377, May 1990.
- [32] A. W. Glisson, "On the development of numerical techniques for treating arbitrarily shaped surfaces," Ph.D. dissertation, University of Mississippi, 1978.
- [33] S. M. Rao, D. R. Wilton, and A. W. Glisson, "Electromagnetic scattering by surfaces of arbitrary shape," *IEEE Trans. Antennas Propagat.*, vol. AP-30, pp. 409–418, May 1982.
- [34] A. W. Glisson and D. R. Wilton, "Simple and efficient numerical methods for problems of electromagnetic radiation and scattering from surfaces," *IEEE Trans. Antennas Propagat.*, vol. AP-28, pp. 593–603, Sept. 1980.
- [35] J. C. Rautio and R. F. Harrington, "An electromagnetic time-harmonic analysis of shielded microstrip circuits," *IEEE Trans. Microwave Theory Tech.*, vol. MTT-35, pp. 726–730, Aug. 1987.
- [36] D. H. Schaubert, D. R. Wilton, and A. W. Glisson, "A tetrahedral modeling method for electromagnetic scattering by arbitrarily shaped inhomogeneous dielectric bodies," *IEEE Trans. Antennas Propagat.*, vol. AP-32, pp. 77–85, Jan. 1984.

PROBLEMS

- P9.1** Using the procedure described in Equations (9.9)–(9.14), find an expression for the 10 cubic-order Lagrangian basis functions defined within triangular cells. Provide a sketch of these functions similar to Figure 9.4.
- P9.2** Using Maxwell's equations, obtain an equation that describes the proper derivative discontinuity in E_z and H_z at an interface between two two-dimensional regions with material parameters ϵ_1, μ_1 and ϵ_2, μ_2 .
- P9.3** Verify the formulas in (9.34) and (9.35).
- P9.4** (a) Find general expressions for the element matrix entries associated with (9.27) and (9.30) for one-dimensional Lagrangian basis and testing functions of any polynomial order. In other words, outline a procedure similar to the development in Equations (9.31)–(9.41), but for the one-dimensional case.
 (b) Find the explicit entries of the element matrices in part (a) for quadratic-order functions.
- P9.5** Sketch the nine biquadratic Lagrangian functions in (9.56)–(9.64).
- P9.6** Estimate the number of nodes and the number of nonzero entries as a function of the number of cells for the bilinear and biquadratic Lagrangian interpolation functions defined in Equations (9.47)–(9.50) and (9.56)–(9.64). Assume an idealized (infinite) mesh of rectangular cells.

P9.7 By evaluating the integrals in (9.54) and (9.55), obtain the 4×4 element matrix entries for the bilinear Lagrangian functions defined on a rectangular cell ($x_1 < x < x_2$, $y_1 < y < y_2$).

P9.8 Consider the transformation from the standard cell ($-1 < \eta < 1$, $-1 < \xi < 1$) to a quadrilateral region as described by (9.65)–(9.75). Write a computer program to calculate the element matrix entries defined in (9.72) and (9.75) for the bilinear Lagrangian functions in (9.47)–(9.50). Use this program to determine the element matrix entries for a region with corners at $(0, 0)$, $(1, 0)$, $(2, 1)$, and $(1, 1)$.

P9.9 Develop a computer subroutine to evaluate the integrals in (9.86) and (9.87) for quadratic Lagrangian basis functions defined on a curved triangular cell, assuming that the cell shape is defined by an isoparametric mapping using the same quadratic functions.

P9.10 Consider the mapping defined by

$$x = \sum_{i=1}^3 x_i B_i(t)$$

where $\{B_i(t)\}$ denote the one-dimensional quadratic Lagrangian basis functions defined over the interval $-1 < t < 1$ in Equations (9.92)–(9.94) and x_2 is located a variable distance between x_1 and x_3 in the interval $x_1 < x_2 < x_3$. Show that values of x_2 outside the range

$$x_1 + \frac{1}{4}\Delta < x_2 < x_3 - \frac{1}{4}\Delta$$

where $\Delta = x_3 - x_1$ produce an unacceptable representation of the interval. Discuss the impact of this result on the placement of nodes in a one-dimensional isoparametric representation, such as that considered in Section 9.5. Can you suggest a procedure for obtaining similar guidelines with multidimensional mappings?

P9.11 Based on the two-dimensional development of the bilinear and biquadratic Lagrangian functions on a standard cell, find expressions for the 8 linear and 27 quadratic Lagrangian basis functions defined on a three-dimensional cell ($-1 < \eta < 1$, $-1 < \xi < 1$, $-1 < \nu < 1$).

P9.12 Expand Equation (9.108) to obtain an explicit expression with the form

$$L_i = \frac{1}{6V}(a_i + b_i x + c_i y + d_i z)$$

for the simplex coordinates (L_1, L_2, L_3, L_4) as a function of the four corners (x_i, y_i, z_i) and volume V of a tetrahedron.

P9.13 Show that mathematical functions of the form

$$\bar{V}_{mn} = \nabla \left[\sin\left(\frac{m\pi x}{a}\right) \sin\left(\frac{n\pi y}{b}\right) \right]$$

satisfy the boundary condition $\hat{n} \times \bar{V}_{mn} = 0$ along the four walls of a two-dimensional cavity ($0 < x < a$, $0 < y < b$). Therefore, they constitute nullspace eigenfunctions of the two-dimensional vector Helmholtz equation $\nabla \times \nabla \times \bar{E} = k^2 \bar{E}$ for a homogeneous cavity with electric walls. Compare the nullspace eigenfunctions with the usual TE cavity modes. How do they differ? Calculate the divergence of both eigenfunction families.

P9.14 Consider Equation (9.152) as though the function was defined within the four square cells surrounding the origin (Figure 9.14). A bilinear Lagrangian basis set defined in these four cells consists of nine functions interpolating to the x -components and nine basis functions interpolating to the y -components at cell corners. Construct the projection of (9.152) onto the bilinear expansion by equating the x - and y -components at the nine nodes. To obtain a continuous representation at the origin, where (9.152)

is discontinuous, use the average value (zero). Sketch the resulting function. Compare the curl of (9.152) and the curl of the Lagrangian approximation.

- P9.15** Using the property $\nabla \cdot \bar{E} = 0$, the vector Helmholtz equation $\nabla \times \nabla \times \bar{E} = k^2 \bar{E}$ for a homogeneous region can be cast into the form $\nabla^2 \bar{E} + k^2 \bar{E} = 0$. Consider the two-dimensional cavity described in Prob. P9.13. Are the functions \bar{V}_{mn} defined in Prob. P9.13 solutions of $\nabla^2 \bar{E} + k^2 \bar{E} = 0$? If so, find their eigenvalues. Discuss the implication of your results.
- P9.16** By considering the geometry in Figure 9.28, show that the basis function $w_3 L_2 \nabla L_1$ from the set defined in (9.154) has a linear tangential projection along edge 12 with value zero at node 1 and one at node 2.

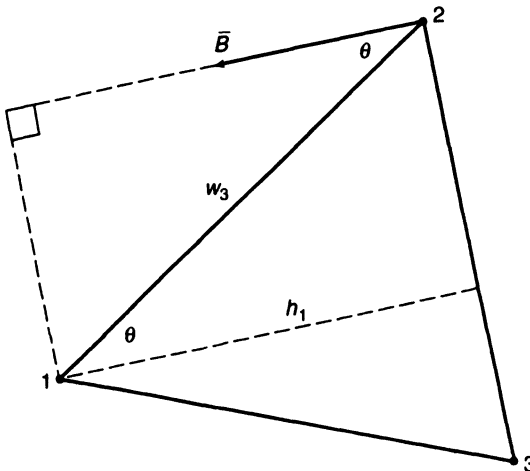


Figure 9.28 Geometry to be used for Prob. P9.16.

- P9.17** (a) Sketch the 12 vector basis functions defined in Equations (9.156)–(9.158), to produce a figure similar to Figure 9.15.
 (b) Show that the normalization used in (9.156) and (9.157) produces unit tangential values at the appropriate interpolation points.

- P9.18** By integrating the linear vector basis functions defined in (9.154) in simplex coordinates, obtain the entries of the 6×6 element matrices for (9.162) and (9.163) evaluated over a single triangular cell. For instance, if

$$\bar{B}_{ij} = w_{ij} L_i \nabla L_j$$

use Equations (9.4)–(9.7) to show that

$$\iint \nabla \times \bar{B}_{ij} \cdot \nabla \times \bar{B}_{mn} dx dy = \frac{w_{ij} w_{mn}}{16A^3} (b_i c_j - c_i b_j)(b_m c_n - c_m b_n)$$

and

$$\iint \bar{B}_{ij} \cdot \bar{B}_{mn} dx dy = \frac{w_{ij} w_{mn}}{2A} (b_j b_n + c_j c_n) \begin{cases} \frac{1}{12} & i = m \\ \frac{1}{24} & \text{otherwise} \end{cases}$$

where w_{ij} is the length of the edge between nodes i and j and A is the area of the cell.

- P9.19** Consider the CT/LN basis function $\bar{B} = w_3 (L_2 \nabla L_1 - L_1 \nabla L_2)$ and the triangular cell depicted in Figure 9.28. Show that the tangential component of \bar{B} has unit value along edge 12 and vanishes along the other two edges of the cell. How does the normal component behave along edge 12?

- P9.20** Show that the basis functions in (9.182) and (9.183) satisfy Equations (9.177)–(9.180).
- P9.21** A vector representation equivalent to the LT/QN functions defined in (9.181)–(9.183) can be constructed numerically for a given triangular cell in such a manner that all 8 functions are interpolatory at specific locations along the cell edges. Beginning with the complete quadratic polynomial in Equation (9.155), identify 12 conditions that must be imposed to construct each interpolatory basis function in the form of (9.175).
- P9.22** The first nine QT/CuN basis functions in Table 9.9 interpolate to the tangential component at the endpoint and middle of each edge of the triangular cell. Develop a normalization of these functions that results in each having a unity-tangential component at the interpolation point.
- P9.23** Construct an alternate set of LT/QN basis functions for a standard rectangular cell with the property that the eight functions that interpolate to the tangential values along the edges are entirely linear (like the LT/QN functions developed for triangular cells in Section 9.9).
- P9.24** Chapter 3 summarized the development of the Bayliss–Turkel type of local RBC. By applying a similar procedure to (9.203), obtain the first- and second-order conditions presented in (9.204) and (9.205). In addition, show that (9.205) can be rewritten as (9.206).
- P9.25** Using an eigenfunction expansion of the exterior fields and a development that parallels that given in Section 3.3, show that an exact RBC can be expressed in the form

$$(\hat{\rho} \times \nabla \times \bar{E}^s)(a, \phi) = \hat{\phi} \frac{1}{2\pi} \int_0^{2\pi} E_\phi^s(a, \phi') K(\phi - \phi') d\phi'$$

where

$$K(\phi - \phi') = k \sum_{n=-\infty}^{\infty} \frac{H_n^{(2)}(ka)}{H_n^{(2)\prime}(ka)} e^{jn(\phi - \phi')}$$

and a is the radius of the circular radiation boundary. Discuss the implementation of this RBC in connection with the TE scattering procedure of Section 9.10.

- P9.26** By modifying the development in Section 3.10, obtain an integral equation RBC that can be used with the two-dimensional scattering formulation in Section 9.10 in order to treat arbitrary boundary shapes.
- P9.27** (a) Consider an idealized infinite mesh of equilateral triangles arranged in a hexagonal pattern. Determine the number of unknowns per cell associated with the CT/LN and LT/QN representations introduced in Section 9.9. How do these numbers compare with the estimates obtained in Section 9.2 for the linear and quadratic Lagrangian representations for a scalar quantity?
- (b) Repeat part (a) to determine the number of nonzero matrix entries per cell for the CT/LN and LT/QN basis functions. How do these estimates compare with those for the scalar basis functions shown in Figure 9.6?
- (c) Combine the estimates of parts (a) and (b) to obtain an estimate of the number of nonzero matrix entries as a function of the number of unknowns for the CT/LN and LT/QN functions. Obtain a similar estimate for the linear and quadratic scalar Lagrangian functions on a triangular-cell mesh.
- (d) The two interior LT/QN functions only interact with functions within their cell and in a deterministic problem can be eliminated from the global system of equations prior to matrix construction. Repeat the estimates in parts (a)–(c) without including the interior LT/QN functions.
- P9.28** Obtain the entries of the 8×8 element matrices for Equations (9.162)–(9.163) and the LT/QN basis functions defined on triangular cells. (*Hint:* Part of the result is given in Prob. P9.18.)

- P9.29** The scattering formulation discussed in Section 9.10 requires the calculation of boundary integrals

$$\int_{\partial\Gamma} \bar{B}_m \cdot \bar{B}_n dt$$

and

$$\int_{\partial\Gamma} \frac{\partial \bar{B}_m}{\partial t} \cdot \frac{\partial \bar{B}_n}{\partial t} dt$$

Show that the first integral can be evaluated for LT/QN functions to produce

$$\begin{aligned} \int_{\text{edge } m} \bar{B}_m^+ \cdot \bar{B}_m^+ dt &= \int_{\text{edge } m} \bar{B}_m^- \cdot \bar{B}_m^- dt = \frac{1}{3} w_m \\ \int_{\text{edge } m} \bar{B}_m^+ \cdot \bar{B}_m^- dt &= \frac{1}{6} w_m \end{aligned}$$

where w_m denotes the length of edge m , \bar{B}_m^+ denotes a basis function whose tangential value increases in magnitude in the positive ϕ direction along edge m , and \bar{B}_m^- denotes a basis function whose tangential value decreases in magnitude in the positive ϕ direction. In addition, by employing an approximation similar to that described in Figure 9.20, show that the nonzero contributions from the second integral are

$$\int_{\text{edge } m} \frac{\partial \bar{B}_m^+}{\partial t} \cdot \frac{\partial \bar{B}_n^+}{\partial t} dt = \int_{\text{edge } m} \frac{\partial \bar{B}_m^-}{\partial t} \cdot \frac{\partial \bar{B}_n^-}{\partial t} dt \cong \begin{cases} \frac{-1}{w_{m-1} + w_m} & n = m - 1 \\ \frac{1}{w_m} & n = m \\ \frac{-1}{w_m + w_{m+1}} & n = m + 1 \end{cases}$$

and

$$\int_{\text{edge } m} \frac{\partial \bar{B}_m^+}{\partial t} \cdot \frac{\partial \bar{B}_n^-}{\partial t} dt \cong \frac{1}{w_m + w_{m-1}} - \frac{1}{w_m} + \frac{1}{w_m + w_{m+1}}$$

where w_{m-1} , w_m , and w_{m+1} denote the length of three adjacent edges ordered so that the index increases in the ϕ direction.

- P9.30** By rearranging terms in Equation (9.233), construct a matrix eigenvalue equation with β^2 as the eigenvalue.
- P9.31** Develop a formulation similar to that given in Section 9.11 for dielectric-loaded waveguides that uses the electric field as the primary unknown. Identify appropriate boundary conditions for p.e.c. walls and discuss the impact of these on the boundary integrals appearing in the E -field versions of (9.228) and (9.229).
- P9.32** Develop expressions for the 6×6 element matrices associated with the CT/LN basis functions and the integrals

$$\begin{aligned} \iiint \nabla \times \bar{B}_m \cdot \nabla \times \bar{B}_n \\ \iiint \bar{B}_m \cdot \bar{B}_n \end{aligned}$$

defined over a tetrahedral cell.

- P9.33** Consider an idealized cubical cell mesh in three dimensions and the LT/QN basis functions described in Section 9.12. Estimate the number of unknowns per cell, the number

of nonzero entries per cell, and the number of nonzero entries per unknown for this representation under the assumptions that (a) the entire set of 54 basis functions per cell is retained in the global system and (b) the 6 basis functions that are entirely local in each cell are eliminated prior to constructing the global system, leaving 48 basis functions per cell.

- P9.34** (a) Show that a three-dimensional vector \bar{Q} whose components are polynomials of exactly quadratic order has curl with the general form

$$\nabla \times \bar{Q} = \hat{x}(Ax + By + Cz) + \hat{y}(Dx + Ey + Fz) + \hat{z}[Gx + Hy - (A + E)z]$$

and therefore embodies exactly eight degrees of freedom.

- (b) By eliminating these eight degrees of freedom from the complete linear vector in Equation (9.270), obtain the Cartesian representation

$$\bar{B}_{\text{div}} = \hat{x}(\alpha + \delta x) + \hat{y}(\beta + \delta y) + \hat{z}(\gamma + \delta z)$$

(c) Confirm that \bar{B}_{div} provides a CN/LT behavior within a tetrahedral cell.

- P9.35** Consider the function

$$L_i \nabla L_j \times \nabla L_k + L_j \nabla L_k \times \nabla L_i + L_k \nabla L_i \times \nabla L_j \quad i \neq j \neq k$$

defined within a tetrahedral domain, in terms of simplex coordinates (L_1, L_2, L_3, L_4). Does this function satisfy the conditions for the CN/LT expansion described in Section 9.13?

- P9.36** Verify that the mapping in (9.288) maintains tangential continuity between cells for the specific cell pair given by

Cell A: corners at $(-1, -1), (1, -1), (2, 1), (0, 1)$

Cell B: corners at $(1, -1), (3, -2), (3, 1), (2, 1)$

Determine the Jacobian matrix for each cell, and consider the basis function

$$\bar{B}_A(\eta, \xi) = \frac{(1 + \eta)(1 + \xi)}{4} \bar{\xi},$$

in cell A and

$$\bar{B}_B(\eta, \xi) = \frac{(1 - \eta)(1 + \xi)}{4} \bar{\xi},$$

in cell B. Show that the mapped functions $\bar{B}_A(x, y)$ and $\bar{B}_B(x, y)$ have the same tangential component along the common edge.

- P9.37** Verify that the mapping in (9.289) maintains normal continuity between cells for the specific cell pair given in Prob P9.36 and the basis functions

$$\bar{B}_A(\eta, \xi) = \frac{(1 + \eta)(1 + \xi)}{4} \bar{\eta}$$

in cell A and

$$\bar{B}_B(\eta, \xi) = \frac{(1 - \eta)(1 + \xi)}{4} \bar{\eta}$$

in cell B. Show that the mapped functions $\bar{B}_A(x, y)$ and $\bar{B}_B(x, y)$ have the same normal component along the common edge.

- P9.38** Verify (9.301) by direct calculation. *Hint:*

$$\bar{B} = \left(\frac{\partial \eta}{\partial x} B_\eta + \frac{\partial \xi}{\partial x} B_\xi \right) \hat{x} + \left(\frac{\partial \eta}{\partial y} B_\eta + \frac{\partial \xi}{\partial y} B_\xi \right) \hat{y}$$

$$\frac{\partial}{\partial x} = \frac{\partial \eta}{\partial x} \frac{\partial}{\partial \eta} + \frac{\partial \xi}{\partial x} \frac{\partial}{\partial \xi}$$

$$\frac{\partial}{\partial y} = \frac{\partial \eta}{\partial y} \frac{\partial}{\partial \eta} + \frac{\partial \xi}{\partial y} \frac{\partial}{\partial \xi}$$

Use $\mathbf{J}\mathbf{J}^{-1} = \mathbf{I}$ to obtain relations such as

$$\frac{\partial \eta}{\partial x} \frac{\partial x}{\partial \eta} + \frac{\partial \eta}{\partial y} \frac{\partial y}{\partial \eta} = 1$$

in order to simplify the expression.

P9.39 Verify (9.309) by direct calculation using

$$\bar{B} = \frac{1}{\det \mathbf{J}} \left(\frac{\partial x}{\partial \eta} B_\eta + \frac{\partial x}{\partial \xi} B_\xi \right) \hat{x} + \frac{1}{\det \mathbf{J}} \left(\frac{\partial y}{\partial \eta} B_\eta + \frac{\partial y}{\partial \xi} B_\xi \right) \hat{y}$$

and ideas similar to those suggested in Prob. P9.38.